

Moiré Deflectometry with a Low-Energy Ion Beam for the AEGIS Experiment

Pierre Lansonneur

► **To cite this version:**

Pierre Lansonneur. Moiré Deflectometry with a Low-Energy Ion Beam for the AEGIS Experiment. Nuclear Experiment [nucl-ex]. Université de Lyon, 2017. English. <NNT : 2017LYSE1191>. <tel-01674237>

HAL Id: tel-01674237

<https://tel.archives-ouvertes.fr/tel-01674237>

Submitted on 2 Jan 2018

HAL is a multi-disciplinary open access archive for the deposit and dissemination of scientific research documents, whether they are published or not. The documents may come from teaching and research institutions in France or abroad, or from public or private research centers.

L'archive ouverte pluridisciplinaire **HAL**, est destinée au dépôt et à la diffusion de documents scientifiques de niveau recherche, publiés ou non, émanant des établissements d'enseignement et de recherche français ou étrangers, des laboratoires publics ou privés.



N° d'ordre NNT : 2017LYSE1191

THÈSE DE DOCTORAT DE L'UNIVERSITÉ DE LYON
opérée au sein de
l'Université Claude Bernard Lyon 1

École Doctorale ED52
Physique et Astrophysique (PHAST)

Spécialité de doctorat : Physique

Soutenue publiquement le 05/10/2017, par :
Pierre Lansonneur

Défectométrie Moiré d'Ions de Basse Énergie pour l'Expérience AEGIS

**Moiré Deflectometry with a Low-Energy
Ion Beam for the AEGIS Experiment**

Devant le jury composé de :

Corinne Augier, Professeure des Universités, Université Lyon1

Gemma Testera, INFN First Researcher

David Lunney, Directeur de recherche CNRS, CSNSM

Michaël Beuve, Professeur des Universités, Université Lyon1

Markus Oberthaler, Professeur des Universités, Université de Heidelberg

Patrick Nedelec, Professeur des Universités, Université Lyon1

Président du jury

Rapporteur

Rapporteur

Examineur

Examineur

Directeur de thèse

Thèse

présentée devant

l'Université Claude Bernard Lyon 1

École Doctorale de Physique et d'Astrophysique

pour l'obtention du

DIPLÔME de DOCTORAT
Spécialité : Physique

(arrêté du 7 août 2006)

par

Pierre LANSONNEUR

Défectométrie Moiré d'Ions de Basse Énergie pour l'Expérience AEGIS

Moiré Deflectometry with a Low-Energy Ion Beam for the AEGIS Experiment

Soutenue le 5 Octobre 2017
devant la Commission d'Examen

Jury :	C. Augier	Président du jury
	G. Testera	Rapporteur
	D. Lunney	Rapporteur
	M. Beuve	Examineur
	M. K. Oberthaler	Examineur
	P. Nedelec	Directeur de thèse

Abstract

Although numerous experiments investigate the properties of antimatter in the weak, strong and electromagnetic sector, the gravitational interaction of antiparticles is still an open question. By observing the free-fall of antihydrogen atoms, the AEGIS experiment plans to perform the first measurement of the gravitational acceleration on antimatter. The device envisioned for such an experiment consists of a set of three transmission gratings with a pitch of few micrometers, associated with a high resolution imaging detector. This thesis focuses on testing such a device with a low-energy ion beam, enabling one to measure simultaneously the magnitude of surrounding electric and magnetic fields. An effort is moreover initiated to perform the same experiment with smaller grating periodicities since it could reveal the quantum interference of the ions. In order to probe the quantum behavior of protons, the effects which might destroy the interference pattern are reviewed and discussed. We finally detail the implementation of a velocity selector and a silicon detector dedicated to low energy antiprotons. These two components are indeed a prerequisite to perform for the first time the interference of antimatter particles.

keywords: very low-energy, moiré effect, interference.

Résumé

Bien que les propriétés de l'antimatière soient largement testées dans le secteur faible, fort et électromagnétique, l'interaction gravitationnelle des antiparticules est encore bien mal connue. En observant la chute libre d'atomes d'anti-hydrogène, l'expérience AEGIS prévoit de mesurer pour la première fois l'accélération gravitationnelle de l'antimatière. Le dispositif prévu pour cette mesure se compose de trois réseaux en transmission et d'un détecteur possédant une haute résolution spatiale. Le travail de cette thèse se concentre sur la caractérisation d'un tel dispositif avec une source d'ions de basse énergie, permettant de mesurer simultanément les champs électriques et magnétiques environnant. Une attention particulière est également portée sur l'implémentation de l'expérience avec des réseaux de pas plus fin, afin de mettre en évidence l'interférence quantique des ions. Les effets qui pourraient réduire le contraste des franges d'interférences sont passés en revue et discutés. Enfin, la réalisation d'une ligne de faisceau capable de sélectionner des particules de basse énergie et l'intégration d'un détecteur silicium dédié à la détection d'antiprotons est détaillée dans le but de réaliser pour la première fois l'interférence de particules d'antimatière.

mots-clés: très basse énergie, effet de moiré, interférence.

Acknowledgements

One tends to forget that a PhD is a collective task. This work could not have been performed without the involvement of some remarkable people. The first thanks goes to my supervisor, Patrick Nedelec, for the chance he gave me and the assistance he provided throughout the whole PhD. I express also my gratitude to:

- Gemma Testera and David Lunney, who accepted to evaluate my thesis,
- all the members of the Institut de Physique Nucléaire de Lyon (IPNL) that were involved in the project, especially Romain, Rodolphe, Patrice and Houmani,
- Pascal Sortais and Thierry Lamy for their technical support with the ion source,
- the IPNL ion beam service and the electronic service, who designed and built the ion beamline,
- Michael Doser, who offered me the opportunity to work at CERN,
- Stefan Häider for, should it be mentioned, his indulgence about the (rare) "bri-co-la-ges" on the source,
- Jacky Rochet for his support and his availability at CERN,
- Benji, Ola, Ruggero (the positron little chickens), Seba (the mummy chicken), Julian, Sebastian, Pauline and all the members of the AEGIS collaboration.

I crossed the path of valuable colleagues at the Kirchoff Institute for Physics of Heidelberg (Germany), where a large part of this work was done. I address them sincere thanks for hosting me almost two years. Especially to:

- Markus Oberthaler, for his supervision and the encouragements he gave since the beginning of the project,
- Philippe, who triggered the proton interferometry experiment during a coffee break at CERN: *"a small project which will probably last no more than a few weeks"*,
- Andrea, Simon and Patrick, the other proton fringe seeker,
- Helmut, for the technical help on almost every physics-related topic,
- Dagmar and Christiane who considerably simplified my life when I arrived in Heidelberg,
- Lisa Veith, Anne Kast and Pr Rasmus Schröder for the SEM pictures of the gratings,
- Alban Kellerbauer and Giovanni Cerchiari for loaning us their detector,
- the whole matterwave group who created a great atmosphere and tasty barbecue parties!

To Matthew for the English corrections.

A ma famille. En particulier, à mes parents.

Never say never.
Justin Bieber

Contents

Abstract	5
1 Introduction	11
2 Motivations	13
2.1 Gravitation and antimatter, why it does matter	14
2.1.1 Matter/antimatter imbalance	14
2.1.2 Composition of our universe	14
2.1.3 Sakharov conditions	15
2.1.4 A repulsive gravity?	15
2.2 Probing antimatter properties on Earth	16
2.2.1 Antiproton annihilation	16
2.2.2 The Antiproton Decelerator at CERN	16
2.2.3 Limits on g for antimatter	18
2.3 The AEGIS experiment	21
2.3.1 Positronium formation and excitation	22
2.3.2 Antiproton manipulation	23
2.3.3 Charge-exchange reaction	24
2.3.4 The hydrogen detector	24
2.3.5 Measuring $g(\bar{H})$	29
2.4 Summary	30
3 Moiré Deflectometry and Talbot-Lau Interferometry	31
3.1 Moiré concepts	32
3.1.1 Fringe pattern of two gratings	32
3.1.2 Magnification with a third grating	33
3.2 Probing electric and magnetic field	34
3.2.1 Deflection by a magnetic field	35
3.2.2 Decoupling electric and magnetic components	36
3.2.3 Resolution limit	36
3.2.4 Critical fields	37
3.2.5 Detector resolution	38
3.2.6 Field correcting factor	39
3.3 Talbot-Lau interferometry with protons	41
3.3.1 Motivations	42
3.3.2 Talbot-Lau interferometer	42
3.3.3 Visibility modulations	45
3.4 Summary	45

3.4.1	Moiré fieldmeter	45
3.4.2	Talbot-Lau interferometer	46
4	Experimental Setup	49
4.1	Overview	50
4.2	Ion beamline	51
4.2.1	Ion source	52
4.2.2	Gas composition	54
4.2.3	Faraday cup	55
4.2.4	Operating settings	55
4.2.5	Energy spread	57
4.2.6	Beam size	59
4.2.7	Mass spectrum	61
4.3	Neutralization chamber	63
4.4	Interferometer	65
4.4.1	Magnetic shield	66
4.4.2	Gratings	67
4.4.3	Alignment	70
4.5	Detector	72
4.5.1	Microchannel plate	73
4.5.2	Resistive anode	73
4.5.3	Phosphor screen and camera	74
4.5.4	Efficiency	77
4.5.5	Spatial resolution	78
4.6	Summary	81
5	Fields Measurement and Discussion	83
5.1	Field measurements	84
5.1.1	Fields acting in the interferometer volume	84
5.1.2	Comparison with a known magnetic field	85
5.1.3	Expected visibility of the interferometric fringes	86
5.2	Shift ambiguity and maximal field	87
5.3	Charge-up effects	87
5.4	Summary	88
6	Toward an Antiproton Interferometer	89
6.1	The ATLIX experiment specificities	90
6.2	The antiproton deceleration beamline	90
6.2.1	Energy range	91
6.2.2	AD beam monitoring	92
6.2.3	Degrader	94
6.2.4	Position of the interferometer	96
6.2.5	Operating settings	96
6.2.6	Energy spread	98
6.3	The Timepix detector	99
6.3.1	High resolution imaging detectors for particle tracking	99
6.3.2	General characteristics	100
6.3.3	Tagging efficiency	101
6.3.4	Spatial resolution	101
6.4	ATLIX feasibility	103

6.4.1	Expected flux and acquisition time	103
6.4.2	Critical fields	103
6.5	Summary	104
7	Conclusion	105
	Appendices	119
A	Hough Transform	121
B	Software	123
C	Constants	125

1 | Introduction

In physics, every phenomenon can be reduced to one of the four fundamental forces: the weak interaction (responsible for some nuclear phenomena such as radioactivity), the strong interaction (holding the nucleons of an atom together), electromagnetism (accounting for the interactions between electrically charged particles) and gravitation (causing for instance the apples fall on Earth). As presented in table 1.1, while the first three interactions are described by the Standard Model of particle physics, General Relativity is the theory accounting for gravitational interaction. Note that gravitation is by far the weakest of the four interactions: compared to the strong force, effects induced by gravity are indeed weaker by almost 40 orders of magnitude!

Interaction	Strong	Electromagnetic	Weak	Gravitation
Theory	Standard Model of particles physics			General Relativity
Particles mediating	gluons	photons	W^\pm, Z^0 bosons	graviton
Range	10^{-15} m	∞	10^{-12} m	∞
Approx. relative strength	1	10^{-2}	10^{-13}	10^{-38}

Table 1.1: The four fundamental interactions and their characteristics. Gravitation, described by General Relativity, is by far the weakest interaction.

At the heart of General Relativity, the weak equivalence principle states that all bodies placed in a gravitational field fall with the same acceleration, independently of their internal composition. It will be shown in chapter 2 that this principle has been verified with remarkable precision with matter. But in 1933, the discovery of the positron, the anti-particle of the electron, raised an important question: is this principle also verified for antimatter? Thanks to the recent developments on antihydrogen physics carried out at CERN, studying the effect of gravity on neutral antimatter seems today feasible.

By observing the free-fall of antihydrogen atoms, the AEGIS (Antimatter Experiment: Gravity, Interferometry, Spectroscopy) experiment plans to measure for the first time the gravitational acceleration of antimatter on Earth. In the AEGIS setup, the antihydrogen atoms are produced by the charge-exchange reaction of antiprotons with positronium, a bound state of an electron and a positron. The various manipulations of these different particles are monitored by the mean of the hydrogen detector, a detector developed partially by the author. Once the antihydrogen atoms are produced, the device envisioned to perform the gravity measurement is a moiré deflectometer. It consists of a set of three transmission gratings associated with a high-resolution imaging detector. This thesis focuses on testing such a device with a low-energy ion beam.

Although the moiré deflectometer is perfectly apt to measure gravitational effects, we describe in chapter 3 another application of the apparatus. Indeed, under certain conditions, the deflectometer allows one to measure simultaneously the magnitude of surrounding electric and magnetic fields. The working principle and the mathematical framework of the moiré “fieldmeter” are hence detailed. Thanks to the moiré effect appearing between the gratings, it appears moreover that this apparatus is competitive with state-of-the-art fieldmeters.

Depending on the gratings periodicity (or pitch), we show then that the deflectometer can work in different regimes. Indeed, when the distance between the gratings get close to a certain scale (known as the Talbot length) that will be presented, the quantum behavior of the ions can be revealed. In opposition to the moiré deflectometer, the trajectory of the ions between the gratings are no longer defined in this regime. Instead, the probability of detecting a particle at a certain location exhibits a characteristic quantum interference pattern, known as the “Talbot carpet”.

Since no results concerning the interference of charged particles heavier than electrons have been reported, we introduce in chapter 4 the Proton Interferometry eXperImEnt (PIXIE) to fill in this gap. It consists in a low-energy ion source delivering (among other particles) protons, the interferometer and the detector. A moiré fieldmeter is also integrated to the setup to measure in real time the magnitude of stray electric and magnetic fields, which might disturb the interference pattern.

The results of the fieldmeter are presented in chapter 5. The fields acting in the volume of the interferometer are measured and used to reevaluate the signal of the interferometer. The reliability of the fieldmeter is then tested with a known magnetic field.

We finally ponder in the last chapter how the PIXIE experiment, currently developed for protons, could be operated equivalently with antiprotons. We detail for this purpose the implementation of a velocity selector and a silicon detector dedicated to low energy antiprotons. These two components are indeed a prerequisite to perform for the first time the interference of antimatter particles.

2 | Motivations

In the early age of the Universe, it seems that Nature has favored matter to the detriment of antimatter, forming the world we know today. Whatever the cause of this imbalance, it is extremely fortunate for us: without it, no stars or people would exist. What happened to antimatter? A possible scenario is that annihilation made the asymmetry much greater today than it was in the early universe. If the asymmetry was tiny during the first microseconds following the Big Bang, most of the antimatter has annihilated with matter then, leading to the very large excess of matter visible today. But another explanation could be that gravitation acts very differently from what we know, when it deals with antimatter. Introducing for instance a repulsive gravity, it is not excluded that there exist regions of the universe in which matter is dominant, and other regions of the universe in which antimatter is dominant, widely separated one from the other. After a review of the observational evidence for a matter-antimatter imbalance in the universe, we present in this chapter how the properties of antimatter are tested experimentally on Earth. More particularly, measuring the effect of gravitation on such objects seems today feasible thanks to the recent developments on antihydrogen physics. We present in the last section the AEGIS experiment (Antimatter Experiment: Gravity, Interferometry, Spectroscopy), which plans to measure for the first time the gravitational acceleration of antihydrogen atoms on Earth.

2.1 Gravitation and antimatter, why it does matter

Numerous questions remain about the origin of antimatter. Why do we not observe matter and antimatter in equal amounts? Is it possible that antimatter challenges our understanding of gravitation? Could a difference with ordinary matter explain the expansion acceleration of the universe? We present in this section what are the stakes of measuring gravitational interaction of antimatter.

2.1.1 Matter/antimatter imbalance

With the aim of solving the equation describing the electron in both relativistic and quantum mechanical frame, Paul Dirac in 1928, found surprisingly two solutions [1]. If one represented indeed the electron, the other described the same particle but with opposite charge. Although Dirac thought originally that this solution could describe the proton [2], he quickly abandoned the idea and postulated in 1931 the existence of a new particle, the positron [3] (anti-partner of the electron). Only one year later, the existence of the positron was confirmed experimentally by Anderson [4]. Soon followed the discoveries of many antiparticles, such as pions [5] or kaons [6], the antiproton in 1955 at the Bevatron [7], the antineutron in 1956 [8] and the first anti-nucleus (anti-deuteron) announced in 1965 by both Brookhaven Laboratory and CERN [9, 10]. It has been since verified experimentally that every known kind of particle has a corresponding antiparticle.

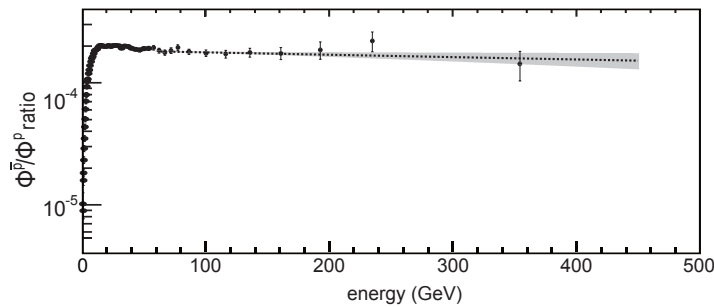


Figure 2.1: The (\bar{p}/p) flux ratio measured in cosmic rays as a function of the energy (from reference [12]). For energies above 20 GeV, the fraction of antiproton is almost constant, of the order of $2 \cdot 10^{-4}$.

Several observations indicate that matter particles outnumber significantly those of antimatter in the near universe. The PAMELA [11] and AMS [12] missions, launched respectively in 2006 and 2011, measured that the flux of positrons in cosmic rays (energetic particles traveling through the interstellar medium) is about 100 times smaller than the flux of electrons. Similarly, the fraction of antiprotons remains constant, of the order of $2 \cdot 10^{-4}$ over a large range of energy, as seen on figure 2.1.

2.1.2 Composition of our universe

Based on the relative peak positions in the cosmic microwave background spectrum and the relative abundance of the lightest elements, it is today admitted that the matter we are made of represents only 4 % of the total mass/energy of the universe. The 96 % remaining are shared between dark matter (23 %), introduced to explain the anomaly observed in galactic rotation curve, and dark energy (73 %) revealed by recent (1998) observation of supernovae "standard

candles" showing an accelerated expanding Universe [13, 14]. Since no particle candidates have been found so far for the dark matter, and the origin of dark energy is unclear, a large part of our universe remains hence unknown.

2.1.3 Sakharov conditions

The antimatter imbalance can be explained if there exists some process that favored matter over antimatter, leading to the excess that we see today. In 1967, Sakharov enumerated the three necessary conditions for an initial matter/antimatter asymmetry to occur [16]:

- **Baryon number violation.** In particle physics, the baryon number is a conserved quantum number. It is defined as $B = \frac{1}{3}(n_q - n_{\bar{q}})$, where n_q is the number of quarks, and $n_{\bar{q}}$ is the number of antiquarks of a hadron. Baryons (made of three quarks) have a baryon number of +1, mesons (one quark, one antiquark) have a baryon number of 0, and antibaryons (three antiquarks) have a baryon number of -1. Baryon number violation is obviously needed to achieve a baryon asymmetry;
- **C and CP violation.** CP-symmetry states that the laws of physics are identical if a particle is interchanged with its antiparticle (C-symmetry) and its spatial coordinates are inverted (P-symmetry). Without C and CP violation, the violation of baryon number in a random process $A \rightarrow B$ would be compensated by the equal amount of violation in the conjugated process $\bar{A} \rightarrow \bar{B}$;
- **System out of thermodynamic equilibrium.** If the system is in thermodynamic equilibrium, the rates of the process violating the baryon number $A \rightarrow B$ and its back reaction $B \rightarrow A$ are the same. Thermodynamic nonequilibrium is hence a necessary condition to prevent such a counterbalance.

But one should keep in mind that, although C and CP violations were observed experimentally [15, 17], no process violating the baryon number has been observed so far. Could a simpler mechanism be at the origin of the matter-antimatter imbalance?

2.1.4 A repulsive gravity?

Besides the conditions listed by Sakharov, the asymmetry observed could be the consequence of a repulsive gravity between matter and antimatter. With such an hypothesis, we could imagine that regions of the universe are dominated by matter while other regions of the universe would be made of antimatter, the two being repelled one from the other. This idea is not new. Even before its prediction by Dirac, the existence of "anti-atoms" presenting a different gravitational interaction was discussed by A. Schuster in 1898. In a letter to Nature, he wrote [18]:

"If there is negative electricity, why not negative gold, with [...] identical spectral lines, different only in so far that if brought down to us it would rise up into space with an acceleration of 981 [cm/s²]."

Furthermore, the force induced by a matter-antimatter repulsion would explain why the universe is expanding at an accelerating rate, eliminating the need for dark energy. The Dirac-Milne universe is a theoretical model where matter and antimatter are present in equal amount along with a repulsive gravitational interaction [19]. It is remarkable that such a model, with minimal assumptions, is able to retrieve the relative abundance of the lightest elements (lithium, beryllium), therefore in agreement with the primordial nucleosynthesis

measurements, but also the age of the universe and the scale of the first peak of the CMB. A repulsive gravity between matter and antimatter is however not approved unanimously: reference [20] reviews the few theoretical predictions for the gravitational interaction of antimatter.

2.2 Probing antimatter properties on Earth

The imbalance of matter and antimatter in the universe, as well as the lack of knowledge about its composition, motivates the search for new physics in the antimatter sector. To elucidate the questions raised in the previous section, we present now a unique facility to test antimatter properties on Earth: the Antiproton Decelerator (AD) and its future extension, the Extra Low ENergy Antiproton (ELENA) ring. After a review of the direct and indirect limits on the gravitational constant g for antimatter, we will see that antihydrogen atoms (\bar{H}) are suitable candidates to measure gravitation induced effects. The last section introduces the AEGIS experiment [21], which plans to measure $g(\bar{H})$ by looking at the vertical deflection (induced by gravity) on a beam of antihydrogen.

2.2.1 Antiproton annihilation

Annihilation is the phenomenon appearing when a particle encounters its anti-partner. Although “annihilation” should be understood as a vanishing, the particle and its anti-particle do not transform into nothing. To fulfill both energy and momentum conservation, additional particles are indeed produced. When a nucleon annihilates with an antiproton (bound system of one quark anti-down \bar{d} and two quarks anti-up \bar{u}) the internal constituents of the nucleons rearrange themselves. Hence, the annihilation of an antiproton leads to the production of charged pions:

$$\begin{aligned}\pi^- &= \bar{u}d, \\ \pi^+ &= u\bar{d},\end{aligned}\tag{2.1}$$

neutral pions:

$$\pi^0 = \frac{1}{\sqrt{2}}(u\bar{u} - d\bar{d}),\tag{2.2}$$

and seldom kaons (composite particles made of s quarks). The result of an antiproton-nucleon annihilation is hence the transition from interacting baryons to a system composed entirely of mesons [142]. The pion final-state branching ratios (BR) for antiproton-proton and antiproton-neutron annihilations at rest are listed in table 2.1. On average, an isolated antiproton-proton annihilation produces $1.5 \pi^+$, $1.5 \pi^-$ and $2 \pi^0$ particles, while an antiproton-neutron annihilation produces $1 \pi^+$, $2 \pi^-$ and $2 \pi^0$ particles [143, 144].

For particles having a few keV of energy, this process typically occurs after several collisions into the material. It is hence much more likely that an antiproton annihilates in the nucleus of a heavy atom. In that case, the exiting pions can possibly be absorbed by the nucleus, or even trigger its fragmentation.

2.2.2 The Antiproton Decelerator at CERN

Investigating the properties of antimatter would not have been possible without the use of dedicated facilities, such as the Antiproton Decelerator (AD). Built in 1996 to replace the Low-Energy Antiproton Ring (LEAR [23]), this storage ring delivers bunches of approximately $3 \cdot 10^7$ antiprotons at an energy of 5.3 MeV every 110 s [24].

antiproton-proton ($p\bar{p}$)		antiproton-neutron ($n\bar{p}$)	
pions final state	BR (%)	pions final state	BR (%)
$\pi^0 \pi^0$	0.28	$\pi^- \pi^0$	0.75
$\pi^0 \pi^0 \pi^0$	0.76	$\pi^- k\pi^0$ ($k > 1$)	16.9
$\pi^0 \pi^0 \pi^0 \pi^0$	3	$\pi^- \pi^- \pi^+$	2.3
$\pi^- \pi^+$	0.32	$\pi^- \pi^- \pi^+ \pi^0$	17
$\pi^- \pi^+ \pi^0$	6.9	$\pi^- \pi^- \pi^+ k\pi^0$ ($k > 1$)	39.7
$\pi^- \pi^+ \pi^0 \pi^0$	9.3	$\pi^- \pi^- \pi^+ \pi^- \pi^+$	4.2
$\pi^- \pi^+ \pi^0 \pi^0 \pi^0$	23.3	$\pi^- \pi^- \pi^+ \pi^- \pi^+ \pi^0$	12
$\pi^- \pi^+ \pi^0 \pi^0 \pi^0 \pi^0$	2.8	$\pi^- \pi^- \pi^+ \pi^- \pi^+ k\pi^0$ ($k > 1$)	6.6
$\pi^- \pi^+ \pi^- \pi^+$	6.9	$\pi^- \pi^- \pi^+ \pi^- \pi^+ \pi^- \pi^+ k\pi^0$ ($k \geq 0$)	0.35
$\pi^- \pi^+ \pi^- \pi^+ \pi^0$	19.6		
$\pi^- \pi^+ \pi^- \pi^+ \pi^0 \pi^0$	16.6		
$\pi^- \pi^+ \pi^- \pi^+ \pi^0 \pi^0 \pi^0$	4.2		
$\pi^- \pi^+ \pi^- \pi^+ \pi^- \pi^+$	2.1		
$\pi^- \pi^+ \pi^- \pi^+ \pi^- \pi^+ \pi^0$	1.9		

Table 2.1: Branching ratios of pion final states from antiproton-proton [144] and antiproton-neutron [145] annihilation at rest (the k denotes the grouping together of multiple π^0 channels). Note that the kaons contribution ($\sim 2\%$) is ignored here (from reference [146]).

It works as follows. A primary beam of 10^{13} protons, with momentum of 26 GeV/c is firstly supplied by the CERN Proton Synchrotron. The beam is then directed toward a target, consisting of a thin iridium rod embedded in graphite [25], and antiprotons are created by the reaction:



The antiprotons, produced along with many other particles, are then collected by a magnetic horn¹ in the region upstream of the target [25]. The few 10^7 antiprotons are then injected into the AD where they are decelerated. To slow down the antiprotons from 3.6 GeV to 5.3 MeV, an alternating electric field is opposed to the motion of the particles, in a set of RF cavities. Note that a side-effect of this step is to widen the momentum spread of the antiprotons. Stochastic cooling [27, 28] and electron cooling [29] are then used to reduce the consequent momentum spreading. Developed by S. Van der Meer, stochastic cooling relies on two elements: a sensor, measuring the position distribution of the beam, and a kicker, which by the mean of electric field pushes the particles toward an ideal orbit of the ring at each turn. Electron cooling, on the other hand, deals with the injection of electrons into the AD ring with a velocity matching the one of the antiprotons. The antiprotons are then able to transfer their energy to the electrons through successive collisions. The electrons are finally removed, taking with them the excess of energy. Within an AD cycle, the stochastic cooling is first performed when the antiproton energy is 3.6 GeV and 2 GeV followed by electron cooling at 300 MeV and 100 MeV [24]. A whole cycle lasts in average 110 sec.

¹a horn-shaped aluminum plate carrying a current of approximately 400 kA.

An additional stage of deceleration, located upstream of the AD is currently commissioned at CERN. In the years to come, the Extra Low ENergy Antiproton ring (ELENA) will further slow down the antiprotons from 5.3 MeV to 100 keV [30]. The ELENA cycle, consisting of two stages of RF deceleration followed by electron cooling, will last only 20 s [30]. With this new facility, the number of antiprotons that can be trapped within the different experiments should be enhanced by a factor of 10 to 100. A schematic view of the antiproton decelerator with the different steps of preparation for the beam, the AEGIS experimental zone and the new ELENA facility is shown in figure 2.2.

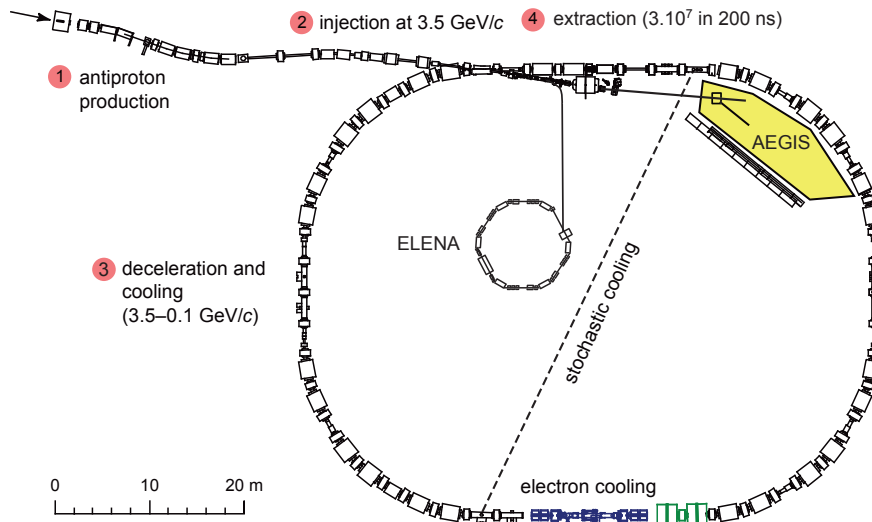


Figure 2.2: Schematic view of the antiproton decelerator with the different steps of preparation for the beam, including stochastic and electron cooling. The layout of the current AEGIS experimental zone and the new ELENA facility are also drawn (image adapted from [26]).

2.2.3 Limits on g for antimatter

The weak equivalence principle (WEP) states that all bodies placed in a gravitational field fall at the same acceleration, independently of their internal composition². Note that another (equivalent) formulation of the WEP is the equality of the inertial mass, written in the second law of Newton, and the gravitational mass, written in the expression of the gravitational force. It is important to notice that this principle is a cornerstone of the theory describing gravitation currently, the General Relativity. Any deviation Δg from the known value³ $g = 9.80876 \text{ m}\cdot\text{s}^{-2}$ would therefore be a major breakthrough in our understanding of gravity.

As shown in figure 2.3, the weak equivalence principle has been extensively tested for ordinary matter since the 16th century. Torsion balances, measuring the torque induced by two masses of different material on a wire are today the most precise experiments performed on Earth. Performed in vacuum, the most updated devices reach typically a precision of 10^{-13} on $\Delta g/g$ [34]. To constrain the WEP even more, new experiments have been carried recently

²It is the famous experiment of Galileo, who showed from the top of the (Pisa?) tower that blocks of different material fall at the same speed.

³Latest measurements indicate that the Earth gravitational field may vary by up to 0.56 % depending on location [32]. The value presented here is computed for Geneva, Switzerland [33].

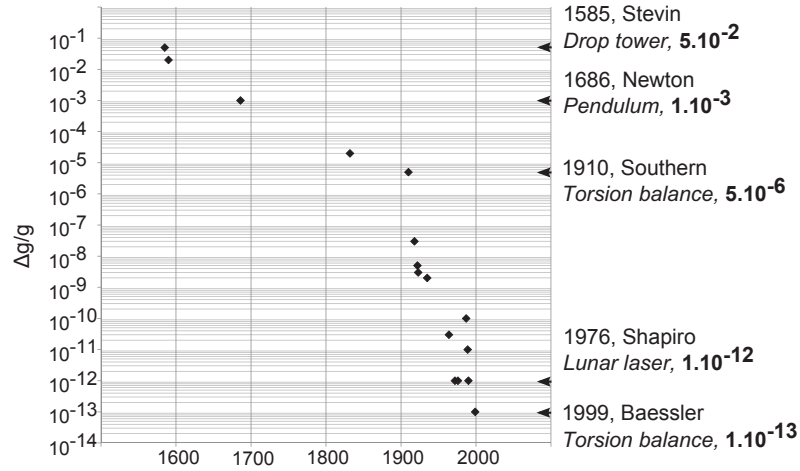


Figure 2.3: The experimental constraints on the weak equivalence principle for ordinary matter since the 16th century. The most stringent experiments until now (torsion balances) achieve a precision of 10^{-13} on $\Delta g/g$ by measuring the torque induced by two masses of different material on a wire. The MICROSCOPE satellite mission [35], launched in 2016 should push further the limits on $\Delta g/g$ to 10^{-15} by comparing the gravitational acceleration of two test masses of titanium and platinum/rhodium in space.

in space. The MICROSCOPE satellite, launched in 2016 should for instance push the limit to 10^{-15} by comparing the gravitational acceleration of two test masses of titanium and platinum/rhodium [35]. Similarly, the STEP satellite, proposed in 2012, is designed to reach a sensitivity of 10^{-18} on $\Delta g/g$ [36]. But whereas the WEP is extremely well tested for matter, experimental limits on g are much rarer for antimatter.

Indirect limits

Indirect tests of the weak equivalence principle for antimatter have been performed by comparing the properties of particles and their antiparticles. By looking at the decays of $K_0 - \bar{K}_0$ system into pions as a function of time, the CPLEAR collaboration was able to state that the principle of equivalence between particles and antiparticles holds to a level of few 10^{-9} [37]. Another indirect limit results from the comparison of the cyclotron frequency between a particle and its anti-partner. When placed in a gravitational potential U , the cyclotron frequency of a charged particle (mass m , charge q) in a magnetic field B is given by:

$$\omega = \frac{qB}{2\pi m} + \frac{U}{c^2} \quad (2.4)$$

Although this second term is negligible in most of the cases, reference [38] states that it can instead get significant if one considers the attraction of the local galaxy supercluster. By comparing the cyclotron frequency of protons and antiprotons in the same magnetic field, reference [39] measured a difference $(\omega_p - \omega_{\bar{p}})/\omega_p \leq 10^{-11}$ translating into a maximal observable difference of 10^{-6} for $\Delta g/g$. But as discussed by reference [38] and [20], these tests are all model-dependant and rely upon disputable theoretical hypothesis.

Direct limits: attempts and proposals

Several attempts to measure gravity directly were made in the past with charged particles but lead to large uncertainties mainly due to difficulties to control coulombian effects. In 1967,

Fairbank and Witteborn proposed an experiment to measure the gravitational acceleration of electrons inside a metal drift-tube [41]. In their setup, the time-of-flight of ultra-slow electrons, launched upwards, was measured and enabled one to retrieve the g constant. Although the same experiment could have in principle been conducted with the antimatter counterpart, the lack of low-energy positron sources available at that time made the community forsake the idea. Later in the 1990's, the PS200 collaboration attempted to perform a similar experiment but with antiprotons from the Low Energy Antiproton Ring [42]. Since antiprotons are about 2000 times more massive than positrons, the requirements on the electric and magnetic shielding of the experiment would have been reduced by three orders of magnitude [43]. However, the experiment struggled to overcome the effect of electric field gradients, due to irregularities in the crystalline structure on the inner surface of the drift tube (patch-effect).

What about neutral antiparticles? It seems out of present reach to perform experiments with antineutrons, because of the difficulty to slow them down [44]. Among the other neutral candidates, the positronium, bound state of electron and positron, was for a long time disregarded because of its high polarizability (hence sensitive to stray field) and its limited lifetime. However, the recent achievement of metastable positronium (with lifetime in the millisecond range) opens the road to new experiments. Some experiments are currently proposed using inhomogeneous field to select specific configurations of the positronium [46] or looking at the gravitational deflection of a positronium beam [47].

The advent of antihydrogen

Antihydrogen atoms are the next simplest neutral baryonic candidates. Since its production for the first time⁴ in 1995, antihydrogen has become a probe of choice for antimatter. While the first atoms were produced at an energy too large for its properties to be studied, an extensive effort has been made over the past decades to store and cool antihydrogen. In 2002, the ATRAP and ATHENA collaborations announced the production of cold antihydrogen, at several hundred of Kelvin [50, 49]. Reaching such a low temperature allowed one to employ various techniques from atomic physics to perform innovative experiments. In 2011, the ALPHA collaboration announced that they had trapped 309 antihydrogen atoms, some for time as long as 1000 seconds [51]. More recently, the transition between the two lowest energy levels of antihydrogen (1S - 2S) was measured [52].

Soon, the cooling of these objects at sub-Kelvin temperatures allowed to design the first experiments dealing with gravitation. In 2013, the ALPHA collaboration measured the top/bottom asymmetry of the annihilations when releasing an ensemble of antihydrogen at temperature of 0.5 K. They were thereby able to constrain for the first time the gravitational acceleration for antimatter to $g(\bar{H}) =_{-65}^{110} g$ with a 95 % confidence level [53]. Although this range might seem large, it represents the first direct limit on gravity for antimatter.

To reduce the uncertainty on $g(\bar{H})$, two experiments have been approved at CERN: the AEGIS (Antimatter Experiment: Gravity, Interferometry, Spectroscopy) experiment [21] and the GBAR (Gravitational Behavior of Antihydrogen at Rest) experiment [54]. In the GBAR setup, \bar{H}^+ ions, the antimatter counterpart of H^- , are produced by two successive charge-exchange reactions with positronium. After being cooled down to sub-Kelvin temperature, the excess positron is photo-detached by a laser shot such that the \bar{H} can free fall in a Time-Projection Chamber. In a future stage, the GBAR collaboration may implement the quantum bounces of the antihydrogen atoms on a surface plane to push further the limits on $g(\bar{H})$.

⁴The PS210 collaboration observed 11 atoms of antihydrogen [48]. That first observation was truly a prowess since only 48 hours of beamtime were allocated to the experiment for the antihydrogen production!

2.3 The AEGIS experiment

The AEGIS experiment [21] (Antimatter Experiment: Gravity, Interferometry, Spectroscopy) plans to measure the gravitational acceleration of antimatter on Earth, by observing the free-fall of antihydrogen atoms. The challenging idea is to produce a beam of cold antihydrogen (\bar{H}) by a charge-exchange reaction involving antiprotons (\bar{p}) and positronium (Ps, a bound-state of electron and positron). The different steps of the experiment, sketched on figure 2.4, are the following:

1. Every 110 s, the AD delivers around $3 \cdot 10^7$ antiprotons which are decelerated by crossing a thin metallic foil. A small fraction (few percent) is then captured and cooled;
2. Positrons emitted by a radioactive ^{22}Na source are ejected onto a mesoporous silica target to form a dense positronium cloud. Once formed, the positronium is excited by two lasers to a Rydberg state with typical $n = 30 \sim 40$;
3. Antihydrogen atoms are formed according to the charge-exchange reaction:



The reaction offers two advantages. Firstly, large rates of \bar{H} can be reached since the corresponding cross-section scales as $n^4 P_s$ with n_{P_s} the principal quantum number of Ps. Moreover, as the principal quantum number of \bar{H} is linked to n_{P_s} , final state can be controlled by tuning the lasers excitation;

4. Antihydrogen atoms passing through a set of transmission gratings will impinge a fringe pattern on a dedicated detector. By comparing the position of the fringes with a reference insensitive to gravity (for instance light), the g constant will finally be retrieved. In order to reduce the uncertainty on the velocity of the antihydrogen atoms, the whole experiment is performed in a cryogenic environment and in ultra-high vacuum.

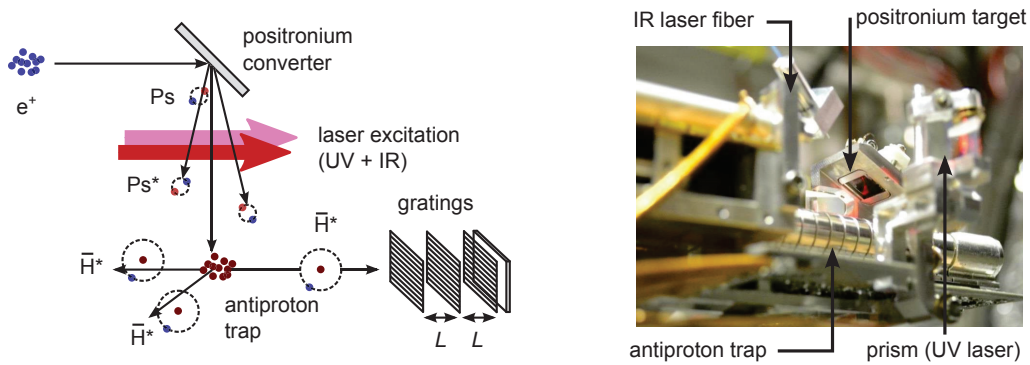


Figure 2.4: Schematic view of the AEGIS experimental protocol and photograph of the \bar{H} production area. Positrons, emitted by a radioactive ^{22}Na source, propagate onto a mesoporous silica target to form a dense positronium cloud. The positronium (Ps) hence formed is then excited by two lasers to Rydberg state Ps^* ($n = 30$ to 40). The antihydrogen atoms, planned to be formed by charge-exchange reaction between cold antiprotons and the excited positronium, are then passing through a set of three transmission gratings to measure $g(\bar{H})$. On the photograph is displayed the ring shaped electrodes of the production trap, the positronium converter and the fiber carrying the infrared laser (in blue). The prism on which the ultra-violet laser is reflected is visible on the side.

2.3.1 Positronium formation and excitation

Positrons, emitted by a 11 mCi ^{22}Na source, are slowed down to a few eV by a solid neon moderator. After a dedicated compression, bunches containing $3 \cdot 10^7$ positrons each are transported toward a magnetic-field-free region. They are then recompressed into a pulse of about 7 ns and accelerated toward the porous silicon target [55]. Positronium is then formed at the surface of the pores when a positron captures an electron of the silicon substrate.

Depending on the relative alignment of the electron and the positron spins, positronium can be produced into two configurations. While the para-positronium (with anti-aligned spins) annihilates within 125 ps, the ortho-positronium, triplet state of parallel spins, has a particularly long lifetime of 142 ns. To detect the formation of ortho-positronium nearby the target, the three gamma resulting from the annihilation of the electron and the positron are observed by the mean of plastic scintillators surrounding the AEGIS apparatus. The technique of Single Shot Positron Annihilation Lifetime Spectroscopy (SSPALS) allows then one to extract the lifetime of positronium from the spectrum of the annihilation counts as a function of time (referenced to the time of the positrons release).

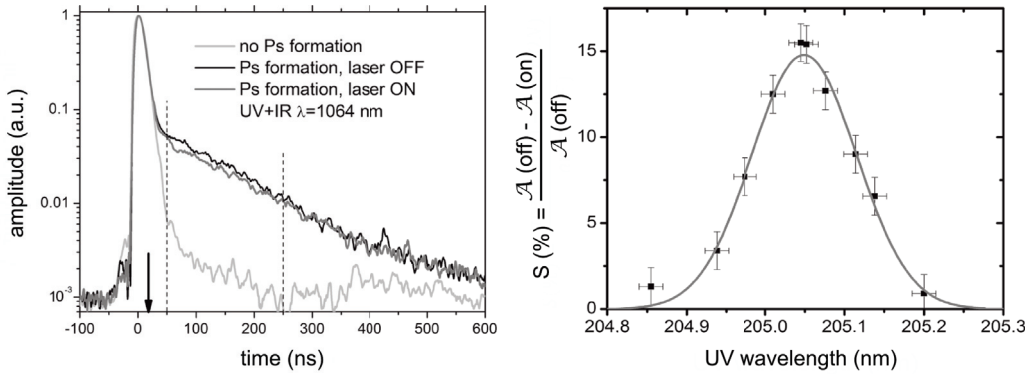


Figure 2.5: (left) SSPALS spectra of Ps into vacuum with laser OFF (black) and UV+IR lasers ON (205.05 + 1064 nm) (dark gray). The arrow marks the time when the laser is shot on the Ps cloud. (right) Linewidth of the 1S - 3P Ps excitation obtained by scanning the UV laser wavelength for constant IR wavelength. The y axis is the relative difference of the area comprised below the SSPALS spectra when the laser is ON or OFF. While a ray at exactly 205.05 nm should be observed for a positronium produced at rest, the thermal agitation of the Ps cloud causes a broadening of the line (Doppler Broadening). Data from reference [55].

To increase the cross-section of the charge-exchange reaction, the positronium is excited by two lasers. An ultra-violet laser (wavelength $\lambda = 205$ nm) excites first the positronium from ground state to $n = 3$ while the transition from $n = 3$ to $n \sim 35$ is managed by an infrared laser ($\lambda = 1064$ nm). The SSPALS spectrums of positronium with and without laser excitation are displayed in figure 2.5 (left). The linewidth of the 1S - 3P excitation (right) is obtained by comparing the area below the two curves as a function of the ultra-violet laser wavelength. As thermal agitation moves the positronium atoms either away or toward the laser, the transition wavelength can be either blue-shifted or red-shifted (Doppler broadening). Such a curve gives hence an insight about the velocity distribution of the positronium cloud. A proper modeling allows one to extract from this curve the spread in velocity of the positronium atoms, of the order of $\sigma_v = 10^5$ m/s, or in temperature $T \simeq 1300$ K [55].

2.3.2 Antiproton manipulation

The confinement of the antiprotons is ensured by a set of Penning-Malmberg traps placed in supra-conducting solenoids. In such traps, an axial magnetic field ensures the confinement of the particles radially while the longitudinal motion is restricted by applying a potential well on a set of ring-shaped electrodes. A view of the AEGIS traps is shown in figure 2.6. In the AEGIS setup, the magnetic field surrounding the traps is of 5 T and 1 T.

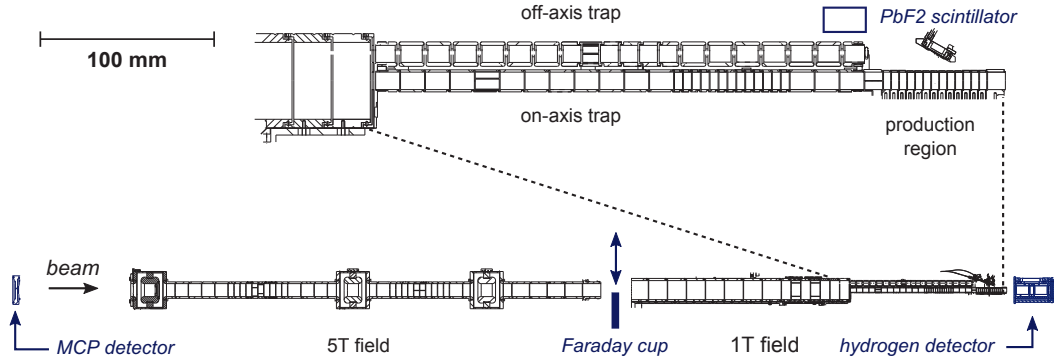


Figure 2.6: Schematic view of the AEGIS traps as well as some of the detectors (blue). The antiprotons exiting the AD and passing through a thin degrader from the left side are caught and cooled in a trap placed in a 5 T magnetic field (left). A microchannel plate (MCP) as well as a movable Faraday cup are the main diagnostics for this region of the apparatus. The antiprotons are then sent toward the 1 T trap, divided into two parts: the off-axis trap, where the positrons are transmitted toward the positronium converter, and the on-axis trap where the antihydrogen production occurs. A PbF_2 scintillator placed nearby the positronium converter is used to detect the formation of positronium. The hydrogen detector (see section 2.3.4) ensures a feedback on the antiproton manipulations in the 1 T region.

Several steps are needed to prepare and transfer the antiprotons to the region where antihydrogen atoms are produced. The procedure adopted in AEGIS is the following:

1. About 10^8 electrons are loaded into a ~ 120 V deep potential well in the 5 T trap. Within a few milliseconds, they then cool down to the cryogenic temperature [57];
2. The AD supplies a bunch of approximately $3 \cdot 10^7$ antiprotons at 5.3 MeV. After passing through a $150 \mu\text{m}$ aluminum foil and a $55 \mu\text{m}$ thick silicon beam counter, the fraction having an energy smaller than 9 keV is caught in the 5 T trap ($\sim 1\%$ of the AD beam [56]);
3. By coulomb collisions, antiprotons transfer their energy to the cold electrons which in turns radiate within a few ms (sympathetic cooling). The time needed for the antiproton temperature to stabilize is typically of the order of one minute;
4. Antiprotons are compressed by applying an oscillating potential on an electrode segmented azimuthally ("Rotating Wall" technique) and are finally sent from the 5 T toward the trap (10 mm in diameter) where the production is planned to occur, located in the 1 T region. This step reaches 90 % of efficiency such that around $3 \cdot 10^5$ antiprotons are stored into the production trap for each shot of the AD.

One should notice that, with this method, the temperature of the antiprotons is limited to the cryogenic temperature, typically around a few Kelvins. In order to cool the antiprotons to sub-Kelvin temperatures, other methods are envisioned such as sympathetic cooling with osmium [58], lanthanum [59] or C_2^- ions [60].

2.3.3 Charge-exchange reaction

Proposed initially by Deutch et al. [61], the formation of antihydrogen by charge-exchange reaction was demonstrated in 2004 by the ATRAP collaboration [62]. Four years later, Charlton pointed out the possibility that such reactions could markedly enhance antihydrogen production [63]. From a classical point of view, he indeed argued that the cross-section should increase as the area of the positronium atom. Since the positronium radius scales with the square of its main quantum number n_{Ps} , a n_{Ps}^4 scaling should hence be expected.

Is there an optimal energy for the antiprotons to maximize the number of antihydrogen atoms produced? Indeed, the Massey criterion states that the capture probability is highest when the speed of the antiproton matches the orbital speed of the positron in the positronium atom. This behavior seems to be confirmed experimentally when looking at proton impacts on positronium in the ground state as observed by reference [64]. In spite of the very few points available, the hydrogen production cross-section as a function of the proton energy seems to present a maximum around a proton energy of 3 to 4 keV. But despite the high flux achievable with antiprotons in the keV range, other constraints have to be taken into account in the case of AEGIS, since the antihydrogen temperature has to be kept as low as possible. To this extent, a key feature of the charge-exchange reaction is that the antihydrogen temperature is directly driven by the one of the antiprotons. The antihydrogen temperature expected by reacting 100 mK antiprotons with Rydberg positronium ($n = 35$), is for instance of the order of 120 mK [21].

The production of antihydrogen by charge exchange offers hence several advantages: high fluxes of antihydrogen are in principle achievable, it presents a narrow and well-defined n -state distribution, and the antihydrogen temperature is driven by the antiproton energy. To monitor the antiproton manipulations and the state distribution of antihydrogen, a diagnostic is needed at the exit of the production trap. We present in the next section the hydrogen detector, an imaging detector set up during the PhD.

2.3.4 The hydrogen detector

Located in the 1 T magnet, the hydrogen detector enables one to visualize the antihydrogen production process by imaging the antiproton plasma and, in the near future, detecting the Rydberg atoms. A view of the detector is shown in figure 2.7.

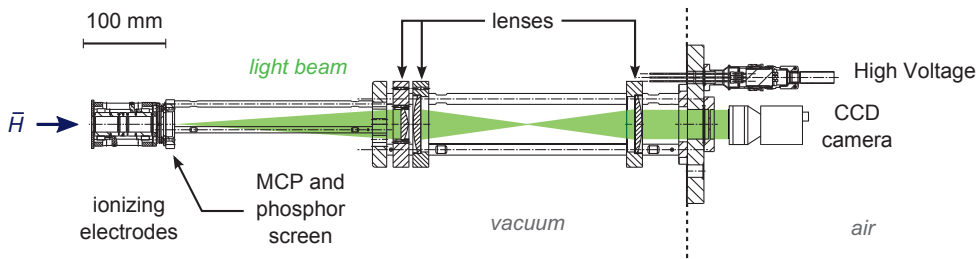


Figure 2.7: Schematic view of the hydrogen detector, located in the 1 T region. The detector is composed of three ring shaped electrodes creating a high electric field gradient to ionize antihydrogen atoms, a two-stage micro-channel plate connected to a fast phosphor screen and a system of three optical lenses focusing the light exiting the phosphor screen on a CCD camera.

It consists of three ring shaped electrodes creating a high electric field gradient to ionize antihydrogen atoms. The antiproton hence separated from the positron is sent onto a two-stage

micro-channel plate (MCP) stacked to a fast phosphor screen. Three lenses focus then the light exiting the phosphor screen on a CCD camera placed outside the vessel. The whole detector is placed in the 1 T magnet, 10 mm downstream of the anti-hydrogen production zone. We detail in the following the different parts and the performance of this detector.

Ionizing electrodes

The three electrodes are 30 mm, 10 mm and 30 mm long respectively and are spaced by 0.5 mm. By applying a voltage ranging from 0 to 5 kV, the maximal electric field created is therefore of the order of 1 MV/m in the gap between two rings. The field is however widely reduced to a few hundreds of kV/m in the center of the electrodes [71].

The probability for an antihydrogen atom to be ionized when placed in a constant electric field $|\vec{E}|$ and after a time t is given by $P = 1 - e^{-\omega t}$ where $\omega = 1/\tau$ is the ionization rate [70]. For a ground state antihydrogen atom, the ionization rate can be calculated analytically [70]:

$$\omega = \frac{4\omega_A |\vec{E}_A|}{|\vec{E}|} \exp\left(-\frac{2}{3} \frac{|\vec{E}_A|}{|\vec{E}|}\right), \quad (2.6)$$

with

$$\omega_A = \frac{me^4}{(4\pi\epsilon_0)^2 h^3}, \text{ and } |\vec{E}_A| = \frac{m^2 e^5}{(4\pi\epsilon_0)^3 h^4}. \quad (2.7)$$

Equation (2.6) leads to a significant ionization rate (better than 10^8 s^{-1}) for an electric field of the order of few 10^{11} V/m , that cannot be reached with the detector. The constraints are however loosen when one considers excited states. Taking into account the field distribution within the electrode, the fraction of antihydrogen ionized and the detection efficiency of the hydrogen detector are given in figure 2.8. For a 5 kV voltage difference between the first two electrodes, all of the atoms excited to $n > 26$ are ionized. The detection efficiency ranges on the other hand from 0 for $n = 22$ to 1 for $n = 46$.

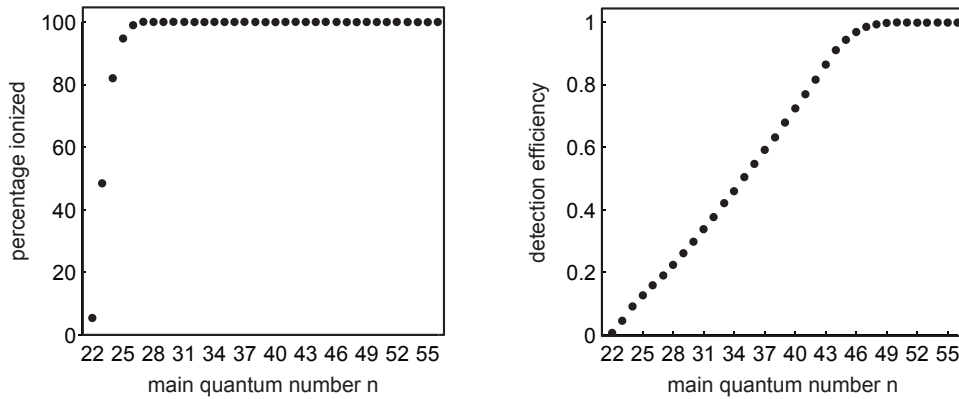


Figure 2.8: (left) The fraction of antihydrogen ionized for several excited states. (right) The detection efficiency taking into account the spatial distribution of the Rydberg atoms in the volume of the electrodes. Both plots are obtained with the first electrode being grounded, while the second and third are set to 5 kV (from [71]).

MCP and phosphor screen

Once ionized, either the antiproton or the positron from the antihydrogen can be sent onto the imaging detector by applying the correct field. The amplification of the signal is ensured by a two-stage MCP (typical gain $\sim 10^6$) stacked to a fast phosphor screen⁵, converting the secondary electrons into photons. The specifications of our model are given in table 2.2. The voltage configuration is such that the voltage on the MCP is kept as low as possible while the phosphor screen is pushed at his maximum conversion efficiency. The risk to damage the MCP are considerably reduced by doing so. Unless one needs to accelerate the antiprotons or positrons toward the detector, the front plane of the MCP is grounded.

MCP		Phosphor screen	
Type	two-stages	Type	P46
Effective area	24 mm	Peak wavelength	530 nm (yellowish green)
Open fraction	60 %	10% afterglow time	0.2 to 0.4 μ s
Power supply	0 to 2 kV	Power supply	~ 4 kV

Table 2.2: MCP and phosphor screen specifications for the model F2223-21P from Hamamatsu [72]. The phosphor screen is chosen for his fast response time, allowing time-of-flight measurement.

As the detector is designed to perform time-of-flight measurements, one may wonder what is its response time. The MCP can in first approach be modeled as an RC circuit. If the MCP resistance reach a few $G\Omega$ at 4 K, the capacitance can be estimated by the relation [73]:

$$C = \epsilon_0 (\epsilon_r (1 - f_{open}) + f_{open}) \frac{\pi d_{act}^2}{4L} + \epsilon_0 \epsilon_r \frac{\pi (d_{MCP}^2 - d_{act}^2)}{4L}, \quad (2.8)$$

where L is the thickness, f_{open} the open fraction of the channels and d_{act} the active area of the MCP. For the model considered, it corresponds to $C = 40$ pF. The response time, of the order of several ms at cryogenics temperatures, is hence inappropriate for time-of-flight measurements. This limitation is overcome by the addition of heating resistors around the MCP.

CCD camera

The CCD camera used initially was model DCU223M from Thorlabs [74]. Some of the relevant specifications of this camera along with its sensor are given in table 2.3. The camera is chosen for its maximal sensitivity around 530 nm, which correspond to the peak wavelength of the phosphor screen.

CCD Camera		Optical Sensor	
model	DCU223M	model	SONY ICX204AL
bit depth	8, monochrome	Full Well Capacity	12 000 e^-
resolution	1024 \times 768 pixels	dark current	3 e^- /pixel
exposure time (trigger)	0.03 ms to 10 min	pixel size	4.65 \times 4.65 μ m ²
frame rate (freerun)	15 to 30 fps	Quantum Efficiency	37% at 532 nm

Table 2.3: Specifications of the CCD camera and its optical sensor (from [74], [75]).

⁵model F2223-21P from Hamamatsu [72]

The number of photons to saturate each pixel is calculated as $N = FWC/QE$, in which FWC (Full Well Capacity) is the amount of charge an individual pixel can hold before saturating, and QE the quantum efficiency at 532 nm. It corresponds roughly to 32400 photons per pixel. Independently from the hot pixels, all of the images presents a certain level of noise whose the sources can be numerous (thermal noise, dark current or readout noise). The noise intensity observed on the image is of the order of $(5/256) * FWC = 234$ photo-electrons.

Sensitivity to magnetic field

To ensure the proper operation of the detector in the high magnetic field where it is placed, the MCP channels are drilled with an angle ranging from 5 to 15 degrees. By stacking the two MCP in reverse way (the channels are in chevron configuration), the relative intensity is enhanced for a magnetic field around 1 T [72].

Efficiency

The hydrogen detector has been designed to observe the impact of a single antihydrogen atom. Starting from a unique antiproton impinging on the MCP, the detection efficiencies of the different parts of the detector are given in table 2.4. Since the detector has not been used with antihydrogen yet, the efficiency of the ionization electrodes (detailed in section 2.3.4) is not taken into account here.

Module	Type	Efficiency
MCP	Gain (at 1.5 kV)	10^6
Phosphor screen	Conversion efficiency	30 photons/ e^-
Lenses	Light collection	0.267 %
CCD camera	Light collection	14 %
Optical sensor	Quantum efficiency	37 %
Total Gain		4196 e^- / incident \bar{p}

Table 2.4: Detection efficiencies of the different modules of the hydrogen detector. The conversion efficiency of the phosphor screen is taken from reference [76]. The light collection efficiency of the CCD camera is the ratio between the surfaces of the objective and of the last lens.

The photons exiting the phosphor screen are collected by three lenses placed such that the light beam is parallel when reaching the camera. The first lens (45 mm in diameter) of the system is placed at 307 mm from the phosphor screen plane. Based on solid angle considerations, and assuming a 100 % transport efficiency between the first and the third lens, the fraction of photons collected by the optical system is hence of the order of 0.27 %.

The impact of a single antiproton should lead therefore to 4196 electrons collected. With a noise level of 234 electrons calculated in the previous section, it corresponds to a signal-to-noise ratio around 18. In the current status of the experiment, in which the aim is more the understanding of the plasma manipulations performed inside the traps, the typical number of antiprotons is typically of the order of 10^5 such that the MCP voltage set rarely overcomes 1 kV to avoid the camera to saturate.

Single antiproton and plasma imaging

An image of few antiprotons released onto the hydrogen detector is shown in figure 2.9. As one can see on the image, the impacts of single antiprotons can be clearly identified.

The hydrogen detector enables one to have a feedback on the manipulation of the antiprotons in the AEGIS traps (see section 2.3.2). Moreover, it offers the possibility to monitor the loading of electrons during the cooling of antiprotons (see section 2.3.2), or the beam of positrons. Images of electrons and positron on the detector are shown in figure 2.10.

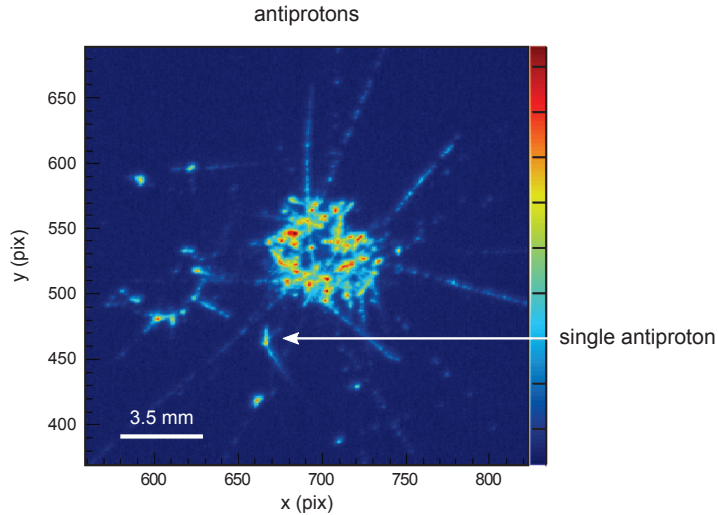


Figure 2.9: Few antiprotons released from the AEGIS trap onto the hydrogen detector. To visualize single antiproton annihilations, the MCP gain is set to high value (1500 V on that image). A different camera (ORCA-R2 digital CCD camera, model C10600-10B from Hamamatsu) was used to take this image.

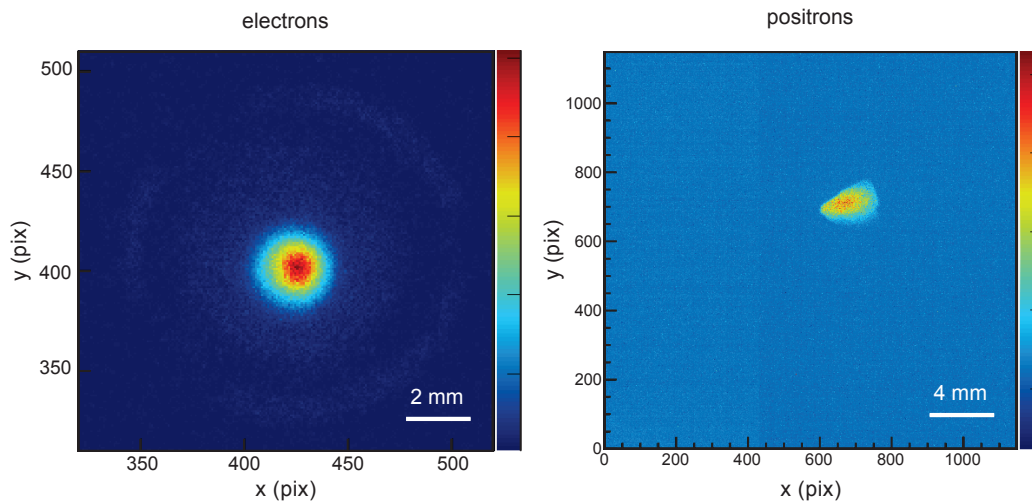


Figure 2.10: Image of electrons (left) and positrons (right) released onto the hydrogen detector. The images were acquired with the ORCA-Flash 4.0 V2 camera, model C11440-22CU from Hamamatsu for the positrons and the DCU223M camera from Thorlabs for the electrons.

2.3.5 Measuring $g(\bar{H})$

The device foreseen to measure $g(\bar{H})$ in the AEGIS experiment is a moiré deflectometer. In its simplest implementation, the moiré deflectometer consists of two transmission gratings separated by a distance L and a position sensitive detector. The periodicity, or pitch, of the grating is d . As shown in figure 2.11, under the effect of gravitation, massive particles experience an acceleration a in the vertical direction leading to a parabolic trajectory while undeflected particles such as photons conserve straight trajectories throughout the whole apparatus. The shift Δy between the two fringes at the level of the detector is then given by:

$$\Delta y = v_y \tau + \frac{1}{2} a \tau^2, \quad (2.9)$$

where v_y denotes the transverse velocity of the particle when reaching the second slit and $\tau = L/v_z$ is the time-of-flight between the two gratings. The vertical velocity v_y at the second slit results from the acceleration beginning on the top of the parabola, thus $v_y = a \tau / 2$. One can therefore simplify equation (2.9):

$$\begin{aligned} \Delta y &= \frac{1}{2} a \tau^2 + \frac{1}{2} a \tau^2, \\ \Delta y &= a \tau^2. \end{aligned} \quad (2.10)$$

For an apparatus length of 1 meter and assuming a Maxwellian distribution of the particles peaked around a few Kelvins (corresponding to a mean velocity of 400 m/s), it leads to a typical spatial shift of 50 μm for a gravitational acceleration $a = 9.81 \text{ m.s}^{-2}$.

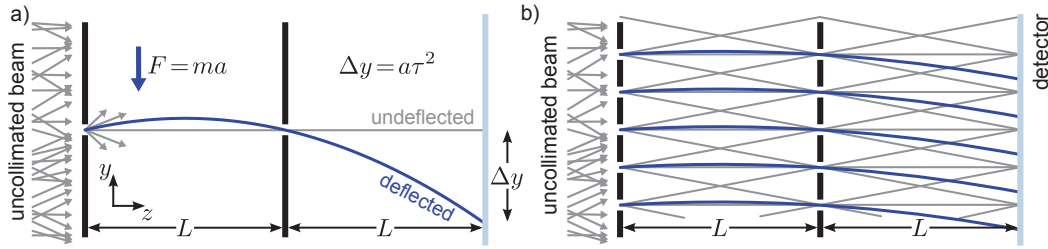


Figure 2.11: The value of the gravitational acceleration for antimatter is proposed to be measured using a moiré deflectometer, consisting of two transmission gratings separated by a distance L and having a pitch d . Under the effect of gravitation, massive particles experience an acceleration a in the vertical direction leading to a parabolic trajectory while undeflected particles such as photons conserve straight trajectories throughout the whole apparatus. The shift Δy between the two fringes at the level of the detector is then given by $\Delta y = a \tau^2$, where $\tau = L/v_z$ is the time of flight between two gratings (image from reference [81]).

We stress that the gravitational interaction has been already tested with high precision on atomic beam. In 2001, a relative accuracy to the Earth gravitational acceleration g of 10^{-10} has been reported with an atomic interferometer using a beam of cold cesium atoms [79]. Instead, the moiré deflectometer was used in 1996 by M. K. Oberthaler to measure g with a metastable Ar atom beam with a relative accuracy of 2.10^{-4} [80]. But compared to atomic interferometers, the strength of the apparatus is to be nondispersive, such that atoms with a broad energy distribution and without collimation can be used [80].

The sensitivity of the moiré deflectometer depends on the number of antihydrogen detected and on several geometrical parameters. Reference [81] gives a detailed expression of the minimal acceleration that can be measured with the device:

$$a_{min} = \underbrace{\frac{d}{2\pi\nu\eta r}}_{\text{gratings}} \cdot \underbrace{\frac{L_{1st} + 2L}{L^2}}_{\text{geometry}} \cdot \underbrace{\frac{k_B T}{m_{\bar{H}} \sqrt{N_{prod}}}}_{\text{source}}, \quad (2.11)$$

where d and r are respectively the pitch and the radius of the gratings, the first grating being placed at a distance L_{1st} from the production trap. k_B is the Boltzmann constant, ν is the fringes visibility, a dimensionless number which will be introduced in next chapter, and N_{prod} is the number of antihydrogen produced at a temperature T . Such a formula can be seen as a guideline to design the deflectometer. To measure g with high accuracy, it is indeed important to have a low temperature of the antihydrogen atoms, to detect a large number of \bar{H} , and to place the deflectometer as close as possible of the production region. Based on the flux of \bar{H} expected for the charge-exchange reaction, reference [82] proposes different possible designs to achieve a 30 % resolution on g with minimal integration time.

A first step for the AEGIS experiment would be to evaluate the sign of $g(\bar{H})$. Under certain assumptions (Maxwellian distribution of the \bar{H} temperature, phase kept below π) the rotation of the deflectometer by 30 degrees along the beam axis enables one to retrieve the sign of g . Measuring in a second time g at a few percents raises several challenges. The remaining open questions are:

- producing antihydrogen with sufficient flux. As seen in equation (2.11), the number of antihydrogen formed is the ultimate limit once the gratings and the deflectometer geometry are chosen;
- precisely knowing the antihydrogen state distribution at the level of the deflectometer. The \bar{H} should not decay during their travel through the gratings, otherwise the velocity recoil following the photon emission may mask the effect of gravity [21];
- controlling the magnetic gradient within the deflectometer. Indeed, any magnetic gradient along z in the region of the deflectometer would cause a vertical force $F_z = -\mu_z \cdot dB_z/dz$, with μ_z the magnetic moment. A magnetic gradient of 0.18 G/cm would cause the same deflection than an acceleration of g for ground-state antihydrogen [21]. The effect gets even worst if the \bar{H} are in an excited state.

2.4 Summary

The imbalance of matter and antimatter in the near universe, as well as the lack of knowledge concerning its composition, motivates the search for a different gravitational interaction in the antimatter sector. For this purpose, the antiproton decelerator (AD) is a precious facility. The AD currently provides a beam of 5.3 MeV antiprotons every 110 s but, in the coming years, an additional stage of deceleration (ELENA) should be able to reduce the antiprotons energy to 100 keV. In the past, several experiments put indirect limits on the value of the gravitational acceleration for antimatter. But it is only with the advent of antihydrogen physics in the mid 1990's that innovative realistic setups have been proposed to measure directly the force acting on antimatter particles. Among the different collaborations involved in the understanding of the gravitational behavior of antimatter, AEGIS aims at observing the free-fall of antihydrogen atoms. In dedicated traps, antihydrogen atoms are formed by charge-exchange between trapped antiprotons and positronium. Once formed, the gravitational acceleration on the antihydrogen atoms will be measured by the mean of a moiré deflectometer, a device consisting in its simplest configuration of two transmission gratings and a position sensitive detector.

3 | Moiré Deflectometry and Talbot-Lau Interferometry

We detail now the working principle of the moiré deflectometer, envisioned for the gravity measurement in AEGIS. We have seen in the previous chapter that it consists of two gratings and a position sensitive detector. When the particles pass through the gratings, a fringe pattern is formed on the detector. As the beam is deflected by gravity, measuring the vertical shift of the fringe pattern enables one to retrieve the value of the gravitational (vertical) acceleration g . We present in this chapter the theoretical concepts involved in moiré deflectometry. We give first an analytical expression of the fringe pattern formed by the two gratings. It will then be shown that a third grating can be placed behind the two gratings to enlarge the fringe pattern. Another application of the moiré deflectometer (beside measuring gravitational interaction) is then introduced. In the same way gravitation is used to bend the trajectory of massive bodies, a Lorentz force can induce a deflection on a beam of charged particles. With different ions, the deflectometer is moreover able to distinguish a deflection due to an electric field from a deflection due to a magnetic field. The moiré “fieldmeter”, is able to measure fields as low as $9 \text{ mV}\cdot\text{m}^{-1}$ and $140 \mu\text{G}$ for one second of acquisition time. The concepts presented here have been recently published in an article [86].

When the pitch of the gratings becomes smaller than a certain scale, the diffraction of the ions have to be taken into account. The fieldmeter, sensitive to the wave behavior of the ions, is then turned into a Talbot-Lau interferometer. Although particles trajectories are no longer defined in this regime, the probability to find the particles at a certain location exhibits a typical geometric pattern. As a results, the contrast of the fringes are no longer fixed but evolve with the wavelength of the ions. Looking for modulations of the fringes contrast is therefore an evidence of the wave behavior of the ions. Although interference is a phenomenon which has been extensively investigated with light, atoms and even large molecules, it has never been shown for ions. Achieving the Talbot-Lau interferometry of protons would be therefore of high interest. We summarize in the last part a few quantities one has to keep in mind in order to perform such an experiment.

3.1 Moiré concepts

As seen in chapter 2, two gratings are sufficient to measure the magnitude of a force acting on a beam of particles. After having given the expression of the fringe pattern formed by two gratings, we will see that adding a third grating allows one to benefit from the moiré effect to enlarge that pattern.

3.1.1 Fringe pattern of two gratings

As shown on figure 3.1, a multitude of trajectories are allowed to pass through two gratings. If the distance between the second grating and the detector is furthermore imposed to be equal to the distance between the two gratings, the shape of the fringes seen on the detector is entirely defined by the gratings pitch d and their open fraction η . It is indeed the convolution of two rectangle functions, one with periodicity d corresponding to the first grating, and one with periodicity $2d$ corresponding to the projection of the first grating onto the plane of the second grating. Using the product of the Fourier transforms of two rectangles, the analytical expression of the pattern is [83]:

$$I(y) = \sum_{n=-\infty}^{+\infty} c_n \exp\left(\frac{2i\pi n}{d}y\right), \quad (3.1)$$

where the c_n coefficients¹ are given by:

$$c_n = 2\eta^2 \text{sinc}^2(\pi\eta n) \cos(\pi\eta n) \quad \forall n \in \mathbb{N}. \quad (3.2)$$

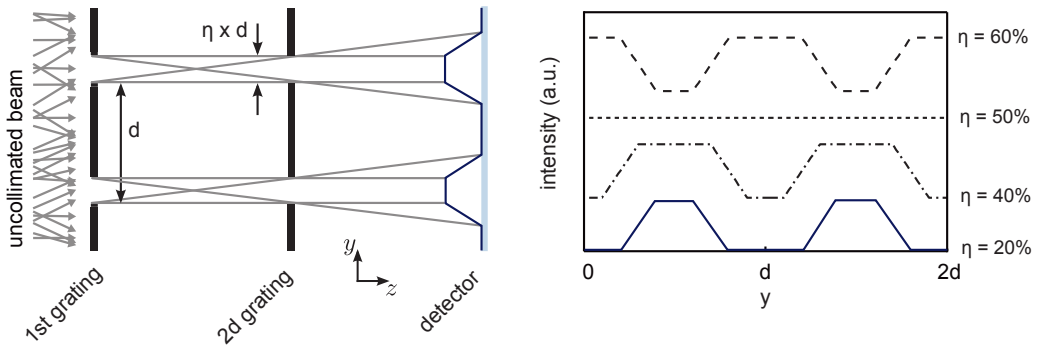


Figure 3.1: (left) Two gratings constrain the particle trajectories of an uncollimated beam. The pattern observed on the detector is the convolution of two square functions defined entirely by the gratings pitch d and their open fraction η . (right) The pattern observed on the detector plane for different open fractions η . No pattern is visible when $\eta = 50\%$ since the shadows of two neighboring slits overlap completely.

One can see in figure 3.1 that the periodicity of the pattern formed on the detector plane is equal to the gratings periodicity. In the AEGIS experiment, the periodicity of the gratings could be in a first time of $40 \mu\text{m}$, of the order of the gravitational shift expected (see chapter 2). A suitable detector should therefore be able to resolve features of several microns to observe such a pattern. The spatial resolution of a few detectors, commonly used in particle physics, are listed in table 3.1. Except the nuclear emulsion plates, discussed in chapter 6, one can notice that the spatial resolution of most of standard detectors exceeds $10 \mu\text{m}$.

¹For the whole thesis, the cardinal sine function is defined by $\text{sinc}(x) = \sin(x)/x$.

detector type	spatial resolution (r.m.s)
Resistive plate chamber	$\lesssim 10$ mm
Bubble chamber	10 to 150 μm
Micro-pattern gas detectors	30 to 40 μm
Microchannel plates	10 to 20 μm
Silicon pixel	$\lesssim 10$ μm
Nuclear emulsions	1 μm

Table 3.1: The intrinsic spatial resolution of a few standard particle detectors. Except the emulsions, most detectors do not have a resolution of few microns. (table from reference [85]). The resolution of microchannel plates is measured in next chapter.

3.1.2 Magnification with a third grating

The moiré effect is a general phenomenon appearing when two objects presenting a certain spatial periodicity are superimposed. The beating of the two structures causes the formation of a pattern whose characteristic scale may be larger than the object periodicity. A common manifestation can for example be observed on a television screen when a person wearing a striped shirt is filmed: the formation of waves in the image is the consequence of the beating of the stripes with the scanning line of the television set. In the case of gratings, a moiré effect is also visible if one imposes a slight tilt or a slight periodicity difference between two gratings. This is used to reveal macroscopic fringes orthogonal to the slit orientation, as shown in figure 3.2. For a small angle between the gratings, the macroscopic fringe periodicity D is directly proportional to the gratings pitch and scales with the inverse of the angle α such that $D = d/\alpha$. In the moiré deflectometer, a third grating tilted by a small angle, is hence placed at the position of the position-sensitive detector. The shift Δy of the pattern when a force is acting is magnified accordingly:

$$\Delta x_{\text{moiré}} = \frac{\Delta y}{\alpha}. \quad (3.3)$$

As one can choose the angle α arbitrarily small, the spatial resolution of the detector is no longer a constraint. The counterpart is the consequent loss of intensity observed on the detector as the beam undergoes an additional grating.

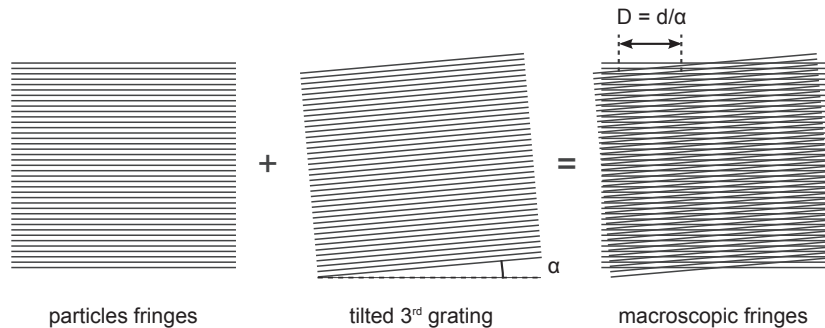


Figure 3.2: A third grating placed behind the fringes but tilted by a small angle enables one to take advantage of the moiré effect to reveal macroscopic pattern, orthogonal to the slits orientation.

The resulting moiré pattern is the convolution of the pattern created by two gratings (see equation (3.1)) with a rectangle function corresponding to the third grating. As the fringes are moreover rotated by 90 degrees, the analytical expression of the intensity along x is [83]:

$$I(x) = \frac{a_0}{2} + \sum_{n=1}^{+\infty} a_n \cos\left(\frac{2\pi n}{D}x\right), \quad (3.4)$$

where the a_n coefficients are given by:

$$a_n = 4\eta^3 \text{sinc}^3(\pi\eta n) \cos(\pi\eta n), \quad \forall n \in \mathbb{N}. \quad (3.5)$$

The moiré fringes observed upstream of the third grating and for different open fraction η are displayed on figure 3.3 (left). Only the first Fourier coefficients (until $n \leq 5$) are taken into account for the computation of the pattern. Reference [83] shows indeed that the other coefficients are negligible. To quantify the contrast of the fringes, we introduce the visibility ν , a dimensionless quantity comprised between 0 and 1. It is defined by the relative difference between the maximal and minimal intensity recorded on the detector:

$$\nu = \frac{I_{\max} - I_{\min}}{I_{\max} + I_{\min}}. \quad (3.6)$$

The visibility of the macroscopic pattern as a function of the gratings open fraction is given in figure 3.3 (right). It is equal to 1 for open fraction until 25 % and then drops rapidly to zero for $\eta = 50$ %.

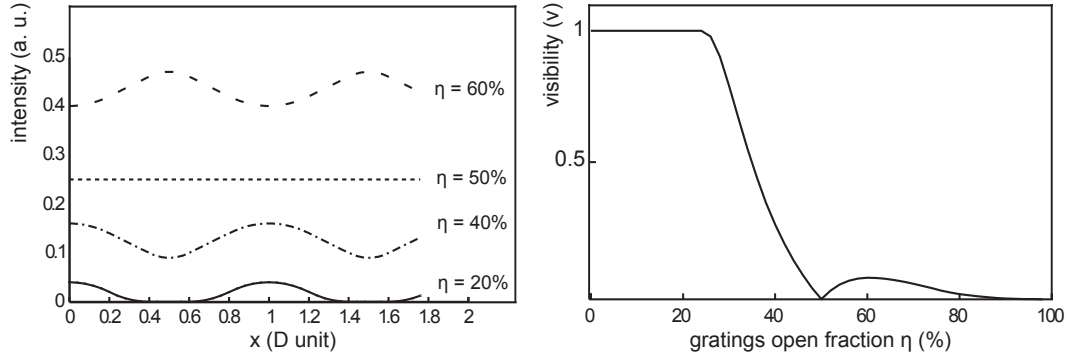


Figure 3.3: (left) The moiré fringes observed upstream of the third grating for different open fraction η . (right) The fringes visibility as a function of the gratings open fraction. The visibility is close to 1, for open fractions below 25 % and drops rapidly to 0 for $\eta = 50$ %. The transmission, evolving as η^3 is on the other hand higher for large open fractions.

3.2 Probing electric and magnetic field

In the same way the moiré deflectometer is able to measure the shift induced by gravity on massive atoms, it can be used to measure the deflection induced by a Lorentz force on charged particles. In order to prepare the ground for the AEGIS experiment, the idea to test the moiré deflectometer with a low-energy ion source was suggested. Compared to a beam of neutral particles, ions offer indeed the possibility to emulate the effect of gravity and tune its magnitude, using for instance magnetic fields. Moreover, with two different ion species

having distinct q/m ratios, the effects of magnetic and electric fields can be decoupled. The sensitivity of such a fieldmeter depends on geometric factor such as the gratings pitch and sizes, but the measurement is ultimately limited by the number of ions detected. We estimate with finite elements calculation a multiplying factor accounting for the deformation of the field lines when the apparatus is placed in an homogeneous electric field. Finally, the maximal frequency at which the device can be operated is evaluated. The concepts presented here have been recently published in an article [86].

3.2.1 Deflection by a magnetic field

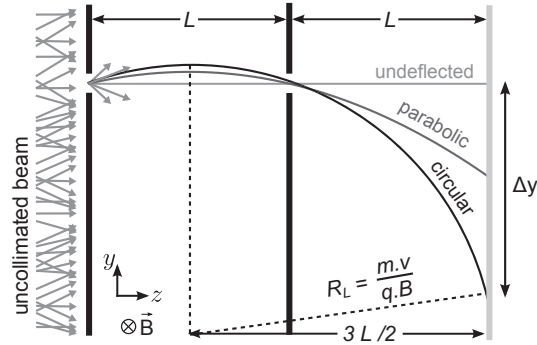


Figure 3.4: A particle adopts different trajectories depending on the force considered. If an electric (respectively gravitational) field causes the parabolic deflection of a particle with charge q (resp. mass m), a magnetic field, oriented in the same direction than the gratings slits, induces a circular motion with radius $R_L = mv_z/qB_x$. The two situations lead however to similar expressions for the vertical shift if $R_L \gg L$ (not the case on the illustration).

A particle with mass m and velocity \vec{v} placed in a gravitational field \vec{g} adopts a parabolic trajectory. We recall the expression of the shift Δy measured at the position of the detector in the more general case of an acceleration a (see previous chapter):

$$\Delta y = a\tau^2. \quad (3.7)$$

One can easily show that the expression remains the same for an electric field \vec{E} since the force experienced, $\vec{F} = q\vec{E}$, is the analog of the gravitational force $\vec{F} = m\vec{g}$. However, is this expression still verified for a magnetic field? Indeed, in presence of a magnetic field \vec{B} , the trajectory adopted in the (Oyz) plane is no longer parabolic but circular, as seen in figure 3.4. Its radius of curvature is given by $R_L = mv_z/qB_x$, where R_L is the Larmor radius and v_z the particle velocity. Reference [87] derives the expression of the consequent vertical shift Δy as a function of the Larmor radius:

$$\Delta y = R_L \left[\left[1 - \left(\frac{L}{2R_L} \right)^2 \right]^{1/2} - \left[1 - \left(\frac{3L}{2R_L} \right)^2 \right]^{1/2} \right]. \quad (3.8)$$

The Larmor radii of protons at various energies are listed at the end of this section (table 3.3). For protons with keV energy, the distance L between two gratings (at most 171 mm, see next chapter) is always small compared to $R_L = 46$ m. A Taylor expansion in L/R_L of expression (3.8) is hence valid:

$$\Delta y \simeq R_L \left[1 - \frac{1}{2} \left(\frac{L}{2R_L} \right)^2 - 1 + \frac{9}{2} \left(\frac{L}{2R_L} \right)^2 \right], \quad (3.9)$$

which can be rewritten as:

$$\Delta y \simeq \underbrace{\frac{qB_x v_z}{m}}_a \underbrace{\left(\frac{L}{v_z} \right)^2}_{\tau^2}. \quad (3.10)$$

The shift can be seen as the product of an acceleration $a = qB_x v_z/m$ and the square of the time-of-flight $\tau = L/v_z$. We will consider therefore that equation (3.7) holds also for a magnetic deflection.

3.2.2 Decoupling electric and magnetic components

When affected by both an electric and a magnetic field, charged particles experience Lorentz forces, translating into an acceleration $\vec{a} = \frac{q}{m}(\vec{E} + \vec{v} \wedge \vec{B})$. Following the axis convention of figure 3.4, and for small radial velocities², the field components leading to a shift along the y axis are trivially the components along y for \vec{E} and along x for \vec{B} . The vertical deflection reads:

$$\begin{aligned} \Delta y &= a\tau^2 \\ \Delta y &= \frac{q}{m}(\vec{E} + \vec{v} \wedge \vec{B}) \cdot \vec{u}_y \cdot \left(\frac{L}{v_z} \right)^2 \\ \Delta y &= \frac{q}{m}(E_y + B_x v_z - \underbrace{B_z v_x}_{\text{neglected}}) \cdot \left(\frac{L}{v_z} \right)^2 \\ \Delta y &= \frac{q}{mv_z^2} L^2 E_y + \frac{q}{mv_z} L^2 B_x. \end{aligned} \quad (3.11)$$

Introducing V_{acc} the acceleration voltage of the ions and invoking the conservation of energy $qV_{\text{acc}} = \frac{1}{2}mv_z^2$, the shift due to the Lorentz force reads:

$$\Delta y = \frac{L^2}{2V_{\text{acc}}} E_y + \sqrt{\frac{q}{2mV_{\text{acc}}}} L^2 B_x. \quad (3.12)$$

The knowledge of Δy for two different ion species, with distinct charge-to-mass ratios, leads therefore to a system of two linear equations with a unique solution in E_y and B_x . Hence, the contribution of the electric and magnetic fields can be decoupled. It is worth noticing that the electric and magnetic components can be equivalently distinguished with only one type of particle, such as electrons, but using three different acceleration voltages.

3.2.3 Resolution limit

Since neutral particles do not experience any force when placed in constant electric and magnetic fields, they can be used to create a reference pattern. The determination of the phase shift between the pattern of deflected particles and the pattern of neutral particles is depicted schematically in figure 3.5. In order to quantify the resolution of the fieldmeter within a given

²such that $v_x \cdot B_z$ becomes negligible in comparison with $v_z \cdot B_x$.

measurement time Δt , one has to include the statistics and therefore the flux n of the registered atoms. As shown in the close-up view, any phase shift measured on the detector is limited statistically by the number of particles detected $N = n \cdot \Delta t$.

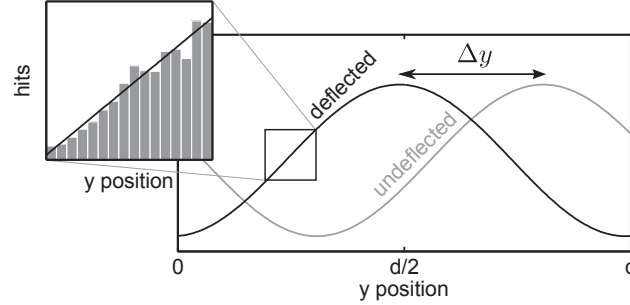


Figure 3.5: The fringe pattern is shifted by Δy due to an uniform acceleration (image from [81]). The number of hits N_i per bin of the detector (close-up view) follows a poissonian distribution, ultimately limited by the shot noise. The uncertainty on each bin is hence $1/\sqrt{N_i}$.

Assuming a Poissonian distribution of the detected events, the relative uncertainty on the phase shift³ is hence given by $1/\nu\sqrt{N}$. Following the derivations of reference [81], the minimal shift that can be measured is:

$$\Delta y_{\min} = \frac{d}{2\pi\nu\sqrt{N}}, \quad (3.13)$$

Assuming that only one component is acting (either $E_y = 0$ or $B_x = 0$), and using equation (3.12), the minimal electric and magnetic fields that can be measured are:

$$\begin{aligned} E_{\min} &= \frac{dV_{\text{acc}}}{\pi\nu L^2\sqrt{N}}, \\ B_{\min} &= \frac{d}{\pi\nu L^2\sqrt{N}} \sqrt{\frac{mV_{\text{acc}}}{2q}}. \end{aligned} \quad (3.14)$$

We consider gratings with pitch $d = 40 \mu\text{m}$, spaced by a distance $L = 171 \text{ mm}$. For a visibility $\nu = 1$, a typical number of $n = 10^4$ ions detected per second at an energy of 2 keV, the minimal fields that can be measured are $E_{\min} = 9 \text{ mV}\cdot\text{m}^{-1}\cdot\text{Hz}^{-1/2}$ and $B_{\min} = 140 \mu\text{G}\cdot\text{Hz}^{-1/2}$. Here the $\text{Hz}^{-1/2}$ unit indicates that the longer one integrates the signal, the better the resolution is. For an acquisition lasting $\Delta t = 1 \text{ s}$, the minimal electric field that can be measured would be $9 \text{ mV}\cdot\text{m}^{-1}$. As the fields scale with d , higher performance can be achieved with gratings having sub-micron pitches. For 100 nm periodicity transmission gratings as the one used in reference [88], the moiré fieldmeter would be able to measure fields as low as $22 \mu\text{V}\cdot\text{m}^{-1}\cdot\text{Hz}^{-1/2}$ and $0.28 \mu\text{G}\cdot\text{Hz}^{-1/2}$ under the same conditions.

3.2.4 Critical fields

For a given number of particles detected, the visibility of the fringes is sensitive to the velocity distribution of the beam, reducing hence the resolution of the fieldmeter. Indeed, in presence of a field, slow particles experience bigger deflections than fast ones. As a consequence, the fringes minima and maxima of the two populations can possibly overlap and smear out the

³the phase shift is defined as $\Delta\Phi = \frac{2\pi}{d}\Delta y$.

pattern. An illustration of the effect is shown in figure 3.6 for a rectangle energy distribution centered on the acceleration voltage V_{acc} . For a more general energy distribution of the beam $f(E)$, the resulting pattern can be expressed by integrating the expression of the pattern intensity I , given in equation (3.4), over the energy:

$$I_{\text{tot}}(y) \propto \int_E f(E) \cdot I\left(\frac{2\pi}{d}(y + \Delta y(E))\right) dE. \quad (3.15)$$

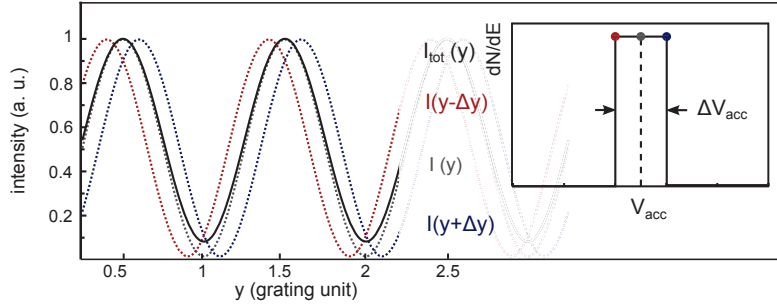


Figure 3.6: In presence of a field, the patterns of fast (blue) and slow (red) particles can possibly overlap. The resulting pattern (black) is the integral of the different patterns (of each populations), normalized to the same intensity. Compared to the original pattern, it presents a lower visibility.

To quantify the consequent visibility reduction, we define the critical fields E_c and B_c as the fields leading to a phase shift of half a period between the two populations. For a given energy spread ΔV_{acc} , the patterns generated by slow and fast particles are separated by $d/2$ when the critical field is acting. For the electric component, we can thus write [86]:

$$\begin{cases} \Delta y = \frac{L^2}{2V_{\text{acc}}} E_c \\ \Delta y + \frac{d}{2} = \frac{L^2}{2(V_{\text{acc}} + \Delta V_{\text{acc}})} E_c. \end{cases} \quad (3.16)$$

Solving this equation system allows one to retrieve the expression of the magnetic and electric critical fields:

$$\begin{aligned} E_c &= \frac{dV_{\text{acc}}^2}{L^2 \Delta V_{\text{acc}}}, \\ B_c &= \frac{d}{L^2} \sqrt{\frac{2m}{q}} \frac{V_{\text{acc}}^{3/2}}{\Delta V_{\text{acc}}}. \end{aligned} \quad (3.17)$$

For a 2 keV proton beam with 1 % energy spread, $d = 40 \mu\text{m}$ and $L = 171 \text{ mm}$, it corresponds to $E_c = 273 \text{ V.m}^{-1}$ and $B_c = 8.9 \text{ G}$. The critical fields give an upper limit on the field magnitudes one can tolerate to visualize the pattern. Higher they are, more robust the moiré deflectometer is.

3.2.5 Detector resolution

The detector spatial resolution σ affects also the fringe visibility due to the uncertainty it causes on each particle impact's coordinates. On figure 3.7 (left) is displayed the convolution of a moiré pattern with a gaussian distribution with standard deviation σ , expressed as a fraction of the fringe periodicity. The different patterns are normalized to the same intensity.

Figure 3.7 (right) shows the resulting visibility as a function of σ . Although the visibility stays above 80 % for a resolution below 10 % of the periodicity, it drops to zero when the resolution is half of the fringes periodicity D . Arbitrarily, one can hence state that the detector resolution should be smaller than 10 % of the fringes periodicity to resolve the pattern with no ambiguity.

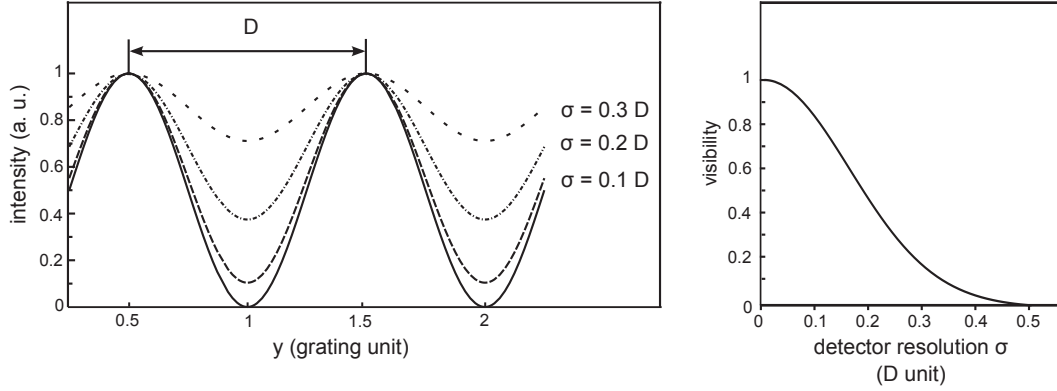


Figure 3.7: (left) A moiré pattern convolved with a gaussian distribution with width σ , accounting for the detector resolution. (right) The consequent visibility as a function of σ . The visibility decreases by approximately 20 % for a detector resolution as high as 10 % of the periodicity.

3.2.6 Field correcting factor

We will see in the next chapter that the gratings have to be electrically conductive and grounded. This constrain may cause an additional error: due to its metallic parts, the moiré fieldmeter alters the field lines when placed inside a uniform electric field. As a consequence, the field magnitude between the gratings gets effectively smaller. The field correcting factor f , defined as the ratio of the field measured and the true field, accounts for this diminution:

$$f = \frac{E_{y,\text{meas}}}{E_{y,\text{true}}}. \quad (3.18)$$

From finite-element method simulation, we estimate this factor for a setup consisting just of three free-standing gratings (assuming for instance that the gratings mechanical supports are made of a material with small permittivity ($\epsilon_R \simeq 1$)). The distribution of the electric field altered by the gratings is shown in figure 3.8. The simulation is done with SIMION 8.0 [89] for an ambient field of $E_{y,\text{true}} = 1 \text{ V.m}^{-1}$. The bottom panel shows the profile of E_y along the axis of the deflectometer (white dashed line). One can notice the presence of zones around the gratings where the electric field drops.

We have seen in section 3.2.2 that the shift due to an uniform electric field when no magnetic field is present is (equation (3.12)):

$$\Delta y = \frac{L^2 E_y}{2V_{\text{acc}}}. \quad (3.19)$$

But, from the distributions plotted in figure 3.8, it is clear that the electric field is no longer uniform within the fieldmeter. Consequently, is the equation (3.19) still valid? To answer this question, we consider the situation depicted in figure 3.9, where a particle (mass m , charge q) travels through a non-uniform electric field $\vec{E}(\vec{r})$. The equation of motion reads:

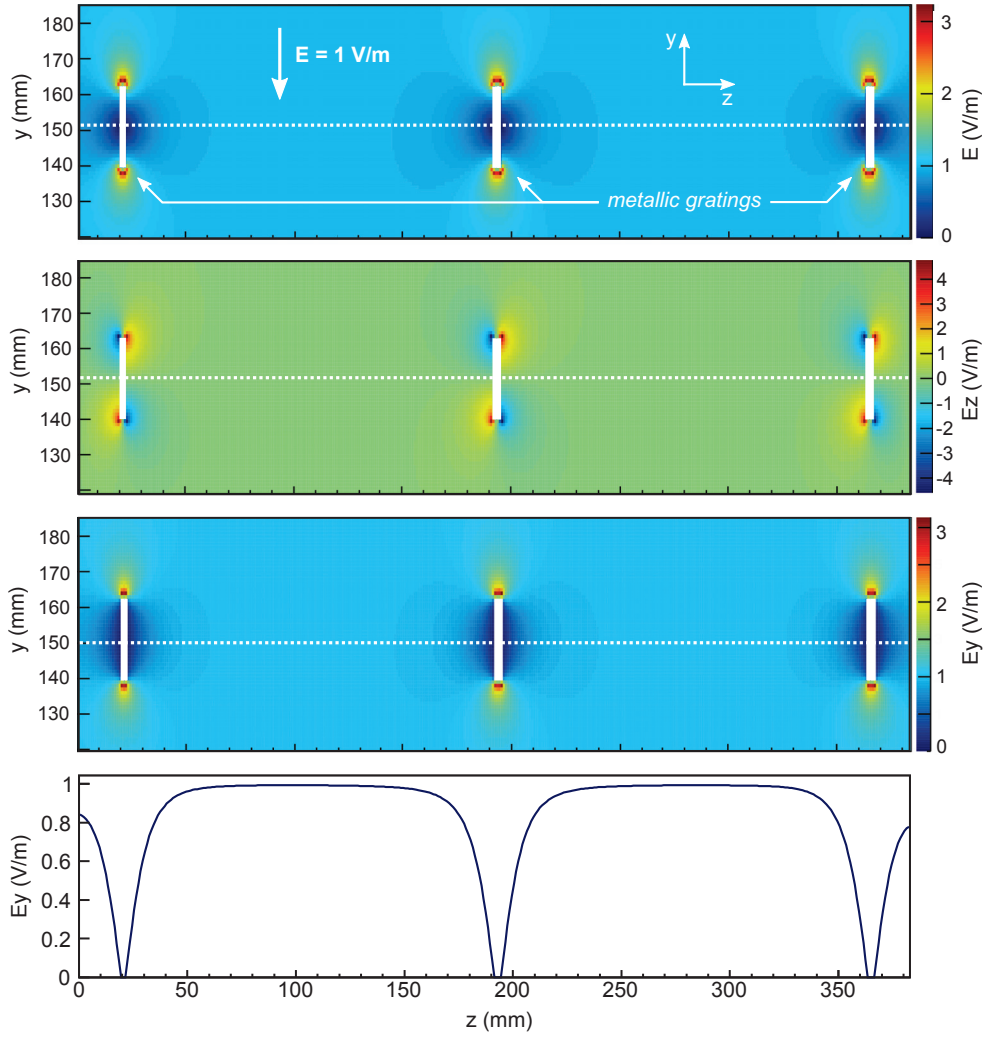


Figure 3.8: (from top to bottom) Electric field distribution simulated with SIMION 8.0 [89] for an ambient field of 1 V/m. The E_z and E_y components are displayed as well as the total electric field $E = \sqrt{E_z^2 + E_y^2}$. One can notice that the field magnitude gets higher around the gratings edges. As shown on the E_z distribution, the particles experience successive decelerations and accelerations through the fieldmeter as the gratings are grounded. (bottom) Profile of the vertical component of the field along the axis of the deflectometer (white dashed line on the upper plots).

$$m \frac{d^2 y}{dt^2} = q E_y(\vec{r}), \quad (3.20)$$

and for the z component:

$$m \frac{d^2 z}{dt^2} = q E_z(\vec{r}). \quad (3.21)$$

As shown on the E_z distribution (figure 3.8, second panel from the top), the ions experience successive decelerations and accelerations along their paths. However, on the axis of the interferometer, we have $E_z(\vec{r}) = 0$ such that the particles velocity is constant and equal to v_z . We can hence write for the y component :

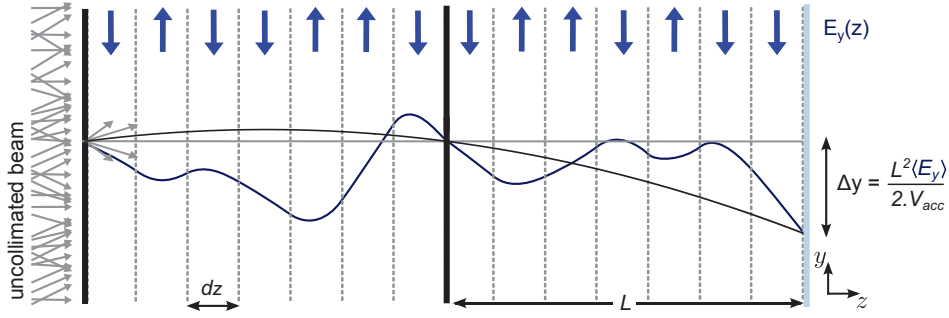


Figure 3.9: (blue) Trajectory of a particle in a non-uniform electric field $E_y(z) \cdot \vec{u}_y$. A particle placed in a uniform field with magnitude $\langle E_y \rangle$ (black) would lead to the same shift Δy .

$$\frac{d^2y}{dz^2} = \frac{qE_y(z)}{mv_z^2}. \quad (3.22)$$

Invoking the conservation of energy $qV_{\text{acc}} = \frac{1}{2}mv_z^2$, we can simplify further:

$$\frac{d^2y}{dz^2} = \frac{E_y(z)}{2V_{\text{acc}}}. \quad (3.23)$$

And if we now integrate this expression between two gratings spaced by L :

$$\frac{dy}{dz} = \frac{1}{2V_{\text{acc}}} \underbrace{\int_0^L E_y(z) dz}_{=L\langle E_y \rangle}. \quad (3.24)$$

We recognize here the average value of the electric field $\langle E_y \rangle$, evaluated between zero and L . A second integration enables one to finally retrieve the expression of the vertical shift Δy for a non-uniform electric field E_y :

$$\Delta y = \frac{L^2 \langle E_y \rangle}{2V_{\text{acc}}}. \quad (3.25)$$

It is remarkable that the shift has therefore the same form than in equation (3.19), the only difference being that the field measured is the average field along the axis of the fieldmeter. From the profile of E_y plotted in figure 3.8 (bottom panel), one can hence evaluate the field correcting factor:

$$f = \frac{\langle E_y \rangle}{E_{y,\text{true}}} = 0.87 \quad (3.26)$$

We will see in the next chapter that most of the parts of the fieldmeter are made of aluminum, whose the relative magnetic permeability is very small [90]: $\mu_r - 1 = 22.10^{-6}$. We assume therefore that the equivalent simulation for the magnetic field is unnecessary.

3.3 Talbot-Lau interferometry with protons

In the moiré deflectometer, the classical description of a particle (by a trajectory) constitutes an important hypothesis. The validity of this approach can be verified, starting from the spatial separation between two orders of diffraction y_n on the detector plane:

$$y_{n+1} - y_n = L \cdot \frac{\lambda_B}{d}, \quad (3.27)$$

where λ_B is the De Broglie wavelength of the particle. An appropriate criterion to assume that diffraction can be neglected is to impose the separation to be much smaller than the gratings periodicity d . It follows the condition: $L \ll d^2/\lambda_B$. We see already here the existence of a characteristic length d^2/λ_B which marks in our setup the limit between the wave regime and the classical regime. The so-called Talbot length is the scale at which the quantum effects are manifested.

After having detailed the interests of interferometry with heavy charged particle such as protons, we introduce the Talbot-Lau interferometer, quantum extension of the moiré deflectometer. As both interference and classical pattern are very similar, it will be shown that the observation of fringes is not a sufficient condition to test unambiguously the quantum behavior of protons. We will see instead that a good approach consists of changing the energy of the protons and looking for modulations of the fringe visibility. The magnitude of the critical fields which might jeopardize the proton interferometry are finally reviewed.

3.3.1 Motivations

It was in the early days of quantum mechanics that Louis de Broglie introduced the idea that any particle should also exhibit wave properties [91]. The so-called particle-wave duality met numerous experimental evidences since, such that it is commonly accepted today that any object presents alternatively the two features depending on the scale of observation considered. Motivated by the work of Planck and Einstein, De Broglie introduced the quantity: $\lambda_B = h/p$, where h is the Planck constant, and p the momentum of the particle. This ratio, homogeneous to a length and better known as the De Broglie wavelength, marks the transition between the two descriptions.

A few years after its formulation by De Broglie in 1924, the particle-wave duality was observed for the first time with atoms and dimers [92], soon followed by the discovery of neutron diffraction in 1936 [93]. In 1999, M. Arndt et al. opened the road to larger objects by interfering successfully fullerenes, voluminous molecules made of 60 carbon atoms arranged in a soccer ball shape [94]. Today, the most massive and complex objects in which wave behavior has been observed are fluorinated porphyrins molecules, having a mass exceeding 10,000 atomic mass unit [95]. What about charged particles? Although the wave properties of electrons were observed already in 1927 [96, 97], no experiments so far have shown that the particle-wave duality holds also for heavier particles. The realization of a bi-prism interferometer with helium ions was indeed attempted by F. Hasselbach [98] but the combination of both a high spatial coherence and a high brightness for the source, features easily addressed in the case of electrons, seemed to be more challenging for ions. Alternatively, we introduce here a remarkable tool to observe the wave behavior of protons, which bypasses the requirements on the source spatial coherence.

3.3.2 Talbot-Lau interferometer

Talbot Effect

Named after H. F. Talbot who first observed its manifestation with light in 1836 [101], the Talbot effect is a near-field diffraction phenomenon appearing when a plane wave illuminates a grating. In that case, the probability to find the particles at a certain place exhibits a typical

pattern, pictured in figure 3.10(a), and known as the Talbot carpet. On this picture, one can notice the presence of several areas where a rephasing leads to a clearly visible periodic pattern while the fringes smear out in other regions. The rephasing of the grating pattern occurs moreover at integer multiples of a characteristic length L_T , the Talbot length, function of the gratings pitch d and the De Broglie wavelength λ_B :

$$L_T = \frac{d^2}{\lambda_B}. \quad (3.28)$$

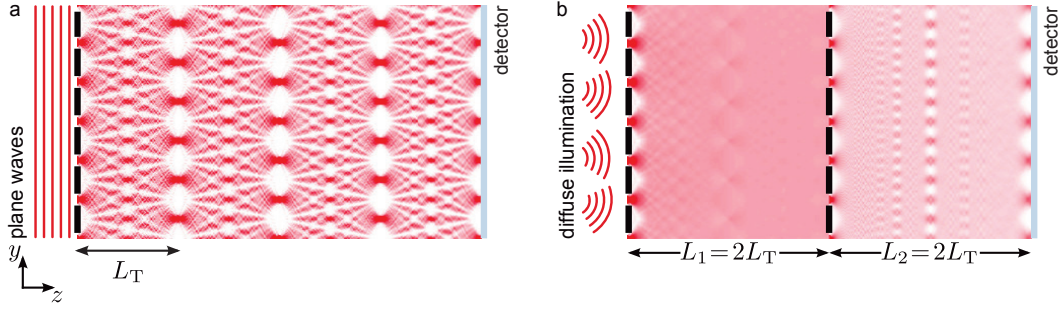


Figure 3.10: (a) The Talbot carpet, resulting from the near field interference of a plane wave on a grating. Rephasings of the pattern occur at distances from the grating equal to the Talbot length L_T , or at any multiple integers of L_T . (b) For sources presenting no spatial coherence (diffuse illumination), the Talbot effect can still be observed by placing a first grating at a distance L_T from a second grating. (image adapted from [81]).

Spatial coherence

As H. F. Talbot had the intuition by varying the spatial extension of the source, the formation of the Talbot carpet does rely on the spatial coherence of the beam. In 1948, E. Lau demonstrated that this requirement can actually be circumvented by positioning a second grating at a distance L_T from the first one [102]. The effect is illustrated in figure 3.10(b). An uncollimated beam passing through a first grating creates the coherence necessary to form several rephasing upstream of a second grating. By doing so, a detector placed at a multiple integer of the Talbot length is then able to observe the interferometric fringes. But here again, the pattern periodicity is equal to the one of the gratings, which is challenging to observe for usual detectors. In the Talbot-Lau interferometer, a third grating is hence placed at the position of a rephasing. Using the moiré trick presented in section 3.1.2, it enables one to enlarge the interferometric fringes. We recall the periodicity of the macroscopic fringes D , for small tilt α of the third grating: $D = d/\alpha$.

Regimes

The Talbot-Lau interferometer can be described mathematically using the Wigner representation [103], as it links the particles wave-functions to their probability distributions in phase space. A rigorous theoretical treatment is given in reference [81]. It deals in summary with the free evolution of the Wigner function between the gratings and its passage through each of them. The signal upstream of the third grating can be finally expressed as [81]:

$$I_{\text{TL}}(x) = \sum_{n \in \mathbb{Z}} c_n \exp\left(\frac{2i\pi n}{D}x\right) \quad (3.29)$$

where the TL subscript stands for Talbot-Lau. The complex coefficients c_n are given by:

$$c_n = 2\eta^3 \text{sinc}^3(\pi\eta n) \cos(\pi\eta n) \sum_{j \in \mathbb{Z}} \exp\left(2i\pi n(n-j)\frac{L}{L_T}\right), \quad \forall n \in \mathbb{N}. \quad (3.30)$$

One can notice that the Fourier coefficients are very similar than the ones of the moiré deflectometer, given in equation (3.4), as the only difference is the presence of a phase term $\exp\left(2i\pi n(n-j)\frac{L}{L_T}\right)$. In the case of $L \ll L_T$, or equivalently for short wavelengths λ_B , this phase term vanishes such that we retrieve the exact same expression than for the moiré deflectometer⁴. Depending on the distance spacing the gratings, different regimes are hence reachable. We have seen that the situation where $L = L_T$ corresponds to the Talbot-Lau interferometer, where near-field diffraction has to be taken into account. The last case, where $L \gg L_T$, corresponds instead to the regime in which the diffraction orders become well-separated. In this regime, the first grating splits the beam while the second gratings recombines the different orders of diffraction. It can be seen as the analogue of an optical Mach-Zehnder interferometer [104, 105] but working with matterwave. The different regimes are summarized in table 3.2.

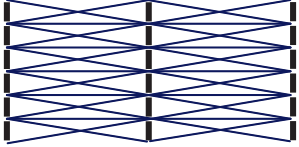
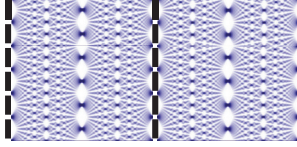
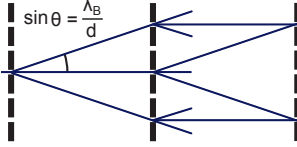
moiré deflectometer	Talbot-Lau interferometer	Mach-Zehnder interferometer
		
$L \ll L_T$	$L = L_T$	$L \gg L_T$

Table 3.2: The different regimes of a set of three transmission gratings spaced by a distance L . The moiré deflectometer is a specific case for which L is small in front of the Talbot length L_T .

A second remark can be made concerning the expression (3.30). When the distance L matches exactly the Talbot length, or any of its multiple, the exponent $n(n-j)L/L_T$ becomes an integer and the phase term vanishes. It turns out that the Talbot-Lau fringes have thus the same shape as the moiré fringes. In other words, there is no way to distinguish the nature (quantum or classical) of the fringes by looking only at the pattern formed. To this extent, we will show now that the fringes visibility represents a better observable.

⁴We recall the relation $a_n = c_n + c_{-n}$, linking the real and complex Fourier coefficients.

3.3.3 Visibility modulations

An exact expression of the fringe visibility can be deduced from equation (3.30), by evaluating the intensity at its minimum, for $x = 0$, and at its maximum, for $x = D/2$. If the gratings are separated by L_T , scanning the position of the detector along the z axis, therefore modifying L , would reveal periodically the rephasings of the Talbot carpet, the signature of the quantum regime. If the last grating is fixed, an equivalent approach is to vary the Talbot length itself, as it scales with the square root of the energy of the incident beam E_k :

$$L_T = \frac{d^2}{\lambda_B} = \frac{d^2 \sqrt{2mE_k}}{h}. \quad (3.31)$$

The visibility of the fringes as a function of the proton beam energy is given in figure 3.11, for $L = 73$ mm, $\eta = 40\%$ and $d = 257$ nm. Whereas the visibility is independent of the energy in the classical case (gray line), one can notice the presence of several modulations due to rephasings of the Talbot carpet in the quantum case. It constitutes hence evidence of the wave behavior of protons.

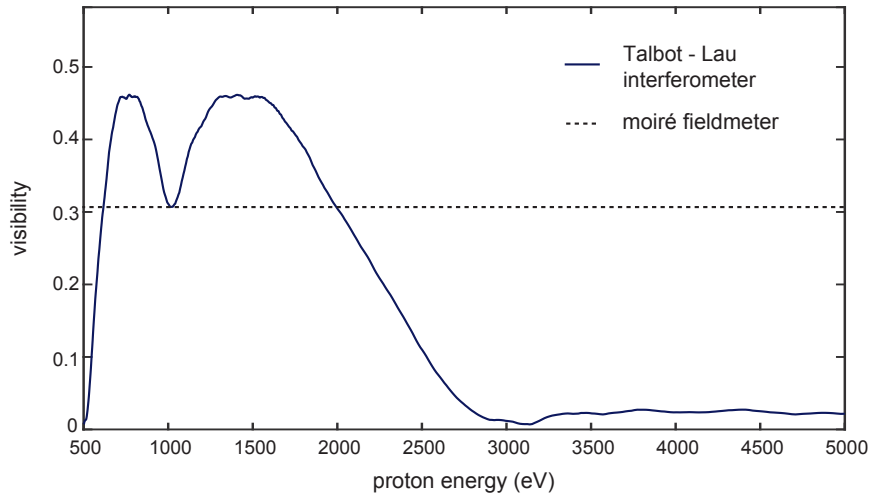


Figure 3.11: Visibility of the interferometric fringes as a function of the proton energy for $\eta = 40\%$. The length between the gratings is fixed to 73 mm, corresponding to the Talbot length of 1 keV protons and the gratings pitch is 257 nm. If the protons behaved classically, the visibility would be independent of the beam energy, as indicated by the dashed line. (courtesy of A. Demetrio).

3.4 Summary

3.4.1 Moiré fieldmeter

We have seen in this section that the knowledge of two vertical shifts, measured with ions species having different charge-to-mass ratios, enables one to decouple magnetic and electric fields. The minimal fields that can be measured by the moiré fieldmeter are ultimately limited by the number of particles detected. However, as the particle beam presents a certain energy spread, the patterns formed by slow and fast particles are likely overlap in presence of a field. In order to keep the pattern undisturbed, one should hence make sure to keep the surrounding fields below a certain threshold: the critical fields.

proton energy		100 eV	1 keV	10 keV
velocity	$\langle v \rangle$ (m.s ⁻¹)	$1.38 \cdot 10^5$	$4.38 \cdot 10^5$	$1.38 \cdot 10^6$
Larmor radius	R_L (m)	14.5	45.7	145
critical electric field	E_c (V.m ⁻¹)	13.7	137	1370
critical magnetic field	B_c (G)	0.19	6.25	19
minimal electric field	E_{\min} (mV.m ⁻¹ .Hz ^{-1/2})	0.436	4.36	43.6
minimal magnetic field	B_{\min} (μG.Hz ^{-1/2})	31.5	99.6	315

Table 3.3: Some quantities, relevant for the moiré fieldmeter, for gratings pitch $d = 40 \mu\text{m}$, separated by $L = 171 \text{ mm}$. The minimal and critical fields are calculated for a 1 % energy spread and a source intensity of 10^4 protons per second (0.1 pA). The Larmor radius is calculated for a magnetic field $B = 1 \text{ G}$.

Some relevant quantities of the moiré fieldmeter are listed in table 3.3. They are calculated for gratings having a pitch $d = 40 \mu\text{m}$, separated by a distance $L = 171 \text{ mm}$. The Larmor radius R_L is always larger than the apparatus length L for proton energy between 100 eV and 10 keV, such that the magnetic deflection can be assumed parabolic. The critical fields, calculated for an energy spread of 1 % are 137 V.m^{-1} and 4.42 G for a 1 keV beam. Finally, for proton energy of 100 eV, the fieldmeter is able to resolve fields as low as $0.44 \text{ mV.m}^{-1}.\text{Hz}^{-1/2}$ and $22.3 \mu\text{G.Hz}^{-1/2}$.

3.4.2 Talbot-Lau interferometer

Extensively tested with neutral particles, the wave-particle duality formulated by De Broglie has never been observed for charged particles heavier than electrons. Compared to other devices, the advantage of the Talbot-Lau interferometer lies in the fact that it does not require the ions to be collimated. The achievement of proton interferometry with such a device seems hence promising. It has been also stressed that the wave behavior of the protons is unambiguously identified if the visibility of the interferometric fringes presents a characteristic evolution with the proton energy.

proton energy		1 keV	10 keV	100 keV
velocity	$\langle v \rangle$ (m.s ⁻¹)	$4.38 \cdot 10^5$	$1.38 \cdot 10^6$	$4.38 \cdot 10^6$
De Broglie wavelength	λ_B (m)	$9.1 \cdot 10^{-13}$	$2.9 \cdot 10^{-13}$	$9.1 \cdot 10^{-14}$
Talbot length	L_T (mm)	72.4	229	724
critical electric field	E_c (V.m ⁻¹)	4.8	48	480
critical magnetic field	B_c (G)	0.23	0.69	2.26
minimal electric field	E_{\min} (mV.m ⁻¹ .Hz ^{-1/2})	0.15	1.5	150
minimal magnetic field	B_{\min} (μG.Hz ^{-1/2})	3.49	11.0	34.9

Table 3.4: Some of the quantities relevant for the proton Talbot-Lau interferometer, calculated for gratings with pitch $d = 257 \text{ nm}$ separated by $L = 73 \text{ mm}$. The minimal and critical fields are calculated for a source delivering 10^4 ions per second ($I = 0.1 \text{ pA}$) with 1 % energy spread.

Some relevant quantities of the proton Talbot-Lau interferometer are listed in table 3.4. They are calculated for gratings having a pitch $d = 257 \text{ nm}$, separated by a distance $L = 73 \text{ mm}$.

Compared to the moiré deflectometer (see table (3.3)), the critical fields, scaling with the grating pitch d , are obviously lower. In other words, the interferometer is more sensitive to stray fields. To ensure that the pattern does not smear out, one has to prevent the surrounding field to be higher than 4.8 V.m^{-1} and 0.16 G for a 1 keV beam.

4 | Experimental Setup

We have seen in the previous chapter that Talbot-Lau interferometry is a remarkable technique to highlight the wave behavior of protons. We present in this chapter the experimental setup of the Proton Interferometry eXperImEnt (or PIXIE). It is composed of an ion source placed in a dedicated beamline, a neutralization chamber, the Talbot-Lau interferometer and an imaging detector. The performance of the source, along with innovative methods to evaluate the beam size, energy distribution and composition are emphasized. The interferometer, consisting of three gratings having an extremely small pitch of 257 nm, is then presented. In order not to disturb the interferometer, a special attention is paid on maintaining the electric and magnetic field below the critical values: $E_c = 4.8$ V/m and $B_c = 230$ mG (see previous chapter). For this reason, the interferometer is placed inside a dedicated magnetic shield. Furthermore, a moiré fieldmeter is integrated to the setup. It consists of a set of three gratings, having a pitch of 40 μm , which allows one to monitor in real time the magnitude of the electric and magnetic fields inside the shield. We detail also the principle of the neutralization chamber, used to convert the beam of protons into a beam of hydrogen. Since the masses of hydrogen and protons are comparable (and so are their De Broglie wavelengths), it offers the possibility to perform Talbot-Lau interferometry of hydrogen atoms with the exact same device. Because of their electrical neutrality, hydrogen atoms are insensitive to Lorentz forces, and can therefore serve as a reference for the fieldmeter. The last section is dedicated to the imaging detector, consisting of a microchannel plate (MCP), a phosphor screen and a CMOS camera. We will see that in the regime where the protons are detected one by one, the coordinates of each impact on the detector can be determined with a resolution of few microns.

4.1 Overview

A photograph and a schematic view of the Proton Interferometry eXperImEnt (PIXIE) setup is shown in figure 4.1.

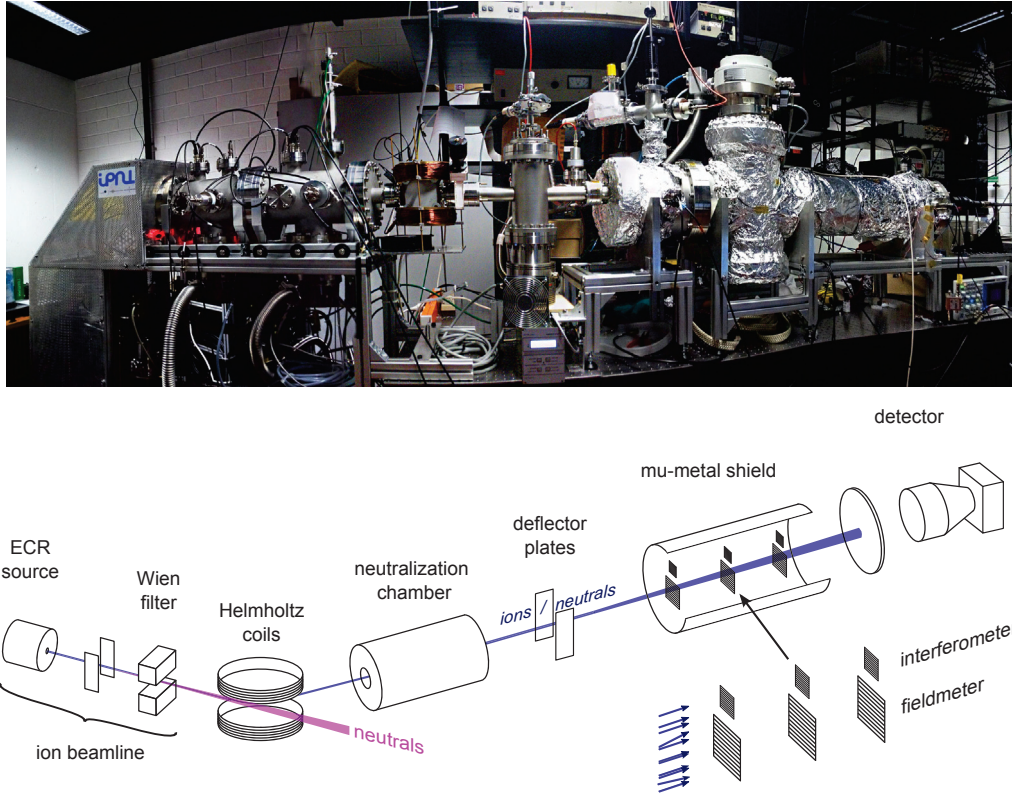


Figure 4.1: Photograph and schematic view of the Proton Interferometry eXperImEnt (PIXIE) setup. Two Helmholtz coils distinguish the ions produced by an Electron Cyclotron Resonant (ECR) source from neutral particles. A neutralization chamber can be used to form a beam of hydrogen atoms. The Talbot-Lau interferometer (see previous chapter) is placed in a mu-metal shield, reducing both electric and magnetic field. A moiré fieldmeter is used to measure the surrounding electric and magnetic fields which might disturb the interferometer. The patterns of both the fieldmeter and the interferometer are finally observed on a detector consisting of a microchannel plate (MCP), a phosphor screen and a CMOS camera.

An Electron Cyclotron Resonant (ECR) source provides a beam of ions whose energy can be tuned from 0 to 2 keV. The source is integrated to a beamline that allows one to focus the beam and adjust its position. Along with protons, H_2^+ and H_3^+ ions but also photons and neutral atoms can be produced. To select the different types of ions according to their charge-to-mass ratios, a Wien filter is hence integrated to the beamline. At the exit of the beamline is placed a pair of Helmholtz coils so as to distinguish the ions from the neutral particles. The protons pass then through a neutralization chamber, consisting of a nitrogen gaseous target and a set of deflector plates. By tuning the nitrogen pressure from 10^{-9} to 10^{-3} mbar, protons can capture an electron from the nitrogen and form a beam of hydrogen atoms. The beam is then directed toward the Talbot-Lau interferometer. It consists of three gratings with pitch $d = 257$ nm. A moiré fieldmeter is used to measure the surrounding electric and magnetic

fields which might disturb the interferometer. It consists in a second set of gratings (pitch $d = 40 \mu\text{m}$) placed underneath the interferometer. To distinguish between the two sets, we refer respectively to the interferometer and the fieldmeter in the following. Both devices are placed in a cylindric shield, made of metal having a high magnetic permeability (μ -metal). Although its primary goal is to attenuate the magnetic field, the shield acts also as a Faraday cage, reducing therefore the electric field in the volume of the interferometer. The patterns formed upstream of the fieldmeter and the interferometer are finally visualized on an imaging detector.

The different parts of the PIXIE setup are detailed in the following sections. The ion beamline is characterized in a first time. For the design chosen, the efficiency of the neutralization chamber is then calculated. The optimal pressure of nitrogen in the chamber is evaluated experimentally. Concerning the interferometer, the magnetic field expected inside the μ -metal shield is estimated. It will be compared in next chapter with the one measured by the fieldmeter. The stakes of the grating metalization and the precision needed to align them with respect to each other are then discussed. The last section is dedicated to the performance of the detector.

4.2 Ion beamline

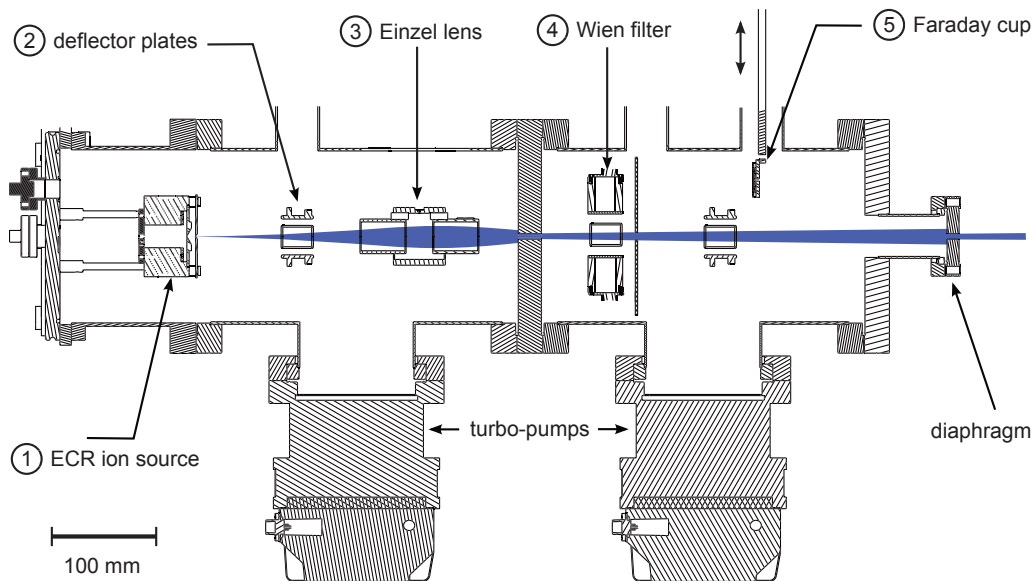


Figure 4.2: View of the ion beamline developed at IPNL. (1) An Electron Cyclotron Resonance (ECR) source delivers a beam of $6 \cdot 10^{12}$ ions per second at an energy up to 2 keV. (2) The horizontal and vertical positions of the beam are then controlled by the mean of two pairs of deflectors plates. (3) An electrostatic lens, or Einzel lens, focuses the ions, later selected by a Wien Filter (4). Finally, a Faraday cup (5) monitors the intensity of the beam.

Developed at the Institut de Physique Nucléaire de Lyon (IPNL) [106], the ion beamline is the first part of the PIXIE setup. As shown in figure 4.2, it is made of:

- 1) An Electron Cyclotron Resonance (ECR) ion source. It consists of a cylindric cavity containing dihydrogen at a pressure of 10^{-5} mbar. Inside the cavity, the dihydrogen is ionized by the mean of an antenna carrying a microwave excitation. By the mean of an extraction electrode, the ion source is able to deliver a current up to $1 \mu\text{A}$, which corresponds to approximately 6.10^{12} particles per second;
- 2) Two pairs of deflector plates used to adjust the horizontal and vertical positions of the beam.
- 3) An electrostatic lens, composed of three coaxial ring shaped electrodes. The middle electrode is connected to a high voltage while the others are electrically grounded. The electrostatic lens, or Einzel lens, is used to focus the beam.
- 4) A Wien filter, used to select the different types of ions according to their q/m ratio.
- 5) A Faraday cup which monitors the flux of ions. It consists in a disk of copper of 22 mm in diameter that can be placed in front of the beam. When the particles hit the Faraday cup, the metal gains a small net charge which is evacuated to a pico-amperemeter¹.

A Pirani gauge and two cold cathode gauges² monitor the pressure within the vacuum chamber. Although the pressure measured in the vicinity of the ion source is typically of the order of 10^{-5} mbar when the source is running, the pressure at the exit of the beamline reaches in comparison 10^{-8} mbar under normal conditions of use. The whole beamline is operated by a Labview [108] interface.

4.2.1 Ion source

ECR sources

Thanks to their long lifetime, and the quasi absence of maintenance required, the use of ECR sources has acquired a unique importance in various technological fields over the last 30 years. In such sources, electrons heated by a microwave excitation, collide onto atoms or molecules of the gas to produce ions. In a presence of a magnetic field B , the ionization is sustainable if the frequency of the microwave excitation ω_{RF} matches the cyclotron frequency of the electrons ω_c :

$$\omega_{\text{RF}} = \omega_c = \frac{eB}{m_e}, \quad (4.1)$$

where e and m_e are the electron charge and mass. This is the electronic cyclotron resonance condition. In most sources, the microwave frequency (or RF frequency) is however imposed by a generator such that the magnetic field allowing ionization is fixed. For a 2.45 GHz excitation frequency, the magnetic field fulfilling the ECR condition is for instance $B_{\text{ECR}} = 876$ G. Inside the cavity, the ionization occurs therefore only where the magnetic field matches B_{ECR} .

¹model Keithley 6400.

²Varian IMG 100.

Predominant reactions in ECR sources

Once the plasma is formed, several processes can possibly occur within the volume of the cavity, leading either to ionization or neutralization of the species [109]:

- **Electron impact ionization.** Ions are produced through the direct collision of a free energetic electron on an atom or a molecule A , if the electron energy is larger than the ionization potential of the atom:



The cross-section of this mechanism is maximal when the energy of the electrons is 2 to 3 times the ionization potential of the atom [109].

- **Charge-exchange.** Already presented in chapter 1, the charge-exchange mechanism is the process corresponding to the exchange of an electron with an atom B of the plasma. It corresponds to the reaction:



Similarly to the antihydrogen production reaction in AEGIS, the probability that charge-exchange occurs is determined by the nature of particles A and B and by the relative velocity between the particles (Massey criterion).

The COMIC source

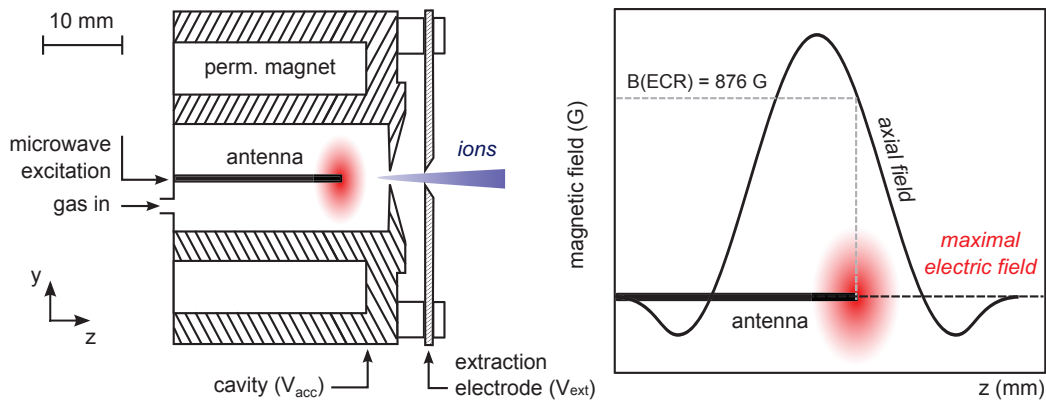


Figure 4.3: (left) Side view of the ion source and (right) shape of the magnetic field along the source axis. An antenna carries a 2.45 GHz microwave excitation, ionizing the hydrogen gas. The cylindrical cavity is at a voltage V_{acc} . Four permanent neodymium magnets, placed around the cavity, create a field which overcomes locally the ECR field $B_{\text{ECR}} = 876$ G. The length of the antenna is chosen such that the electric field is maximal in the zone where the magnetic field matches the ECR field.

The COmpact MIcrowave and COaxial (or COMIC) source is shown schematically in figure 4.3 (left). In this ECR source, an axi-symmetric magnetic field is ensured by four neodymium permanent magnets placed azimuthally and creating a gradient from the middle of the cavity toward the extraction electrode. Inside the cavity is placed a coaxial antenna carrying a 2.45 GHz excitation and three couplers, used to increase locally the electric field to 10^4 V/m [112]. As seen on figure 4.3 (right), the length of the antenna is chosen to maximize the electric field in the area where the magnetic field matches the ECR field. Once the plasma is formed, an

extraction electrode set at a negative voltage allows one to pull out positively charged ions. In our setup, the extraction electrode consists in a 2 mm-thick aluminum plate placed downstream of the cavity with a round aperture of 0.5 mm in diameter. The cavity is kept at a positive voltage V_{acc} , ranging from 0 to 2000 V. The extraction voltage V_{ext} , referenced with respect to V_{acc} , varies from 0 to -2000 V.

Beside charged particles, ultra-violet photons originating from the deexcitation of molecules of the gas, can also leave the source. The COMIC source, developed at the Laboratoire de Physique Subatomique et de Cosmologie de Grenoble [107], is presented in more details in reference [112].

4.2.2 Gas composition

The bottle connected to the ion source contains pure hydrogen at a level of 10 ppm. However, due to the possible leaks of the pipe system, it is likely that the gas presents a small fraction of air at the level of the cavity. We estimate now the fraction of dihydrogen in the gas ionized.

Paschen Law

When placed in a gas at a certain pressure P , an electrical breakdown can possibly occur between two electrodes presenting a voltage difference. The Paschen law gives the relationship between the breakdown voltage V_b and the pressure of the gas [113]:

$$V_b = \frac{K P d}{\ln(K' P d) - \ln\left(\ln\left(1 + \frac{1}{\gamma}\right)\right)}, \quad (4.4)$$

where K and K' are empirical constants depending on the gas considered, γ is a factor accounting for the electrodes geometry and d is the distance between the two electrodes. The Paschen coefficients for air and dihydrogen are listed in table 4.1. Introducing x the fraction of dihydrogen in the gas, we have for a mixture of dihydrogen and air: $K' = x \cdot K'_{H_2} + (1-x) \cdot K'_{air}$, and $K = x \cdot K_{H_2} + (1-x) \cdot K_{air}$.

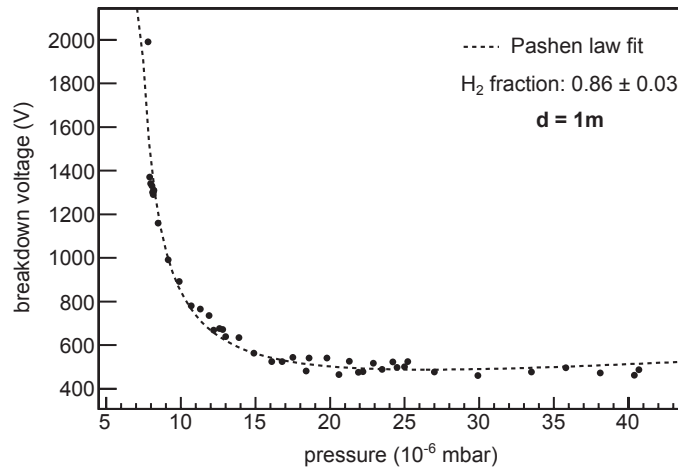


Figure 4.4: The cavity breakdown voltage as a function of the pressure measured in the vicinity of the source. The breakdown voltage is the voltage read from the power supply for a voltage set to 2 kV. The distance between the cavity and the bottle is $d = 1$ m. The Paschen law, fitted to the data points, enables one to estimate the fraction of dihydrogen in the gas entering the ion source.

	air	H_2
K' (mbar ⁻¹ cm ⁻¹)	11	4
K (V mbar ⁻¹ cm ⁻¹)	274	98

Table 4.1: Paschen coefficients of air and dihydrogen.

Air contamination

In our setup, an electrical breakdown can possibly occur within the pipe linking the bottle (electrically grounded) to the source (at voltage V_{acc}). The voltage at which the electrical breakdown occurs, as a function of the pressure measured in the vicinity of the source, is given in figure 4.4. Considering the fraction of hydrogen x , and the proportionality factor between the pressure measured nearby the source and the pressure within the plastic pipe, the Paschen law is fitted to the data points. Estimated from the fit, the fraction of hydrogen at the level of the source is:

$$x = 0.86 \pm 0.03. \quad (4.5)$$

Electrical breakdowns are however a drawback to the proper operation of the beamline since they prevent one to set the source voltage. As one can see in figure 4.4, a way to get rid of this effect is to reduce the gas pressure inside the source. Indeed, for pressure below $7 \cdot 10^{-6}$ mbar, the maximal voltage that can be applied without experiencing any breakdown exceeds 2 kV. Since the pressure and the distance between the electrodes play a similar role in equation (4.4) (P and d can be interchanged), another strategy is to shorten the distance between the electrodes. To avoid electrical breakdowns, the 1 m pipe was hence replaced by a shorter (~ 1 cm) insulating ceramic pipe.

4.2.3 Faraday cup

A photograph of the custom made Faraday cup (FC) is shown in figure 4.5 (left). Unlike standard Faraday cups, the main limitation of this design is that it does not collect secondary electrons emitted by the Faraday cup material. As seen in figure 4.5 (right), this effect is not negligible: one incident proton at 2 keV may lead to the emission of one to two electrons [117]. If a proton hits the FC, the charge read on the pico-amperemeter is therefore not e but $2e$ (in the case of one secondary electron) and the absolute flux read by the cup is thus overestimated by a factor two.

4.2.4 Operating settings

We present now some important settings of the source such as the energy at which the ions can be delivered or the effect of the extraction electrode. We show later how the ion intensity evolves with the voltage of the electrostatic lens.

Energy range

The acceleration voltage V_{acc} and the kinetic energy of the ions E_k are linked by the relation:

$$q \cdot V_{\text{acc}} = E_k. \quad (4.6)$$

Although the COMIC source has been operated until $V_{\text{acc}} = 20$ kV [112], the maximal energy of the ions depends ultimately on the voltage where sparks start to appear between the source

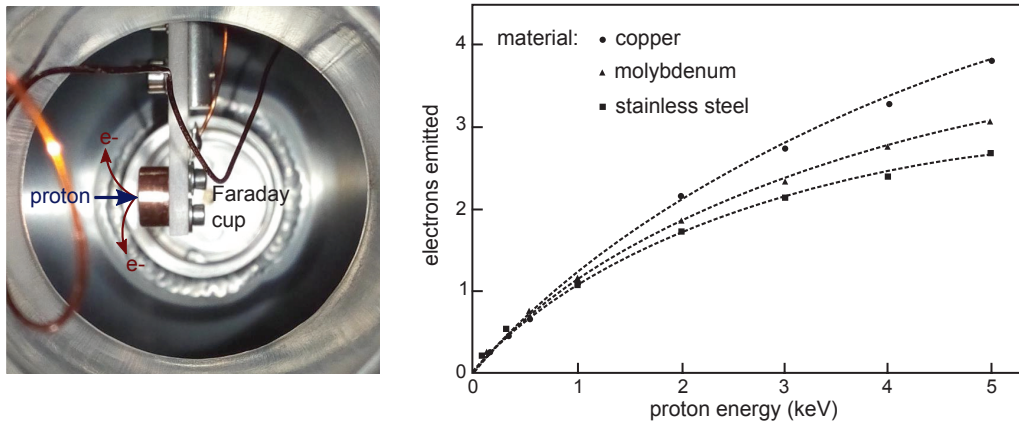


Figure 4.5: (left) Photograph of the Faraday cup. An ion hitting the cup creates secondary electrons which are not collected. The number of secondary electron depends on the energy of the impinging ion, or the cup material. The right panel shows the number of electrons as a function of the energy of protons on copper. (adapted from reference [117]).

and the rest of the vacuum chamber. The minimal energy the ions can reach, is on the other hand hard to evaluate. Indeed, one should keep in mind that the slower are the ions, the higher is their sensitivity to both electric and magnetic fields. As a consequence, slow ions are likely to be deflected from the beamline axis, such that the flux exiting the beamline gets effectively lower. The ion intensity as a function of the source acceleration voltage is given in figure 4.6. The flux is constant between $V_{\text{acc}} = 400$ to 2000 V but drops for $V_{\text{acc}} < 400$ V.

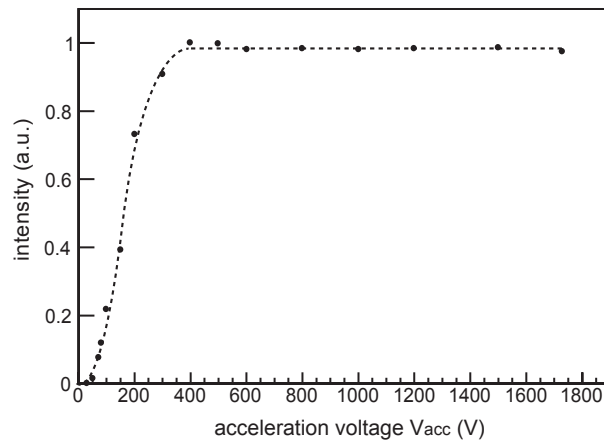


Figure 4.6: The ion intensity as a function of the ion acceleration voltage V_{acc} . The ions, sensitive to stray fields, are likely to be deflected from their nominal trajectory for low acceleration voltages. As a consequence, the intensity rises and reaches a plateau for acceleration voltage above $V_{\text{acc}} = 400$ V. For each point, the extraction electrode is set to 2 kV.

Extraction voltage

In order to extract positively charged ions, the voltage applied on the extraction electrode V_{ext} , or extraction voltage, is set to negative values. The evolution of the ion flux with the

extraction voltage is displayed in figure 4.7. It is worth to notice that the extraction voltage does not influence the ion energy. Indeed, the electric potential varies from V_{acc} at the level of the cavity to zero as the beamline is electrically grounded. The difference is therefore equal to V_{acc} , no matter how the potential evolves in between.

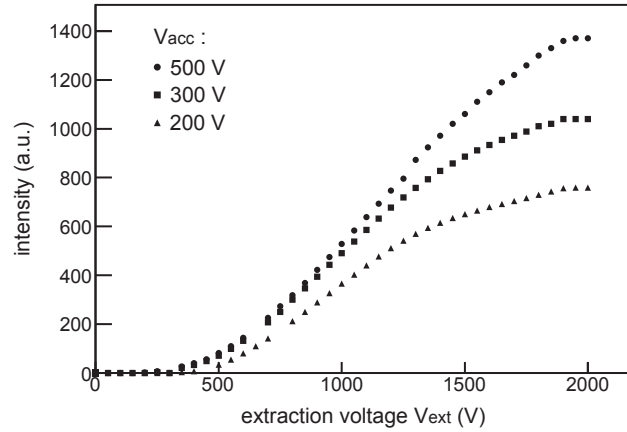


Figure 4.7: The ion intensity as a function of the extraction voltage (in absolute value), for several acceleration voltages.

Lens voltage

The Einzel lens consists of a cylindrical electrode, set at a certain voltage, placed between two cylindrical electrodes electrically grounded. When a voltage is applied on the middle electrode, the ions experience a kick toward the axis and get therefore focused. Depending on the lens voltage, different regimes are hence accessible, as shown in figure 4.8.

When no voltage is applied, the beam presents a certain overlap with the detector (FC) surface. As long as the voltage increases, the ions get more and more focused until an optimum, corresponding to the maximal fraction that can be collected by the FC. The focusing point passes then downstream of the FC, such that the beam does not fully overlap the detector. At a certain point, the electric potential in the middle of the lens is higher than the ion energy and the ions are reflected backward. In the PIXIE setup, the lens voltage is adjusted to reduce or increase the flux of ions entering the interferometer.

4.2.5 Energy spread

In order to measure the energy distribution of the ion beam, a fine mesh set at a voltage V_{mesh} , is placed a few millimeters in front of the Faraday cup. A photograph of the mesh and the Faraday cup is shown in figure 4.9.

The ions whose the kinetic energy satisfies $E > V_{\text{mesh}}$ are able to cross the mesh and are reflected otherwise. For a beam presenting a certain energy distribution $f(E) = dN/dE$, the intensity read on the Faraday cup is therefore the integral of the energy distribution from the mesh voltage to infinity:

$$I = \frac{I_0}{\int_0^{+\infty} f(E)dE} \cdot \int_{V_{\text{mesh}}}^{+\infty} f(E)dE, \quad (4.7)$$

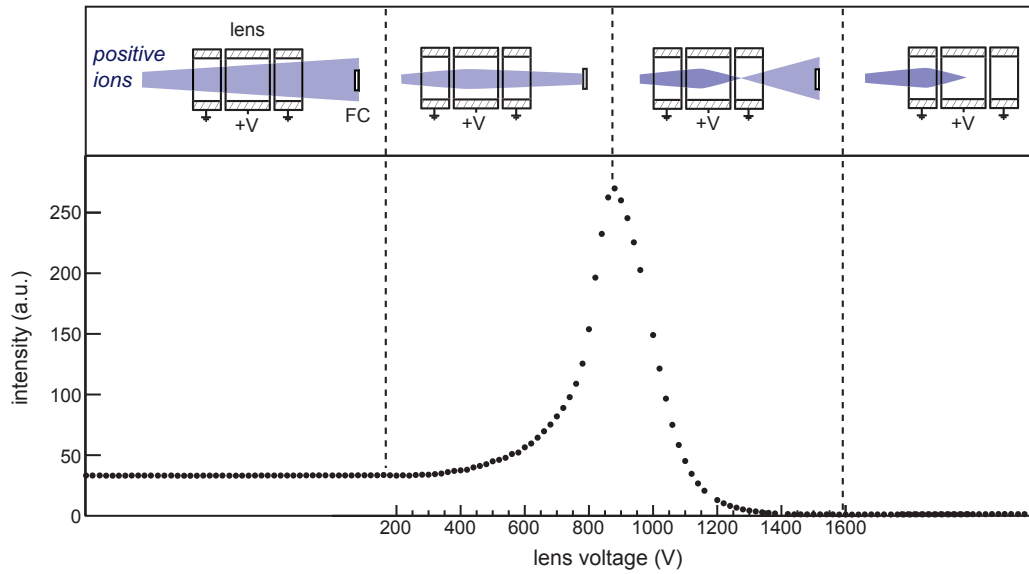


Figure 4.8: The ion intensity, measured on the Faraday cup (FC), as a function of the lens voltage, for a 700 eV energy. The cartoon on the upper side represents the three rings of the lens along with the ion trajectories (blue). From left to right, the ions get more and more focused until a maximal fraction is collected by the Faraday cup. The focusing point of the lens passes then before the FC, such that the beam does not fully overlap the cup surface. At a certain point, the electric potential in the middle of the lens overcomes the ion energy and the ions are reflected.

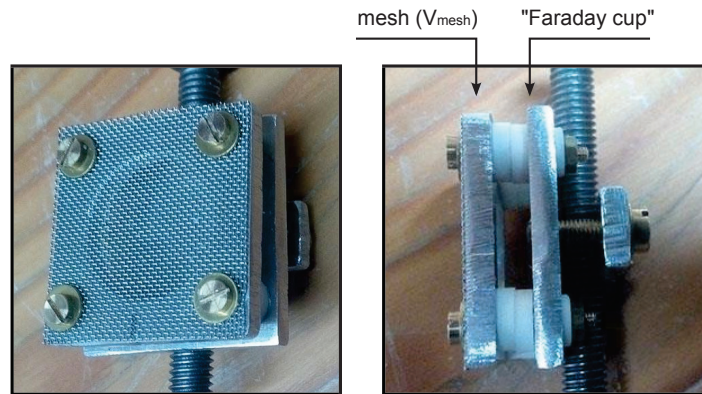


Figure 4.9: Photograph of the mesh and the Faraday cup.

where I_0 is the intensity measured when no voltage is applied on the mesh. Since the energy distribution is assumed to vanish at infinity, the derivative of this expression with respect to the mesh voltage gives hence the energy distribution:

$$f(E) = - \frac{dI}{dV_{\text{mesh}}} . \quad (4.8)$$

The intensity read on the Faraday cup as a function of the mesh voltage is displayed in fig-

ure 4.10 (left), for a $V_{\text{acc}} = 1500$ V acceleration voltage. The derivative is shown in the right plot. It is centered on the acceleration voltage and present a certain spread $\Delta E = 20$ eV. The spread, is hence around

$$\frac{\Delta E}{E} = 1.3\%. \quad (4.9)$$

While the distribution drops sharply to zero for $E > V_{\text{acc}}$, one can notice the presence of a long tail toward low energies. It can be interpreted as follows. Even though the beam is quasi monochromatic at the exit of the source (the acceleration voltage do not vary by more than 1 V according to the power supply specification), the ions are likely to bounce on the different parts of the beamline (for instance on diaphragms). It results in successive losses of energy, spreading the energy distribution toward the left.

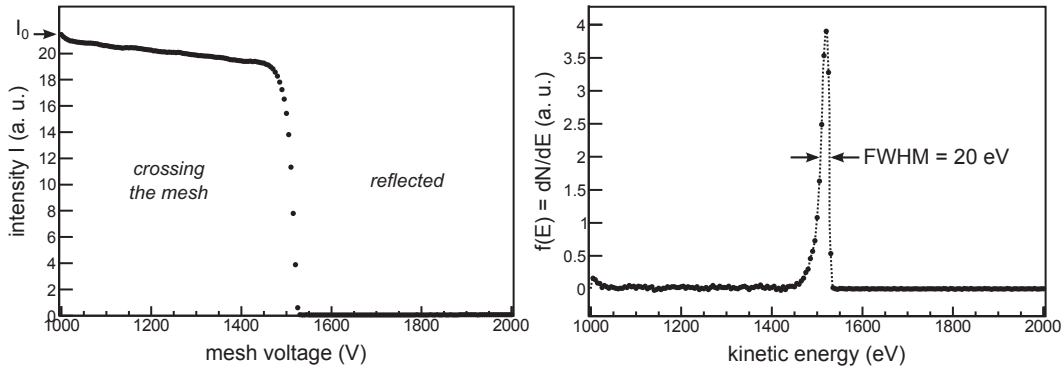


Figure 4.10: (left) The intensity read on the Faraday cup as a function of the mesh voltage and (right) the deduced energy distribution. The mesh is placed in front of the Faraday cup such that the only particles allowed to pass through must have a kinetic energy higher than the mesh voltage. From the number of particles reaching the Faraday cup, one can hence deduce the energy spectrum of the ion source. The data shown here were acquired for an acceleration voltage $V_{\text{acc}} = 1500$ V. The full width at half maximum (FWHM) of the peak is 20 eV, translating into an energy spread of $\Delta E/E = 1.3\%$.

4.2.6 Beam size

The size of the beam can be estimated by the means of the horizontal and vertical deflector plates located upstream of the Faraday cup. When a voltage difference ΔV is applied between the plates, it creates an electric field \vec{E} deviating the beam from the center as shown in figure 4.11. In the volume between the two electrodes, the particle (charge q , mass m) follows a parabolic trajectory whose equation is:

$$y(z) = \frac{qE_y}{2mv_z^2} \cdot z^2, \quad (4.10)$$

where E_y is the vertical component of the field \vec{E} (the axis convention is given in figure 4.11). The derivative of y with respect to z gives the angle of the beam along the z axis. At the exit of the plates ($z = d$), it is:

$$\left. \frac{dy}{dz} \right|_{z=d} = \frac{qE_y d}{mv_z^2}. \quad (4.11)$$

Introducing Δy the displacement on the Faraday cup, we have thus:

$$\begin{aligned}\Delta y &= L \cdot \left(\frac{dy}{dz} \right)_{z=d} \\ \Delta y &= \frac{Ld}{l} \frac{2q\Delta V}{mv_z^2}\end{aligned}\quad (4.12)$$

The conservation of energy imposes moreover $qV_{\text{acc}} = \frac{1}{2}mv_z^2$, such that the expression can be simplified:

$$\Delta y = \frac{Ld}{l} \frac{\Delta V}{V_{\text{acc}}}.$$
 (4.13)

We see therefore that the displacement of the beam on the Faraday cup depends only on the acceleration voltage V_{acc} , on the voltage difference between the deflector plates and on some geometric factors. For a 700 V acceleration voltage, a $\Delta V = 1$ V difference between the plates moves for example the beam by about 105 μm .

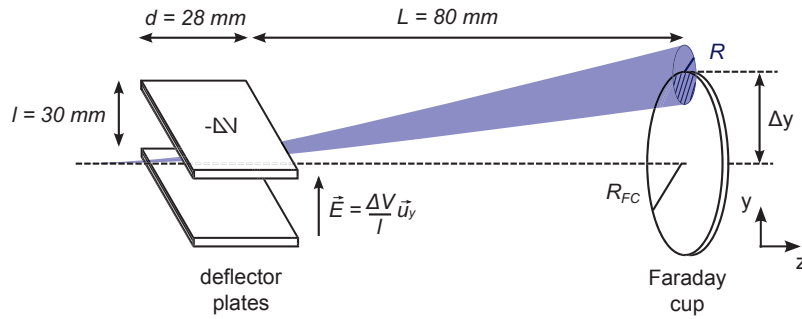


Figure 4.11: Estimation of the beam size. An electric field \vec{E} , created between the deflector plates, deviates the beam by Δy on the Faraday cup.

The intensity read on the Faraday cup as a function of the vertical displacement is shown in figure 4.12. The intensity measured is directly proportional to the number of particles hitting the FC, and therefore to the overlap between the surface of the beam and of the Faraday cup. Within the hypothesis of uniform beam distribution, the analytical expression of the intensity is:

$$\begin{aligned}I(\Delta y) &\propto R^2 \arccos\left(\frac{R^2 + R_{\text{FC}}^2 + \Delta y^2}{2 \cdot R \cdot \Delta y}\right) + R_{\text{FC}}^2 \arccos\left(\frac{R^2 + R_{\text{FC}}^2 + \Delta y^2}{2 \cdot R_{\text{FC}} \cdot \Delta y}\right) \\ &\quad - \frac{1}{2} \sqrt{((R + R_{\text{FC}})^2 - \Delta y^2)(\Delta y^2 - (R - R_{\text{FC}})^2)},\end{aligned}\quad (4.14)$$

where R and R_{FC} are respectively the radii of the beam and of the FC, and Δy the distance between their centers. The experimental data are fitted by this expression such that the corresponding horizontal and vertical radii are:

$$\begin{aligned}R_h &= 3.89 \pm 0.10 \text{ mm}, \\ R_v &= 3.23 \pm 0.06 \text{ mm}.\end{aligned}\quad (4.15)$$

The beam has thus comparable dimensions in horizontal and vertical direction, which makes sense since there is no favored direction in the transverse plane of the beam. The reliability

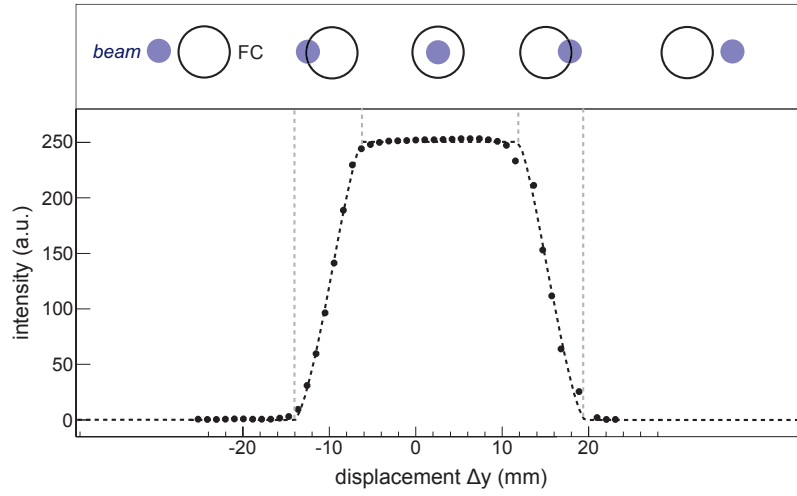


Figure 4.12: Intensity as a function of the vertical displacement of the beam, for a $V_{\text{acc}} = 700$ V acceleration voltage. On the upper panel is displayed schematically the position of the beam with respect to the Faraday cup (FC). Within the hypothesis of an uniform and circular distribution, the fit (black dashed line) is the interception of the Faraday cup and the beam surface.

of this measurement can be tested by extracting also the known radius of the Faraday cup, $R_{\text{FC}} = 11$ mm. According to the fit, it is in agreement with the expected value:

$$\begin{aligned} R_{\text{FC},h} &= 12.89 \pm 0.04 \text{ mm}, \\ R_{\text{FC},v} &= 10.39 \pm 0.02 \text{ mm}. \end{aligned} \quad (4.16)$$

4.2.7 Mass spectrum

Since the purity of a beam is expected to fluctuate according to the type of source used [118], RF power injected, type of magnetic confinement, etc., the beam composition is usually known empirically and its control requires dedicated measurement devices. Here is detailed how the Wien Filter implemented inside the ion beamline differentiates the ions according to their q/m ratio. The results shown in previous section remain valid for a non-filtered beam.

Wien filter

A photograph and a schematic view of the Wien filter is shown in figure 4.13. It consists in two horizontal electrodes (dimensions $28 \times 12 \text{ mm}^2$) spaced by a distance $l = 30$ mm. A vertical magnetic field of approximately 0.13 T is created by a pair of ferrite magnets. A 2 mm slit is juxtaposed at the exit of the Wien Filter to improve the selection efficiency. The ions (mass m , charge q) entering the Wien filter with a certain kinetic energy E_k experience both electrical and magnetic components of the Lorentz force such that the equation of motion is:

$$\vec{a} = \frac{q}{m} \underbrace{(\vec{E} + \vec{v} \times \vec{B})}_{=\vec{0}}. \quad (4.17)$$

The ion is not deflected by the filter if the right term cancels. That is to say, if the voltage difference V between the two electrodes satisfies the relation:

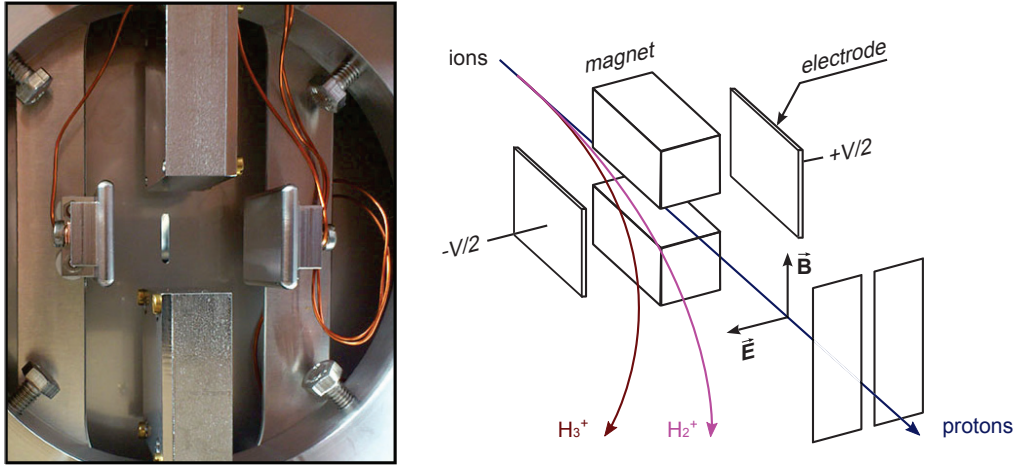


Figure 4.13: Photograph and a schematic view of the Wien filter. The filter consists in two horizontal electrodes, a pair of ferrite magnets and a slit. The orthogonal electric and magnetic fields are used to select the ions according to their q/m ratio.

$$V = lB\sqrt{\frac{2E_k}{m}} = lB\sqrt{\frac{2qV_{\text{acc}}}{m}}. \quad (4.18)$$

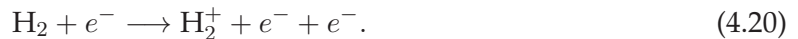
The ions which do not satisfy the equation (4.18) are instead bent toward the wall of the vacuum chamber. The magnetic field created by the two magnets is not homogeneous within the volume of the Wien Filter, leading therefore to an uncertainty on the voltage to apply to select a given ion species. However, as the diameter of the Faraday cup is small in comparison with the distance between the two magnets, we make the hypothesis that the beam experiences only the central region of the Wien filter. The magnitude of the effective field acting here, $B = 0.135 \pm 0.021\text{T}$, has been evaluated with helium. Indeed, due to its noble gas nature, helium is ionized only into He^+ and alpha particles He^{2+} , that can be identified unambiguously on the mass spectrum.

Beam composition

The situation is different in the case of dihydrogen since many types of ions can be formed. The most favorable ion species are H_3^+ (bound system of three protons and two electrons), H_2^+ (two protons and one electron) and protons. H_2^+ and protons are formed by electron impact ionization, as soon as the energy of the electron overcomes 15.4 eV, the ionization potential of molecular hydrogen [119]:



and for H_2^+ :



Charge-exchange mechanism prevails instead for the production of H_3^+ [120]:



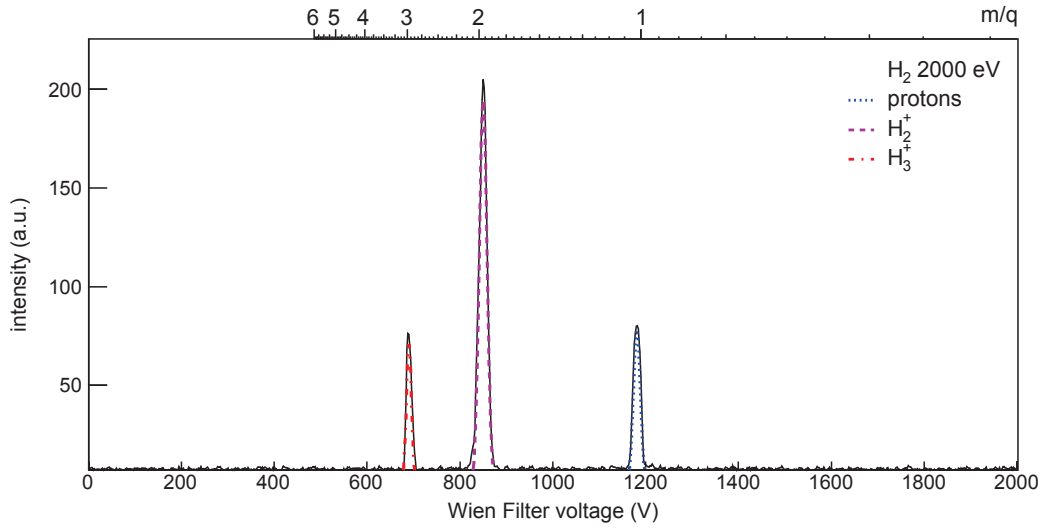


Figure 4.14: The mass spectrum of the ion source for an acceleration voltage $V_{\text{acc}} = 2000$ V. The m/q scale is calculated assuming a 0.135 T magnetic field, as measured during the calibration of the Wien filter. From left to right, three peaks are visible and correspond respectively to H_3^+ (bound system of three protons and two electrons, representing 21 % of the total flux), H_2^+ (two protons and one electron, 57 %) and protons (22 %).

The mass spectrum of the source is shown in figure 4.14. The m/q scale is calculated assuming a 0.135 T magnetic field, as measured during the calibration with helium. The spectrum exhibits clearly three peaks corresponding from left to right to H_3^+ (representing 21 % of the total flux), H_2^+ (57 %) and protons (22 %). The relative proportions of these species vary from one source to another. With an equivalent source working with 700 W microwave power, D. Spence and K.R. Lykke [121] obtain for example a typical fraction of protons around 75 % while in reference [110], a source delivering 3 to 37.5 % of protons is described. As the ionization potential of hydrogen is the highest of the periodical table, it is likely that the amplitude of the microwave excitation plays an important role on the fraction of protons formed. Nevertheless, for the range of microwave power accessible to the ion source, 0 to 30 W, no significant evolution have been observed.

4.3 Neutralization chamber

Once the protons are distinguished from the other ions, the neutralization chamber offers the possibility to form a beam of neutral hydrogen. The underlying idea is to convert the proton beam into hydrogen by charge-exchange reaction with a gaseous target of nitrogen:



For an incoming beam of 5 keV protons, the cross-section of this reaction is $\sigma = 18.5 \cdot 10^{-20} \text{ m}^2$ [123]. The number of protons remaining in the chamber N_p decreases exponentially with the length z of gas traversed. Starting from a beam containing initially N_0 protons, one can write:

$$N_p = N_0 \exp(-\sigma n z), \quad (4.23)$$

where n is the density of nitrogen molecules which can be rewritten³: $n = P/k_B T$, P is the pressure of nitrogen within the neutralization chamber at temperature T , and k_B the Boltzmann constant. The number of hydrogen atoms formed N_H can then be deduced:

$$N_H = N_0 - N_p. \quad (4.24)$$

And the flux of hydrogen atoms formed at the exit of the chamber ($z = L$) is therefore:

$$\Phi_H(P) \propto N_0 \left(1 - \exp\left(\frac{-\sigma P L}{k_B T}\right) \right). \quad (4.25)$$

From equation (4.23), one can calculate the pressure needed to neutralize half of the protons:

$$P_{1/2} = \frac{\ln(2)k_B T}{\sigma L}. \quad (4.26)$$

For a length $L = 20$ cm, it corresponds to $P_{1/2} \simeq 10^{-3}$ mbar at $T = 298$ K. The nitrogen pressure has hence to be maintained at this level in the chamber, while the vacuum is below 10^{-6} mbar in the rest of the experiment. To this end, a differential pumping stage has been realized by placing two diaphragms (10 mm in diameter) at the extremities of the chamber. In order to get rid of the protons which have not been neutralized, an electric field is moreover created by two deflector plates placed upstream of the chamber. A schematic view of the neutralization chamber is shown in figure 4.15.

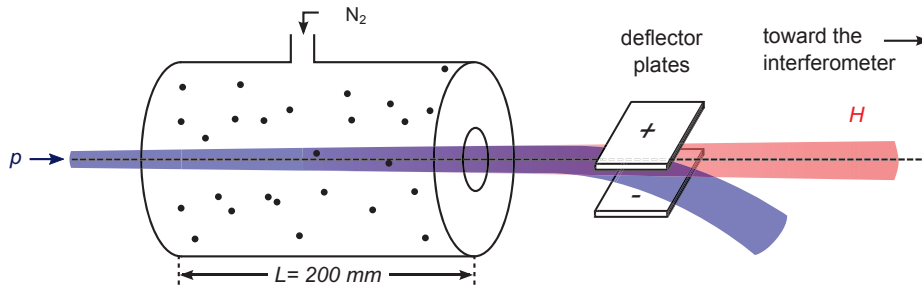


Figure 4.15: Schematic view of the neutralization chamber. The proton beam is sent toward a gaseous target of nitrogen whose the pressure can be adjusted. The hydrogen is then formed by charge exchange reaction between the protons and the nitrogen molecules. Finally, two deflector plates allows one to get rid off the protons that may not have been neutralized.

The flux of hydrogen exiting the neutralization chamber as a function of the pressure of nitrogen is shown figure 4.16, for an incoming beam of 2 keV protons. Different regimes are visible on the plot. For low pressure (regime I), the density of nitrogen is too small to form any hydrogen by charge-exchange. The hydrogen atoms are produced for $P > 10^{-5}$ mbar (II). For a pressure $P > 10^{-2}$ mbar, the average distance between two molecules of nitrogen (or mean free path) become smaller than a few millimeters. As the length of the chamber is $L = 20$ cm, the hydrogen atoms experience thus multiple scattering on the nitrogen molecules (III). Finally, when the pressure overcomes $P = 10^{-1}$ mbar, the density of gas is so important that hydrogen atoms can no longer escape the neutralization chamber (IV).

³For a perfect gas, the number of particles N comprised in a volume V fulfills the relation $PV = Nk_B T$.

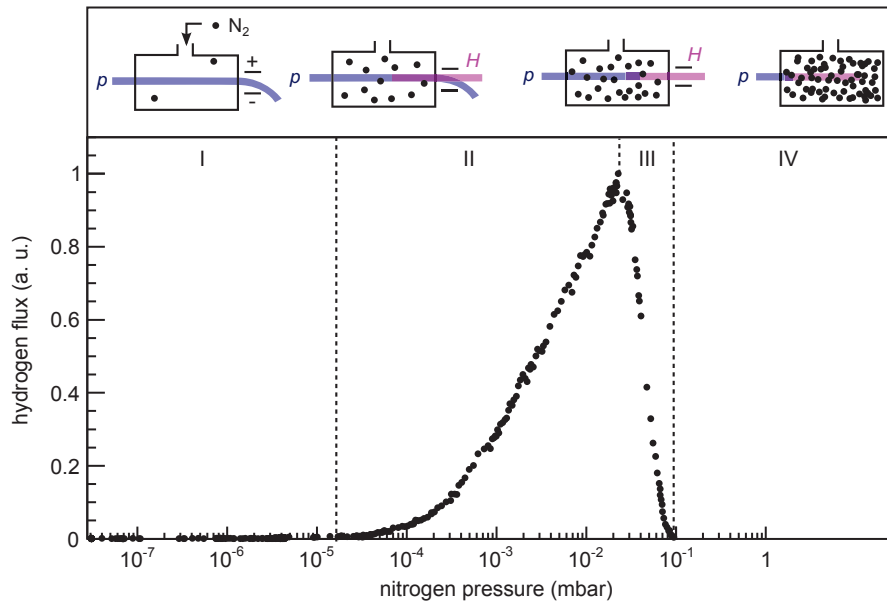


Figure 4.16: The flux of hydrogen exiting the neutralization chamber, as a function of the pressure of nitrogen. The data are acquired for an incoming beam of protons at 2 keV. For low pressure, the density of nitrogen is too small to form any hydrogen by charge-exchange. The hydrogen atoms are produced for $P > 10^{-5}$ mbar. For a pressure $P > 10^{-2}$ mbar, the average distance between two molecules of nitrogen (or mean free path) become smaller than a few millimeters. As the length of the chamber is $L = 20$ cm, the hydrogen atoms experience thus multiple scattering on the nitrogen molecules. Finally, when the pressure overcomes $P = 10^{-1}$ mbar, the density of gas is so high that hydrogen atoms can no longer escape the neutralization chamber.

4.4 Interferometer

A schematic view of the interferometer is shown in figure 4.17. It consists of a Talbot-Lau interferometer, used to show the quantum behavior of the protons and a moiré fieldmeter, used to monitor the electric and magnetic fields while the interferometer is running. Both device consist of three gratings (with a pitch of 257 nm for the interferometer and of 40 μm for the fieldmeter) that are glued on an aluminum holder. To control the fields acting around the interferometer, the gratings of the fieldmeter are placed just below the grating of the interferometer.

The two first holders are mounted on goniometers⁴ allowing rotation of the gratings around the beam axis, with an angular resolution of 1.7 μrad [124]. A translation stage⁵ enables the third holder to move vertically, with a 200 nm resolution [124]. The interferometer and the fieldmeter are mounted on a massive aluminum frame, which ensure the mechanical stability of the device and which act as a Faraday cage. The distance L between the gratings can be adjusted. In the following, we will refer alternatively to the “short” configuration, corresponding to $L = 73$ mm, and the “long” configuration, corresponding to $L = 171$ mm.

⁴ANGt101 RES from attocube [124]

⁵ANPz101 RES from attocube [124]

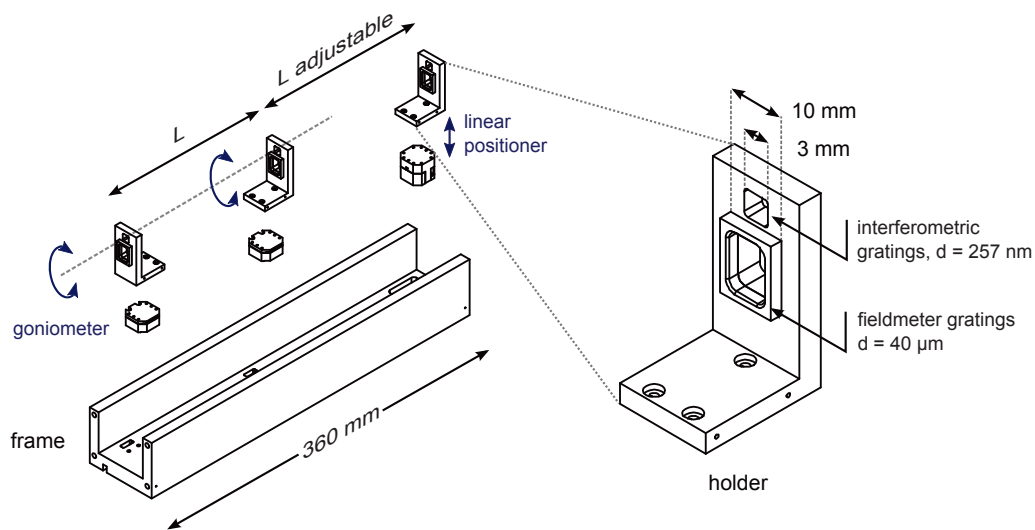
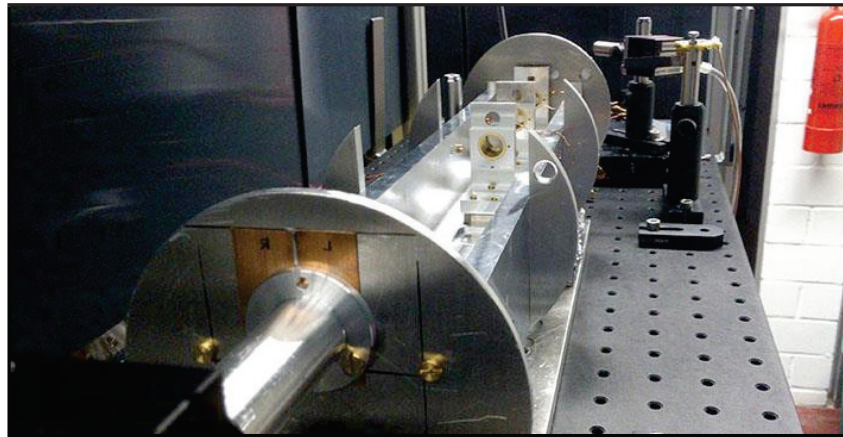


Figure 4.17: Photograph and exploded view of the interferometer. The gratings used for interferometry (pitch $d = 257$ nm) are placed on a holder made of aluminum (right). Gratings having a $40 \mu\text{m}$ periodicity are placed just below to monitor the magnitude of stray electric and magnetic fields. (left) The two first holders are mounted on goniometers allowing rotation around the beam axis, while a translation stage enables the third holder to move vertically. The interferometer is mounted on an aluminum frame, ensuring the mechanical stability of the device and acting as a Faraday cage.

4.4.1 Magnetic shield

In order to keep the surrounding magnetic fields below the critical value $B_c = 160$ mG (see previous chapter), the interferometer and the detector are placed inside a magnetic shield⁶. As shown in figure 4.18, it consists of three cylindrical layers of a metal with high permeability and six caps, ensuring the homogeneity of the field around the edges. The shield is entirely made of mu-metal®, an alloy of nickel (80 %), iron (15 %) and molybdenum (5 %), whose relative permeability reaches typically $\mu = 2.10^4$ [125]. Its efficiency is characterized by the ratio of the magnetic field outside and inside the shield, or shielding factor:

⁶from Magnetic Shield LTD [126].

$$S = \frac{B_{out}}{B_{in}} = 1000. \quad (4.27)$$

Placed in the Earth magnetic field (measured around 0.6 G in the laboratory), the field inside the shield should hence be of the order of 0.6 mG.

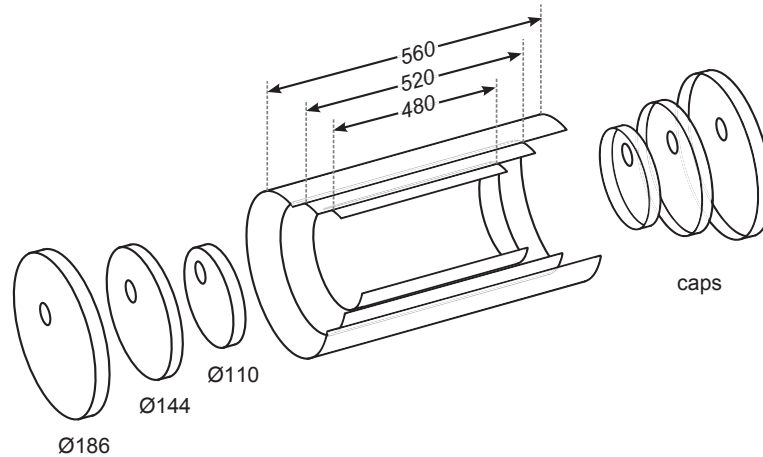


Figure 4.18: Fragmented view of the magnetic shield. It consists of three coaxial cylinders and six caps, ensuring the homogeneity of the field around the edges. The shield, entirely made of mu-metal®, reduces the ambient magnetic field by a factor 1000. All dimensions are in millimeter.

4.4.2 Gratings

Scanning Electron Microscopy (SEM) pictures of a moiré fieldmeter grating and of an interferometer grating are shown in figure 4.19. Their characteristics are listed in table 4.2.

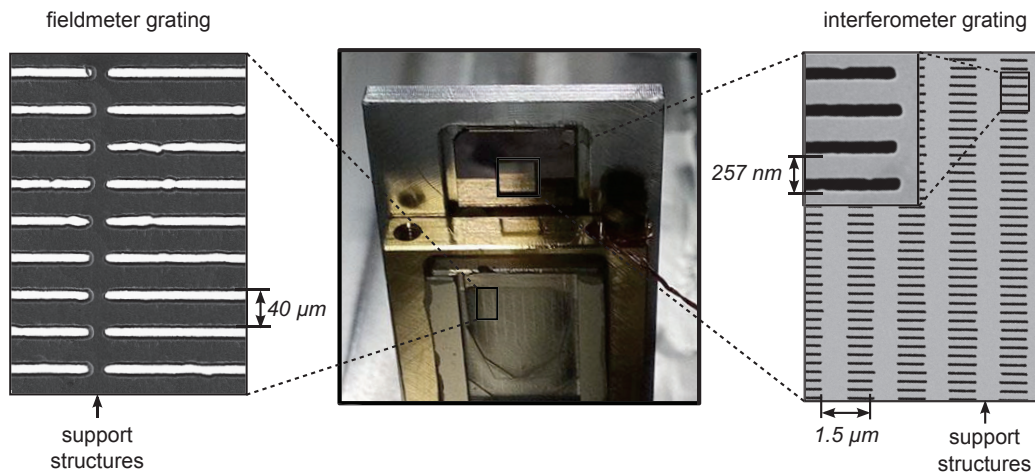


Figure 4.19: SEM pictures of a moiré fieldmeter grating (left) and of an interferometer grating (right). The gratings pitch are respectively 40 µm and 257 nm. On both, support structures are present to avoid the slits to collapse on themselves. (courtesy of L. Veith and A. Kast)

fieldmeter gratings

The gratings of the fieldmeter have a periodicity $d = 40.2 \pm 1.5 \mu\text{m}$ and an open fraction 22.5 % [83]. They were produced out of a silicon wafer on which the pattern was printed by ion etching [84]. Moreover, to avoid the slits to collapse on themselves, support structures were added to the gratings during the etching process. They consist of structures oriented perpendicularly to the slits whose the periodicity ranges from 200 μm to several millimeters depending on each grating [84].

interferometer gratings

The periodicity of the interferometer gratings, evaluated from the high magnification SEM images, is $257.1 \pm 1.8 \text{ nm}$, while their open fractions range from 37 % to 46 % depending on each grating. They are made out of a 160 nm thick membrane of silicon nitride (Si_3N_4). As for the fieldmeter gratings, support structures are also present to ensure the mechanical stability of the slits. They have a periodicity $d' = 1.5 \mu\text{m}$ and an open fraction ranging from 53 % to 71 % depending on each grating. These gratings were graciously offered by Pr. M. Arndt from Vienna University [127].

	fieldmeter gratings	interferometer gratings
size	$10 \times 10 \text{ mm}^2$	$3 \times 3 \text{ mm}^2$
thickness	100 μm	160 nm
material	Si / SiO_2	Si_3N_4
pitch	$40.2 \pm 1.5 \mu\text{m}$	$257.1 \pm 1.8 \text{ nm}$
open fraction	22.5 %	37 %, 40 % and 46 %

Table 4.2: Characteristics of the fieldmeter gratings and of the interferometer gratings.

Coating

As the gratings are made of an insulating material, they are likely to charge-up when hit by the ions. To prevent such a phenomenon, a metallic layer can be deposited on the gratings. For this purpose, we used sputter deposition. This method consists in sending a beam of argon ions onto a metallic target placed on top of the gratings. The atoms of the metal, extracted by the impact of the ions, can then fly and reach the gratings surface. By fixing the time during which the gratings are exposed, the thickness of material deposited can be controlled. The electrical resistivity of several metals are listed in table 4.3.

Material	resistivity ($10^{-8} \Omega \cdot m$)
Silver	1.5
Copper	1.6
Gold	2.4
Aluminum	2.8
Palladium	10.5

Table 4.3: Electrical resistivity of several metals. (from [128])

Figure 4.20 shows SEM images of a membrane of silicon nitride coated with (left) 10 nm of gold only and (right) 10 nm of gold and palladium. As one can see from the pictures, gold

tends to lift off from the silicon nitride membrane. Although it presents an higher resistivity, the alloy of gold and palladium seems instead to adhere better to the membrane. To prevent the coating to lift off, we therefore decided to coat the gratings with a 10 nm layer of gold (80 %) and palladium (20 %).

In order to reduce the mechanical stress during the metalization, the coating was moreover deposited by successive layers of 2 nm, the gratings being flipped between two coatings. Finally, the stability of the coating has been verified under the SEM microscope after one week of irradiation.

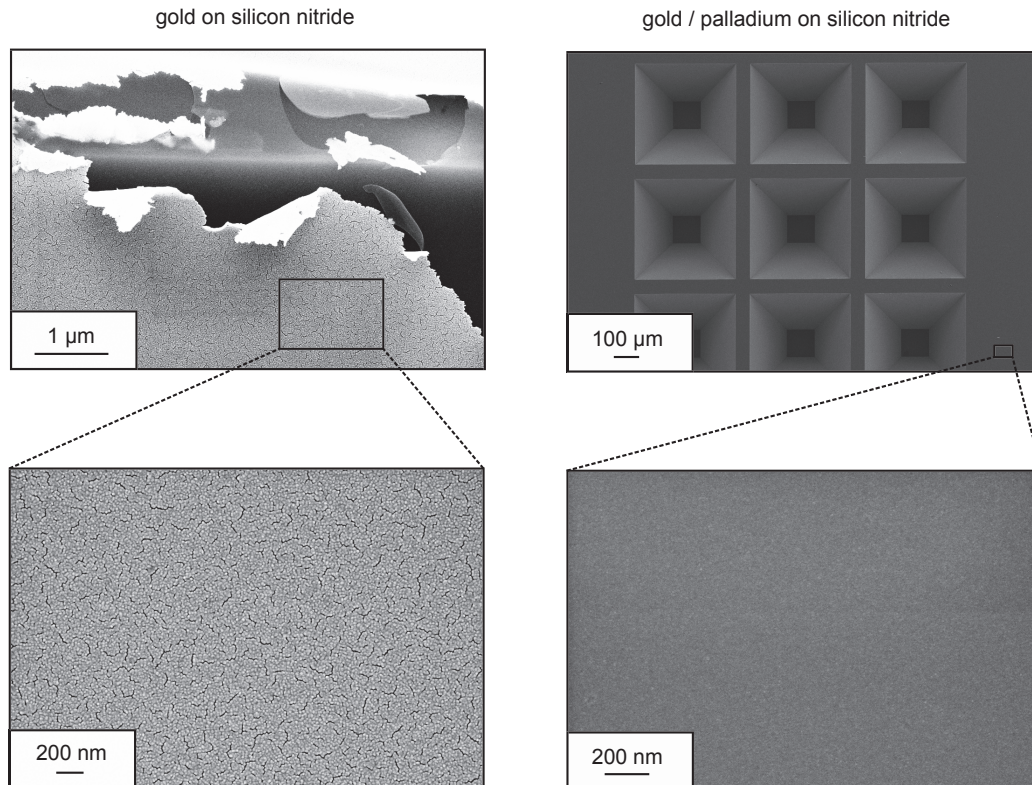


Figure 4.20: SEM images of a silicon nitride membrane coated with (left) 10 nm of gold and (right) 10 nm of gold (80 %) and palladium (20 %). Compared to the gold/palladium alloy, the layer of gold is not adhering to the membrane (delamination visible). For similar magnifications of the SEM, gold shows also larger grains.

The thickness of the coating was chosen arbitrarily: evaluated with SRIM software [129], 10 nm is indeed the range of a 2 keV beam of protons in gold.

Defects

To check the conformance of the gratings, one grating from the interferometer was exposed to the SEM. Figure 4.21 shows the defects that were observed. The top pictures show a crack and perforation of the grating, probably due to a mishandling. The bottom left picture shows instead a defect resulting from the patterning process itself. Nevertheless, we emphasize that these defects are rare and represent a negligible fraction of the grating surface. They should not disturb the interferometer.

The dust, visible on the bottom right picture, could instead get charged up by the ions. The inhomogeneous field hence created may disturb the pattern. We will see in the next chapter that the electric field is fortunately too small to affect the interferometer.

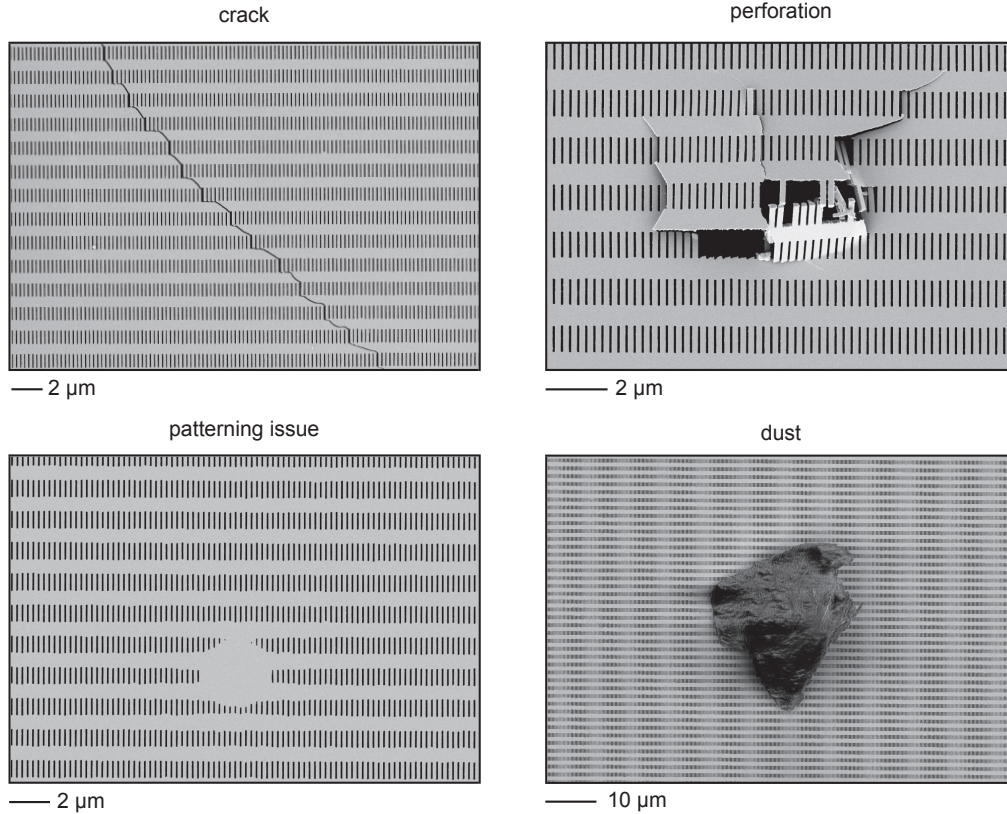


Figure 4.21: SEM picture of a few defects seen on a interferometer grating. The top pictures show a crack and perforation of the grating, probably due to a mishandling. The bottom left picture shows instead a defect resulting from the patterning process itself.

4.4.3 Alignment

The positioning of the gratings with respect to each other is a crucial point to operate the interferometer. To align the interferometer, we present now a method that uses the diffraction pattern of a He-Ne laser on the grating support structures.

Tolerance

To quantify the maximal angle allowed between the gratings, one can calculate for instance what angle would cause the appearance of an additional macroscopic fringe.

As seen in figure 4.22, the periodicity of the macroscopic fringes D depends on the relative angle between each grating. It can be expressed as a function of the angle α between the gratings and the grating periodicity: D/α . The number of fringes n formed upstream of the third grating is thus the width of the grating divided by the periodicity of the macroscopic fringes.

$$n = \frac{l}{D} = \frac{l \cdot \alpha}{d}. \quad (4.28)$$

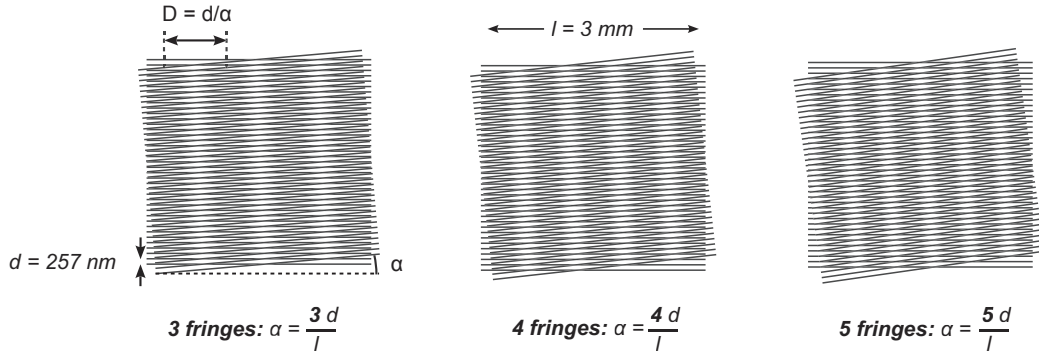


Figure 4.22: The number of macroscopic fringes formed upstream of the interferometer depends on the relative angle between each gratings. To fix the number of fringes, the gratings have to be aligned at better than $\alpha \leq \frac{d}{l}$.

The number of macroscopic fringes formed upstream of the interferometer is hence fixed if the relative angle between the gratings fulfills:

$$\alpha \leq \frac{d}{l}. \quad (4.29)$$

For $d = 257 \text{ nm}$ and $l = 3 \text{ mm}$ (see table 4.2), it corresponds to a maximal angle of $85 \mu\text{rad}$ (or 4.87 mdeg) between the gratings.

Alignment procedure and precision reached

The procedure to align the interferometer is described schematically in figure 4.23. A He-Ne laser ($\lambda = 633 \text{ nm}$) is sent through the interferometer and diffracts with the support structures of each gratings (pitch $d = 1.5 \mu\text{m}$, see table 4.2). One can show that the laser beam is split in only two orders of diffraction, at angles $\theta_1 = 24.9 \text{ deg}$ and $\theta_2 = 57.5 \text{ deg}$. In order to align the second grating with respect to the third one (which cannot be rotated), a camera⁷ is placed at the intersection of the second order of the third grating and the first order of the second grating. As shown on the close-up view, the second grating is then rotated until the two orders fully overlap. To align the first grating with respect to the third one, the same procedure is repeated with the second grating in place.

The precision of the alignment depends on

- the distance between the intersection point and the axis of the interferometer ($l = 113 \text{ mm}$ for the second grating),
- the minimal distance that can be resolved between the two orders of diffraction (measured typically with a precision of $\Delta x \simeq 1.5 \mu\text{m}$).

The accuracy on the relative angle between the gratings is therefore:

⁷Guppy F-033 from Allied Vision [130]

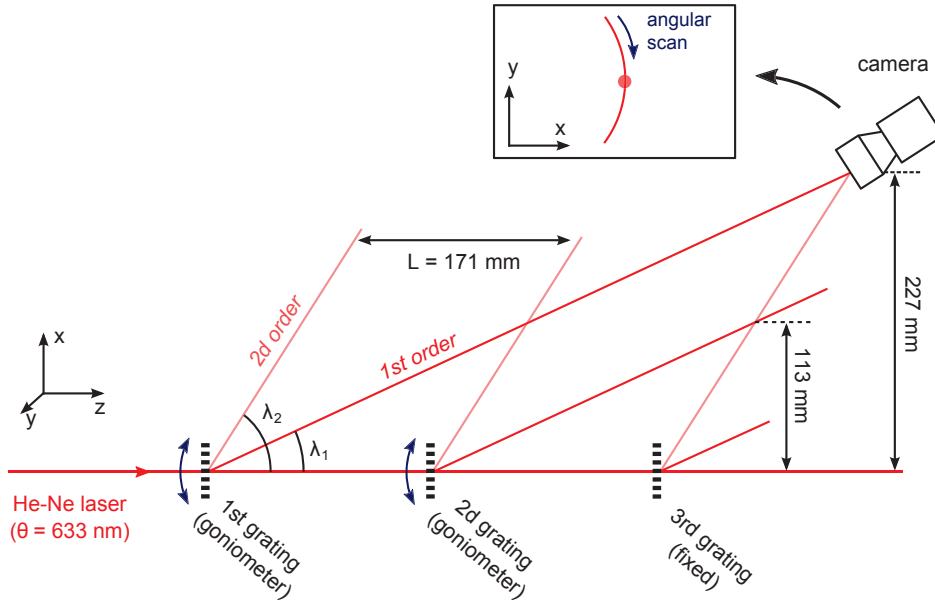


Figure 4.23: The procedure to align the interferometer (seen from the top). A He-Ne laser beam (wavelength $\lambda = 633$ nm) sent through the interferometer is diffracted on the grating support structures (periodicity $d = 1.5$ μm). To align the second grating with respect to the third one (fixed), a CCD camera is placed at the intersection point of the second order of the third grating and the first order of the second grating. The second grating is then rotated until the two orders fully overlap (close-up view). The same procedure is repeated to align the first grating with respect to the third one.

$$\alpha = \frac{\Delta x}{l}, \quad (4.30)$$

$$\alpha = 13 \mu\text{rad}.$$

Since equation (4.29) is satisfied, we can state that the interferometer is aligned.

A limitation of this protocol is that, once aligned, the interferometer has to be moved inside the magnetic shield. Due to the possible movement of the goniometers during this operation, there is no reason to believe that the gratings are still aligned afterward. In the future, a major upgrade will be to monitor the positions of each grating inside the chamber, while the interferometer is acquiring data. The method, which will rely on three independent optical interferometers, is detailed in reference [131].

4.5 Detector

The ion fringes formed upstream of both the interferometer and of the fieldmeter are observed on the imaging detector. In our setup, an amplification of the signal is first performed by a two-stage microchannel plate (MCP). The amplified signal is then read out by either a resistive anode, or a phosphor screen and a CMOS camera. After having introduced the MCP specifications, we compare the performance of both readouts.

4.5.1 Microchannel plate

Microchannel plates are widely used components in particle and atomic physics. They consist of plane of highly resistive material (usually silicon oxide) metalized on each face. An array of channels leading from one face to the opposite is distributed over the whole surface, each channel acting as an electron multiplier. When a particle hits the surface of a channel, secondary electrons are emitted. If a voltage difference is applied between the two faces of the MCP, these electrons can in turn emit other electrons such that for one single impact, the number of electrons exiting the MCP (or gain) reaches typically 10^4 . The MCP used in our setup has an active diameter of 25 mm and the distance between each channel (10 μm in diameter) is of 12 μm . As it is actually made of two MCPs stacked together in a chevron configuration, it provides a typical gain around $5 \cdot 10^6$ for a 2 kV voltage difference [133].

The MCP is sensitive to charged particles delivered by the ion source, such as protons, H_2^+ , H_3^+ and hydrogen atoms. The detection efficiency of these particles are given in figure 4.24. Note that ultra-violet or X-rays photons can be detected as well with a detection efficiency ranging from 1 % to 15 % [72].

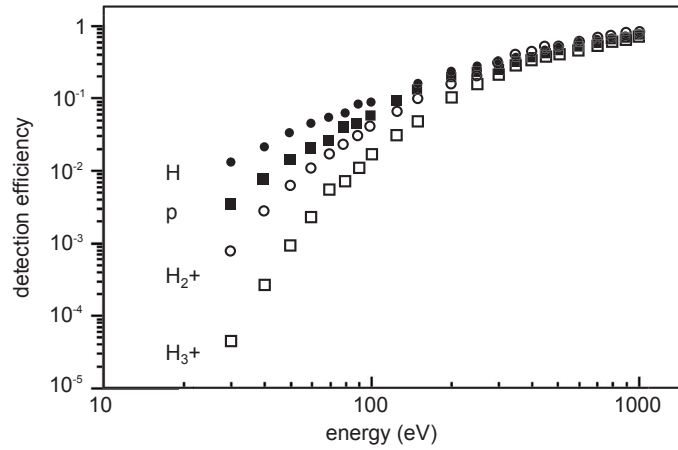


Figure 4.24: MCP detection efficiency of hydrogen (H), protons (p), H_2^+ , and H_3^+ ions depending on their kinetic energy (from reference [132]).

The amplified electrons emerging from the rear face of the MCP can then be viewed either on a phosphor screen, or indirectly by encoding of the charge pulses on a resistive anode.

4.5.2 Resistive anode

In many instances a pulse-counting mode of operation is desired (as when, for example, simultaneous measurement of timing and position is performed). The resistive anode is a good candidate for this purpose. The resistive anode can be seen as a planar RC transmission line on which the impinging charges are collected by four electrodes A, B, C, D . The x and y positions of each particle impact can be determined from the partitioning of the charges Q_i :

$$x = \frac{Q_A + Q_B - Q_C - Q_D}{Q_A + Q_B + Q_C + Q_D}, \quad (4.31)$$

and

$$y = \frac{Q_A + Q_D - Q_C - Q_B}{Q_A + Q_B + Q_C + Q_D}. \quad (4.32)$$

A fast electronics⁸ converts then the analog signals to a set of digital coordinates, stored in a 256×256 pixel matrix. The spatial resolution of this model is of the order of $250 \mu\text{m}$ with typical background count rate of less than 10 per second [134]. The resistive anode offers on the other hand good timing capabilities: the model used here is for instance able to detect up to 10^5 counts per second.

The resistive anode and the two MCPs are monitored by one single voltage V_0 . By the mean of a resistive divider, the voltage of the resistive anode is reduced to $0.86V_0$, while the front plate of the MCP is electrically grounded. The rear plate of the second MCP is at $0.75V_0$ [134]. The evolution of the flux as a function of the voltage V_0 is plotted in figure 4.25 for protons and background (residual neutral particles, dark counts and thermal noise). As seen in figure 4.25, the signal-to-noise ratio evolves also with the gain and reaches a maximum value of $\sim 2 \cdot 10^3$ for an anode voltage of $V_0 = 2.7 \text{ kV}$.

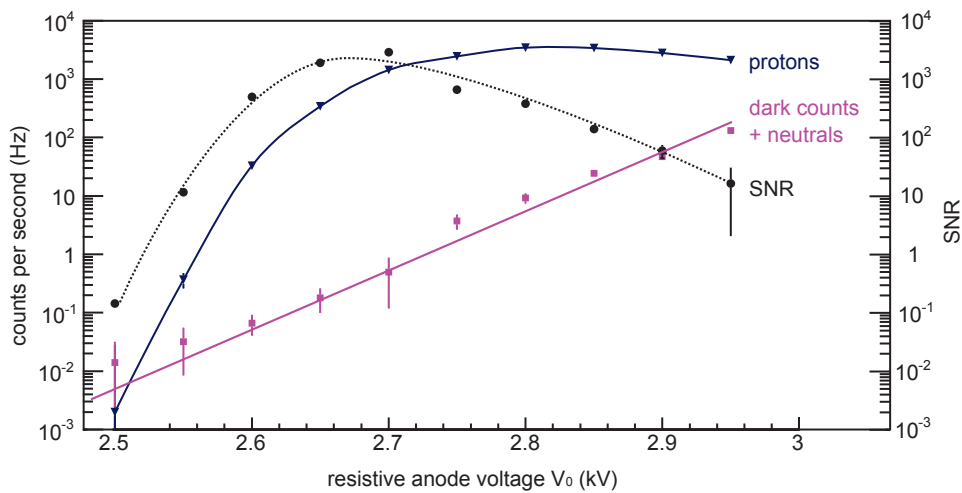


Figure 4.25: The rate of events detected on the resistive anode as a function of the resistive anode voltage. The rate of neutrals and dark counts are summed as they represent a source of background (pink). The signal-to-noise ratio (SNR, black dotted line), defined as the ratio of the blue (protons) and pink curve reaches a maximum value of $\sim 2 \cdot 10^3$ for an anode voltage of $V_0 = 2.7 \text{ kV}$.

For each ions species considered, the images are acquired with a rate of approximately 1 kHz during 1 min such than 10^4 to 10^5 events are taken into account in average. To minimize the effect of the non-uniformity of the detector (dead and hot stripes), the resistive anode is rotated with respect to the expected fringes orientation. Figure 4.26 shows a typical image of the moiré fringes as viewed on the resistive anode, obtained with neutral hydrogen.

4.5.3 Phosphor screen and camera

Although resistive anodes are advantageous for pulse counting applications or time-of-flight measurements, better spatial resolution can be achieved with phosphor screens. A schematic view of the MCP readout by a phosphor screen and a camera is shown in figure 4.27. The MCP and phosphor screen, placed inside the vacuum chamber, are separated from the camera by a glass window. The signal originating from a single proton is first amplified into 10^6 electrons by the MCP. A phosphor screen converts then the electrons into photons, emitted

⁸Quantar Technology 3390A Resistive Anode Encoder [134]

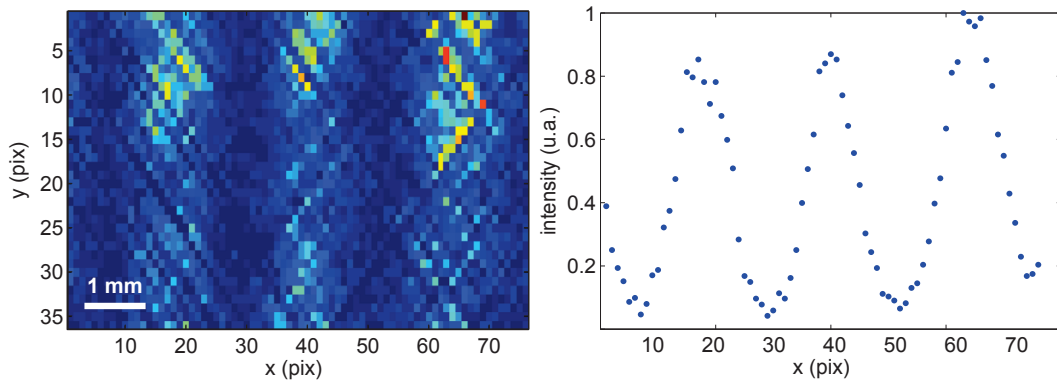


Figure 4.26: View of the moiré fringes obtained with neutral hydrogen on the resistive anode detector. The plot on the right represents the projection on the x axis with a high visibility of 0.92. In the fieldmeter, such a pattern is used as a reference for measuring the shift difference between the ions.

in all directions (covering therefore a solid angle of 4π). Only a small fraction of the photons, $\Omega = 0.06$ sr, is collected by the camera lens (diameter 42 mm at a distance of 150 mm from the phosphor screen) and read by a CMOS camera.

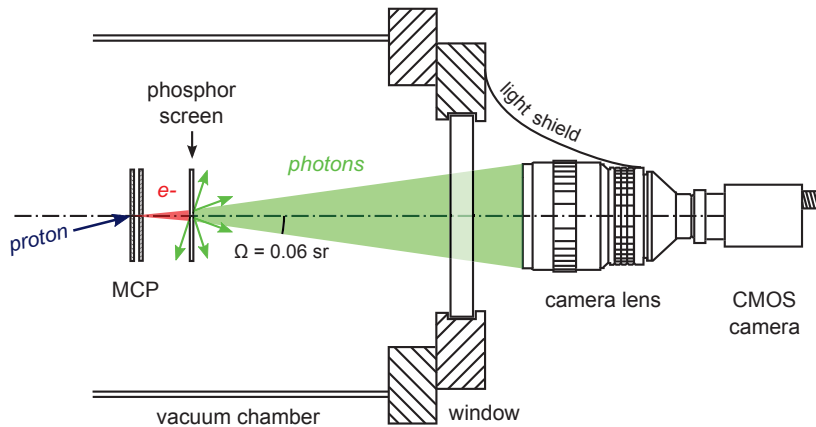


Figure 4.27: Schematic view of the MCP stacked to a phosphor screen and read out by a CMOS camera. The MCP and phosphor screen, placed inside the vacuum chamber, are separated from the camera by a glass window. The signal originating from a single proton is first amplified into 10^6 electrons by the MCP and sent onto a phosphor screen. Introducing Ω the solid angle covered by the objective, a small fraction $\Omega/4\pi$ of the photons emitted by the phosphor screen is then collected by the objective and read by a CMOS camera.

The detector presented here is very similar to the one used in the hydrogen detector, already introduced in section 2.3.4. After having detailed the phosphor screen and the camera, we evaluate the detection efficiency and the spatial resolution of this detector.

Phosphor screen

The phosphor screen consists of a thin layer ($\sim 6 \mu\text{m}$) of a fluorescing material deposited onto a glass substrate. When the electron cloud impacts on the screen, the energy absorbed is re-emitted isotropically under visible light (green). To avoid the surface to charge up, a thin layer

of a conductive material (indium tin oxide) is also deposited on top of the phosphor [133]. Depending on their conversion efficiency and decay time, various types of phosphor screens are available. The characteristics of the one used in our setup (type P43) are listed in table 4.4. Although its long decay time makes it inappropriate for time-of-flight measurements, the P43 has a high conversion efficiency, of the order of 100 photons/ e^- for 4 keV impinging electrons.

Phosphor screen	
composition	Gd ₂ O ₂ S:Tb
conversion efficiency	100 photons/ e^-
peak wavelength	545 nm (green)
decay time	2.6 ms

Table 4.4: Characteristics of the P43 phosphor screen (from GIDS-GmbH [133]). The conversion efficiency of the phosphor screen is taken from reference [135], extrapolated for 4 keV electrons. The decay time written here is the time needed for the light output to decrease from 90 % to 1 %.

CMOS camera

Once collected by the camera lens, the photons arrive to the CMOS camera. Some of the relevant specifications of the camera and of its sensor are given in table 4.5. The high quantum efficiency of the sensor, $QE = 67\%$ at the peak wavelength of the phosphor screen, is noticeable.

CMOS Camera		Optical Sensor	
model	Mako G-234	model	SONY IMX249
bit depth	8, monochrome	sensitive size	11.3 × 7.1 mm
resolution	1936 × 1216 pixels	dark current	7 e^- /pixel
maximal gain	40 dB	pixel size	5.86 × 5.86 μm^2
frame rate (freerun)	up to 30 fps	Quantum Efficiency	65% at 545 nm
exposure time (trigger)	65 μs to 73 s	Full Well Capacity	33 105 e^-

Table 4.5: Specifications of the Mako G-234 camera and its optical sensor (from [130]).

The number of photons to saturate each pixel is calculated as $N = FWC/QE$, in which FWC (Full Well Capacity) is the amount of charge an individual pixel can hold before saturating, and QE is the quantum efficiency at 545 nm. 55000 photons are needed to saturate each pixel.

Independently from the hot pixels, every image presents a certain level of noise. It can originate for instance from dark current or from an imperfect shielding of the surrounding light. An image of the noise (where no signal is expected) is shown on figure 4.28 for a MCP voltage of 1.5 kV and the phosphor screen at 4.0 kV. The intensity of the pixels of the image are represented as an histogram on the upper panel. As seen from the histogram, the noise observed on the image peaks at an intensity $z = 14.8 \pm 2.1$ in average. It corresponds to $(15/256) * FWC = 1940$ photo-electrons.

For an optimal visualization of the signal, the field-of-view of the camera is adjusted to the zone where the fringes appear. It defines the conversion scale:

$$1 \text{ pixel} \longleftrightarrow 12.5 \mu\text{m} \quad (4.33)$$

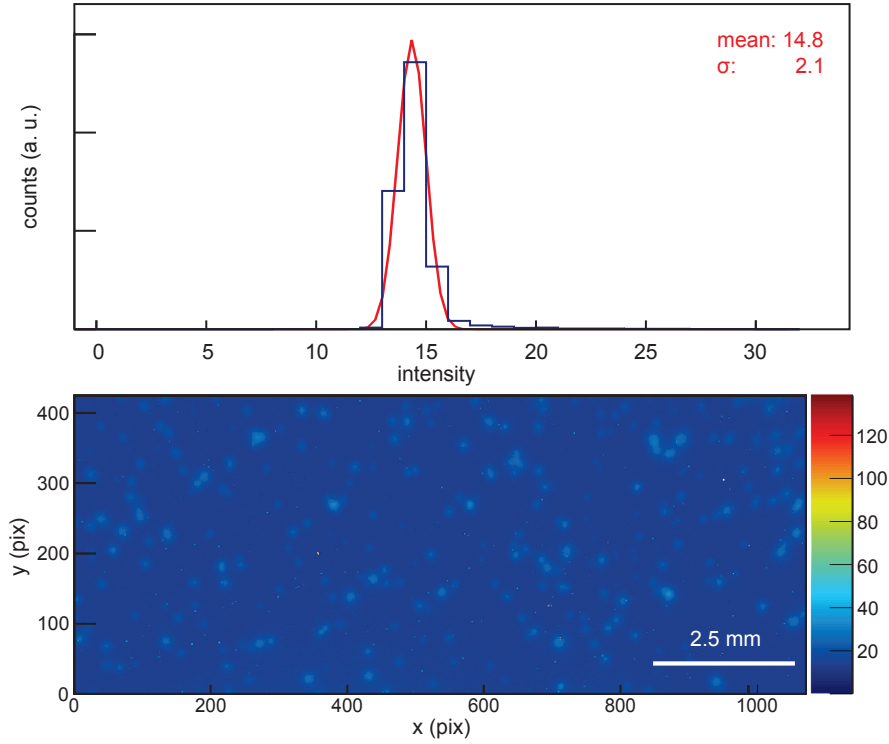


Figure 4.28: Image of the noise (taken in a zone where no signal was expected) as seen by the CMOS camera. The MCP was set at 1.5 kV and the phosphor screen at 4.0 kV. The image is encoded on 8 bits, corresponding to $2^8 = 256$ levels for the intensity of each pixel (color scale). The intensity of the pixels are represented as an histogram (upper panel), which peaks at an average value of 14.8 ± 2.1 .

4.5.4 Efficiency

Is the detector sensitive to single particle? To answer this question, we evaluate now the intensity expected on the image starting from the impact of a unique particle. The efficiencies of the different parts of the detector are given in table 4.6.

module	type	efficiency
MCP	gain (at 2 kV)	$5 \cdot 10^6$
phosphor screen	conversion efficiency	100 photons/ e^-
objective	light collection	0.48 %
optical sensor	quantum efficiency	65 %
Total Gain		$1.6 \cdot 10^6 e^- / \text{incident p}$

Table 4.6: Detection efficiencies of the different modules of the detector. A single proton leads to $1.6 \cdot 10^6$ photo-electrons on the sensor. The light collection of the objective is calculated as the solid angle covered by the lens divided by 4π since the photons are emitted in all directions.

A single proton impact leads therefore to $1.6 \cdot 10^6$ photo-electrons on the camera sensor. According to reference [136], the electron cloud at the exit of the second MCP expands typically over 6.5×6.5 channels, which corresponds roughly to an area of $120 \times 120 \mu\text{m}^2$ (see section

4.5.1) on the phosphor screen. As one pixel on the camera corresponds to $12.5 \mu\text{m}$, the $1.2 \cdot 10^6$ electrons are hence distributed on a 10×10 pixel matrix such that each pixel receives in average ~ 16000 electrons. With a noise level of 1940 electrons calculated above, it corresponds to a signal-to-noise ratio around 8.

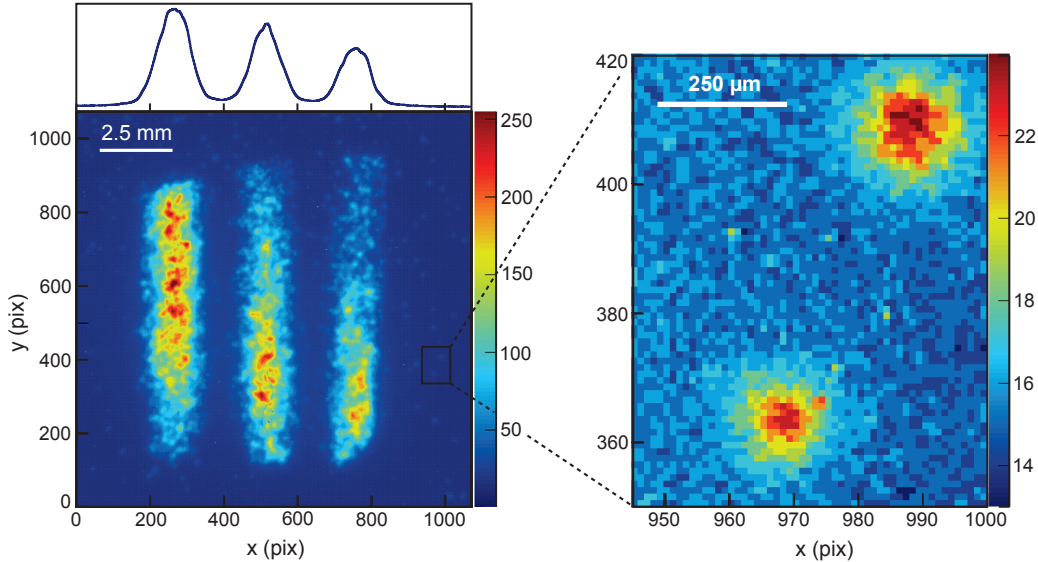


Figure 4.29: (left) Image of the moiré fringes obtained with protons, as seen by the CMOS camera. The MCP was set at 1.5 kV and the phosphor screen at 4.0 kV. The upper plot is the projection of the fringe pattern on the x axis (visibility $\nu = 0.7$). (right) Close-up image of single protons impact. As the spot expands over several pixels, with a proper algorithm, one can reconstruct the center of the spot with a sub-pixel resolution.

The moiré fringes obtained with 2 keV protons are shown on figure 4.29. A zone where two single proton impacts are visible is enlarged on the right. Moreover, the intensity at the position of the impact is of the order of 4, such that the signal-to-noise ratio is around $24/15 \simeq 1.6$, lower than the one calculated. The reason is that the MCP voltage was set to 1.5 kV for this measurement, corresponding to a gain around 10^6 [72]. A signal-to-noise ratio reduced by a factor 5 is therefore expected.

4.5.5 Spatial resolution

We have seen that the spatial resolution of the resistive anode depends on the size of the strips, and reaches typically $250 \mu\text{m}$. The resolution of a phosphor screen readout is instead ultimately limited by the size of the phosphor grains, which are in comparison of the order of 2 to $3 \mu\text{m}$ [133]. Based on the data acquired with neutral hydrogen, we evaluate now experimentally the spatial resolution of the detector. We will see that in the regime where particles arrive one by one on the MCP, the spatial resolution of the readout is typically of the order of $\sigma = 14 \mu\text{m}$.

Retrieving the impacts coordinates

We have seen in the previous section that the camera is able to detect single proton impact. The approach chosen is to reduce the flux and the shutter time of the camera until the particles

are detected one by one. In that case, one can retrieve particle per particle the coordinates of the impact on the detector. As seen on figure 4.29 (right), the impact of a proton extends over several pixels on the camera. This feature makes the resolution drastically higher than for the resistive anode, where a particle illuminates only one pixel.

The algorithm used to extract the coordinates of each impact is illustrated on figure 4.30. It proceeds as follows:

- Pixels whose the intensity are below a certain threshold are suppressed from the image. The value of the threshold is set to $\langle z \rangle + 3 \cdot \sigma_z$, where $\langle z \rangle$ is the average intensity of the noise, measured in section 4.5.3 and σ_z the standard deviation of the noise intensity. For normally distributed noise, this steps suppresses 99.7 % of the background.
- The local maxima are searched for in the background-free image. In order to remove the hot pixels, only the pixels whose the 8×8 neighboring pixels have an intensity above the threshold are taken into account. If two maxima are separated by less than the threshold, only the highest one is retained.
- For each local maximum, the background-free image is projected on the x and y axes.
- The projection on the x axis (respectively y axis) is then fitted by a gaussian distribution. The x (resp. y) coordinate of the impact is identified to the mean value extracted from the fit.

With such an algorithm, the accuracy on the position of the impact gets better than the size of a pixel. From the analysis of $5 \cdot 10^5$ impacts, the error on the coordinates (from the fit) is distributed around a mean value of 0.05 pixel (0.63 μm).

Pattern formed upstream of a single grating

Once retrieved by the algorithm, the impact coordinates of each hit are stored in an histogram and form the fringe pattern. Figure 4.31 shows for instance the pattern formed upstream of one grating (pitch $d = 40 \mu\text{m}$) exposed to approximately 10^5 particles.

While the fringe visibility of a detector having an infinite resolution would be 1 (either the particle passes through the slit or is blocked by the gratings material), the visibility is here of the order of 0.1 due to the uncertainty on each impact coordinates. The pattern can hence be seen as the convolution of a rectangle function, accounting for the grating transmission function, with a gaussian distribution, whose the standard deviation accounts for the detector resolution. The deconvolution of the pattern leads to a standard deviation of

$$\sigma = 14.2 \pm 1.0 \mu\text{m}. \quad (4.34)$$

This number accounts for the detector intrinsic spatial resolution but also for the strength of the algorithm. It is important to notice that the spatial resolution found does not represent an ultimate limit. One could indeed discuss the hypotheses of the algorithm (gaussian shape of the impact, noise subtraction) and find another method to extract the coordinates with a better accuracy.

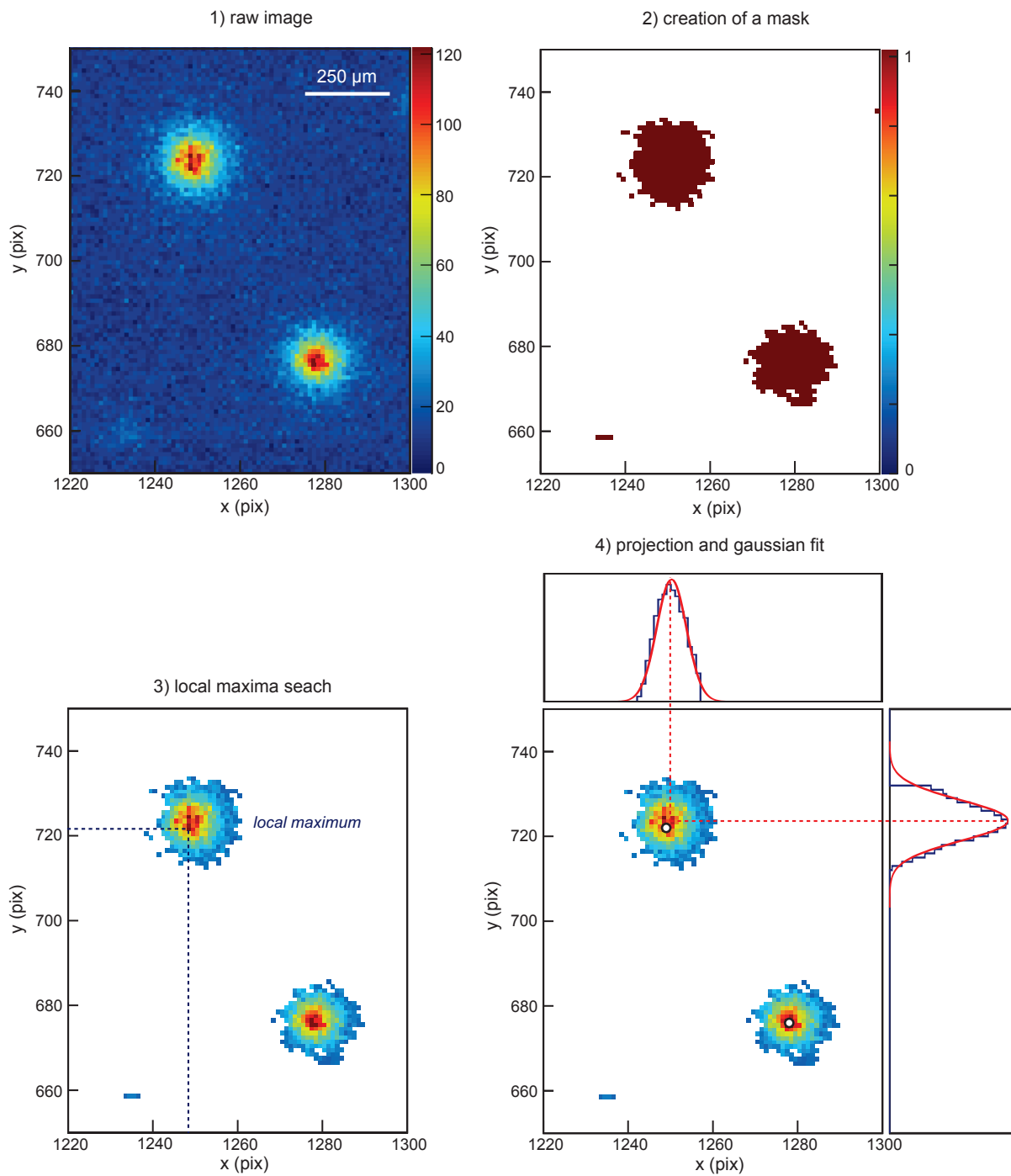


Figure 4.30: The algorithm used to extract the impact coordinates with a sub-pixel resolution. A mask is created from the raw image (image 1). If the intensity of a pixel is below a certain threshold, its intensity is set to zero. The threshold is chosen to exclude 99.7 % of the background (see text). The local maxima of the background-free image (3) are searched in a second time. The background-free image is then projected on the x and y axes. The x and y coordinates of each maxima are finally retrieved by fitting the projection with a gaussian distribution.

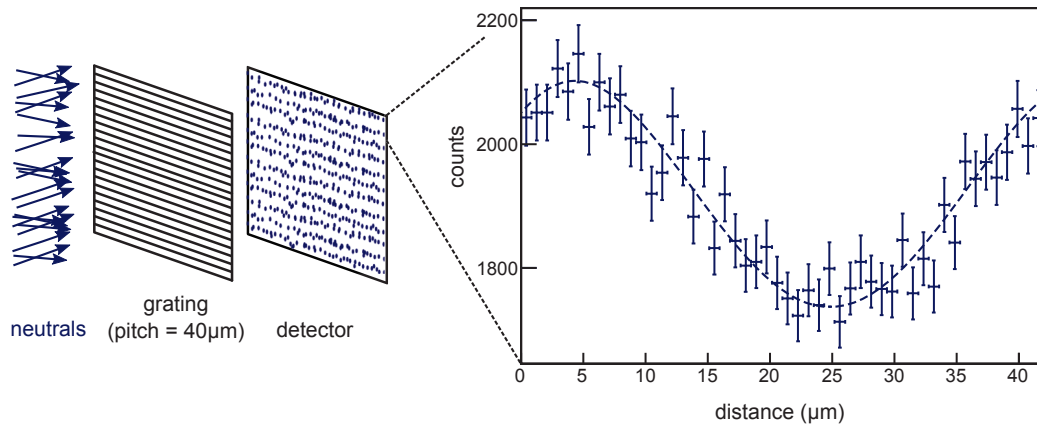


Figure 4.31: The pattern formed by 10^5 impinging hydrogen atoms passing through a single grating (pitch $d = 40 \mu\text{m}$). The coordinates of the impacts are retrieved from the algorithm presented above. While the fringe visibility of a detector having an infinite resolution would be 1 (the particles are either stopped or pass through the grating slit), the visibility is here of the order of 0.1.

4.6 Summary

To perform for the first time the interferometry of protons, a dedicated experimental setup has been designed and built. Its first stage consists of an ECR source delivering protons along with H_2^+ and H_3^+ ions at an energy ranging from 400 eV to 2000 eV. The energy spread of the ions, of the order of 1.3 %, has been measured by varying the voltage of a mesh placed in front of a Faraday cup. The beam size, adjusted by an electrostatic lens, has been estimated between 3.23 mm and 3.89 mm. A Wien filter has been installed and calibrated to select in a controlled way each ion species. The interferometer consists of three gratings having a pitch of 257 nm placed inside a magnetic shield. The shield, made of three layers of mu-metal, is able to reduce the Earth magnetic field by a factor 2000. Each grating is mounted on a vacuum compatible actuator allowing either rotation of the grating around the beam axis or its vertical translation. The interferometer was aligned beforehand with a precision of $13 \mu\text{rad}$ on the relative angle between the gratings. To monitor the magnitude of the electric and magnetic fields within the magnetic shield, we have installed a moiré fieldmeter right under the interferometer. The fieldmeter consists of three gratings having a pitch of $40 \mu\text{m}$ and separated by a distance that can be adjusted. Moreover, to reference the moiré fieldmeter, we have realized a neutralization chamber. When operated at an optimal pressure of 10^{-2} mbar, the chamber provides a beam of neutral hydrogen formed by charge-exchange between the protons and a nitrogen gaseous target. When the particles exit the interferometer, their signal, firstly amplified by a MCP, is finally read-out by a detector. We have compared in this chapter the performance of two types of readout: a resistive anode and a phosphor screen associated with a CMOS camera. Although the resistive anode is better for experiments dealing with pulse counting or time-of-flight measurements, the phosphor screen offers drastically better imaging capabilities. It is moreover sensitive to single particles and in the regime where particles are observed one by one, we have developed an algorithm to retrieve the impact coordinates with sub-pixel accuracy. With such an algorithm, the spatial resolution of the detector reaches $14 \mu\text{m}$.

5 | Field Measurements and Discussion

We have seen in chapter 4 that the PIXIE experiment deals with an interferometer and a moiré fieldmeter running in parallel. We present in this chapter the results of the moiré fieldmeter. In order to measure the fields acting at the position of the interferometer, we acquire the fringe patterns formed by protons, H_2^+ and H_3^+ ions on the resistive anode detector. The respective shifts between these patterns and a reference pattern (formed by hydrogen atoms) are then measured to evaluate the magnetic and electric fields as detailed in section 3.2.2. In a second phase, the reliability of the fieldmeter is evaluated by the mean of a pair of coils creating an homogeneous and known magnetic field. The output of the moiré fieldmeter is then compared with the response of a Hall probe, a magnetic sensor commonly used. The fields measured nearby the interferometer are then taken into account to reevaluate the visibility of the interferometric fringes (see section 3.3.3). The last part of the chapter stresses the importance of controlling the electric field due to the charge-up of the interferometer. To illustrate the charge-up effects, a wire made of an insulating material was placed close to the fieldmeter. We show how the inhomogeneous field created by that wire distorts the moiré pattern. The results presented here have been recently published in an article [86].

5.1 Field measurements

5.1.1 Fields acting in the interferometer volume

The moiré patterns of hydrogen, protons, H_2^+ and H_3^+ ions measured by the fieldmeter are plotted in figure 5.1. Each pattern is formed by around 10^4 ions at an energy of 2000 eV and projected along the axis of the fringes. The distance between the gratings is set to 171 mm (long configuration) and the detector is the resistive anode presented in section 4.5.2. The visibility of the fringes is comprised between 99 % for the neutral particles and 97 % for the protons.

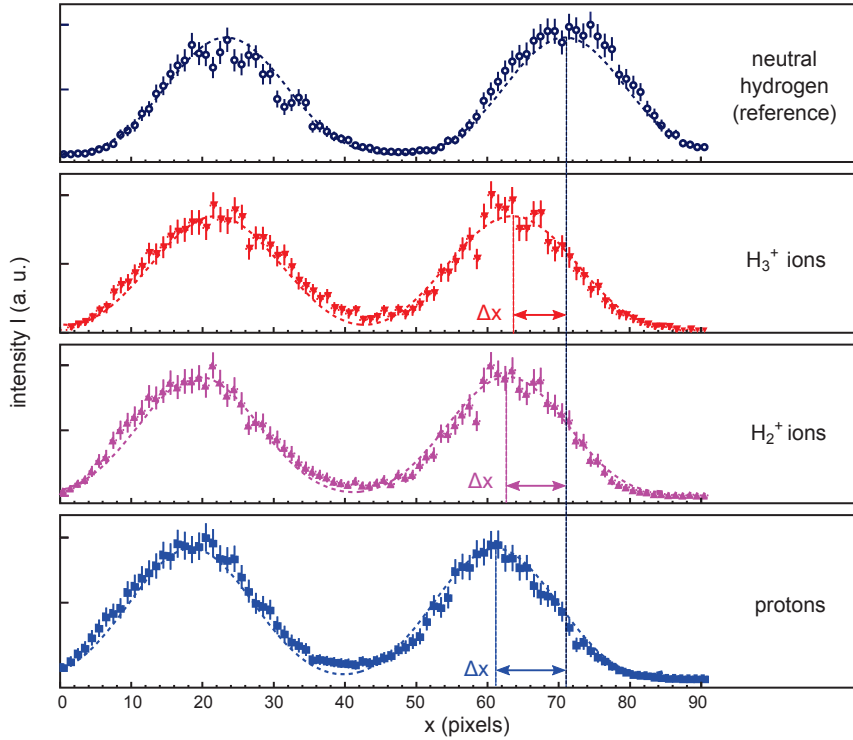


Figure 5.1: Projection of the moiré patterns of hydrogen, H_3^+ , H_2^+ ions and protons. Each pattern is formed by around 10^4 ions impinging on the resistive anode detector, at an energy of 2000 eV. The patterns are then fitted by their analytical expression (equation (3.4)) to retrieve the shifts between the ions and the hydrogen reference. Original figure published in [86].

In order to retrieve the shift between the pattern of ions and the pattern of hydrogen, the fringes are fitted by their analytical expression (see section (3.1.2)). As the Fourier coefficients are rapidly negligible for $n > 2$, only the first three coefficients are taken into account for the fit:

$$I(x) = \frac{a_0}{2} + a_1 \cos\left(\frac{2\pi}{D}(x + \Delta x)\right) + a_2 \cos\left(\frac{4\pi}{D}(x + \Delta x)\right), \quad (5.1)$$

where the a_n coefficients are given by:

$$a_n = 4\eta^3 \text{sinc}^3(\pi\eta n) \cos(\pi\eta n), \quad \forall n \in \mathbb{N}. \quad (5.2)$$

The corresponding shifts, scaled down to the original $40\ \mu\text{m}$ periodicity of the gratings, are listed in table 5.1. The fit uncertainties originate from the non-uniformity of the detector and from the error on the pattern periodicity ($2.3\ \mu\text{m}$).

	shift (μm)	error (μm)	χ^2/ndf
protons	1.98	0.37	1.32
H_2^+	1.35	0.26	1.35
H_3^+	1.14	0.23	1.20

Table 5.1: The shifts Δy measured between H_3^+ , H_2^+ and protons with hydrogen.

Each combinations of ion species (proton with H_2^+ , proton with H_3^+ and H_2^+ with H_3^+) leads to three distinct measurements for the electric and magnetic fields following the equation system (3.12). Taking the mean value of the three combinations leads to:

$$\begin{aligned} E_y &= 0.91 \pm 0.31\ \text{V.m}^{-1} \\ B_x &= -15.2 \pm 6.8\ \text{mG}, \end{aligned} \quad (5.3)$$

where the errors originate from the standard deviation of the different combinations. It is worth noticing that both electric and magnetic fields are measured below the critical fields that might disturb the interferometer ($E_c = 4.8\ \text{V.m}^{-1}$, $B_c = 230\ \text{mG}$, see table 3.4).

5.1.2 Comparison with a known magnetic field

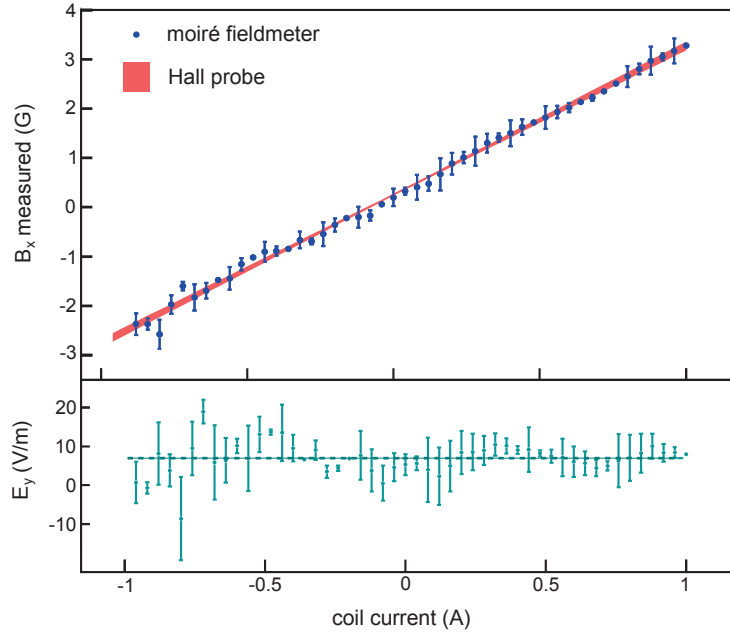


Figure 5.2: Measured electric and magnetic fields as a function of the coil current. The magnetic field, evaluated separately by a Hall probe, shows a linear dependency while the electric field remains constant of the order of $6.96\ \text{V.m}^{-1}$. On the upper plot, an offset field of $410\ \text{mG}$ (imputed to the improper nulling of the Hall sensor) is added to the Hall probe response. Published in [86].

The reliability of the fieldmeter was evaluated with an homogeneous and known magnetic field. For this purpose, the three gratings were taken out of the mu-metal shield and placed between two large rectangular Helmholtz coils (dimensions 500×280 mm), ensuring a uniform magnetic field¹ between the gratings. As the distance between the gratings was set to $L = 34$ mm to guarantee the magnetic field homogeneity, the minimal field measurable by the fieldmeter was $2.4 \text{ mG}\cdot\text{Hz}^{-1/2}$. For each value of the current, the field values were obtained as in the previous section. The magnetic field was independently measured with a Hall probe placed in the vicinity of the gratings.

The magnetic and electric fields measured by the moiré fieldmeter as a function of the coil current are given in figure 5.2. An affine function with a slope of 2.97 G/A is fitted to the data and compared to the Hall probe output ($3.01 \pm 0.07 \text{ G/A}$). Although the slopes are compatible, a 410 mG offset is measured between the two devices. This offset is imputed to the improper nulling of the Hall sensor, while the moiré is calibrated “in absolute” by the hydrogen reference at the position of interest (in situ).

5.1.3 Expected visibility of the interferometric fringes

As presented in section 3.2.4, the presence of stray fields reduces the visibility of the interferometric fringes. The interferometric fringe visibility as a function of the proton energy is displayed in figure 5.3. The visibility is calculated for a 1 % energy spread and takes into account the fields measured in section 5.1.1.

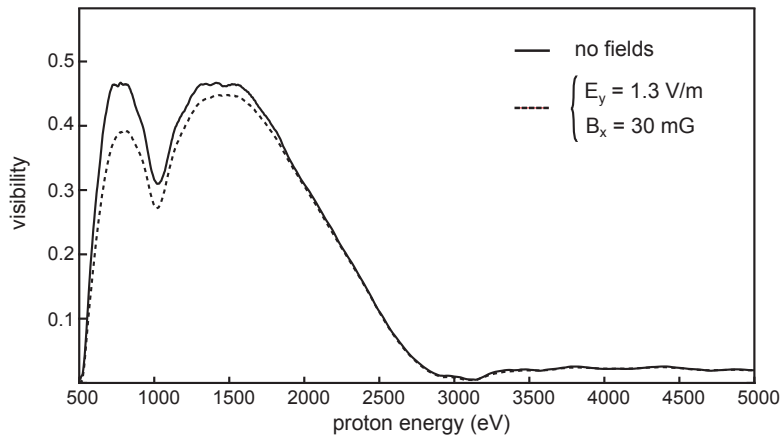


Figure 5.3: The visibility of the fringes calculated as a function of the proton energy, reevaluated for the fields measured inside the magnetic shield. Since the distance between the gratings is of 73 mm (short configuration), the fields are not affecting dramatically the signal of the interferometer. The open fraction of the gratings is 40% (courtesy of A. Demetrio).

Compared to the configuration where no fields are acting, the interferometer is not affected dramatically for $E_y = 1.3 \text{ V/m}$ and $B_x = 30 \text{ mG}$. Therefore, we can safely state that the fields are controlled in the interferometer volume.

¹The field is estimated to be uniform within 1 % based on Biot-Savart calculation [87].

5.2 Shift ambiguity and maximal field

The shift between the pattern formed by the ions and the pattern of hydrogen is subject to an ambiguity. There is indeed no way to distinguish a certain shift from the same shift modulo the pattern's period d . Therefore, choosing the smallest Δy defines implicitly the maximal field that can be measured by the moiré fieldmeter: the shift can at most be equal to the periodicity d . Replacing Δy by d in equation (3.12), the maximal fields can be expressed as:

$$\begin{aligned} E_{y,\max} &= \frac{2dV_{\text{acc}}}{L^2}, \\ B_{x,\max} &= \frac{d}{L^2} \sqrt{\frac{2mV_{\text{acc}}}{q}}. \end{aligned} \quad (5.4)$$

For 2 keV ions, $L = 171$ mm and $d = 40$ μm , it corresponds to 5.5 $\text{V}\cdot\text{m}^{-1}$ and 63 mG. (35 $\text{V}\cdot\text{m}^{-1}$ and 1.6 G for $L = 34$ mm). In practice, the moiré fieldmeter is therefore a fine measurement device which needs to be associated to a standard fieldmeter.

5.3 Charge-up effects

Inhomogeneous electric fields may cause the deformation of the moiré fringes. To illustrate this effect, three wires made of a non conductive material (kapton®) were placed temporarily on the side of the fieldmeter. A photograph of the setup is presented in figure 5.4.

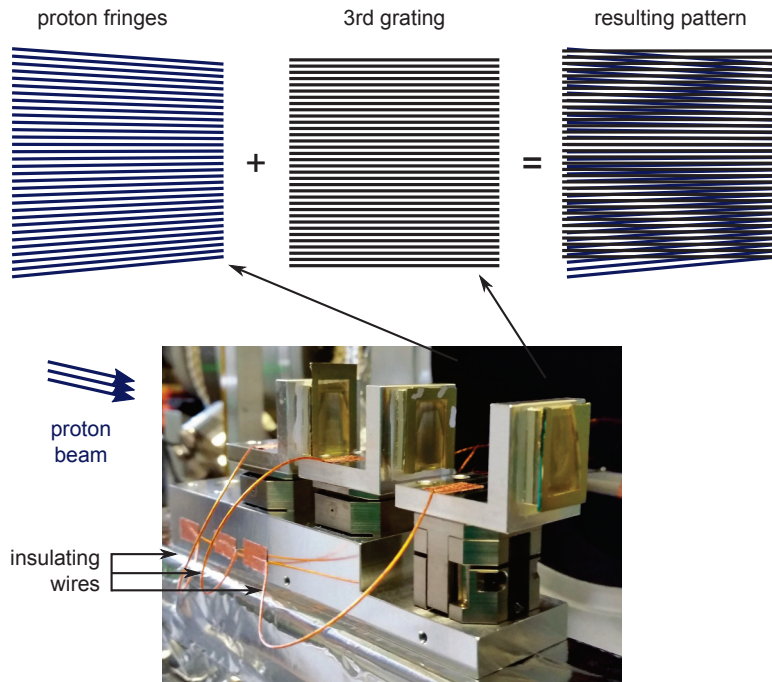


Figure 5.4: To illustrate the charge-up effect, wires made of an insulating material (kapton®) were placed temporarily on the side of the fieldmeter. As the wires are charging up, an inhomogeneous field is created and distorts the pattern formed by the protons. Superimposed with the last grating, a peculiar moiré pattern can be obtained on the detector.

As the wires charge up, an inhomogeneous electric field is created and distorts the pattern formed by the protons. A peculiar moiré pattern can then be observed on the detector: it corresponds to the superimposition of the third grating and the distorted ion fringes. The validity of this interpretation can be verified by rotating the second grating, as depicted in figure 5.5. The upper panel shows the pictures obtained by superimposing a grating with the distorted fringes while the experimental images are displayed on the bottom panel.

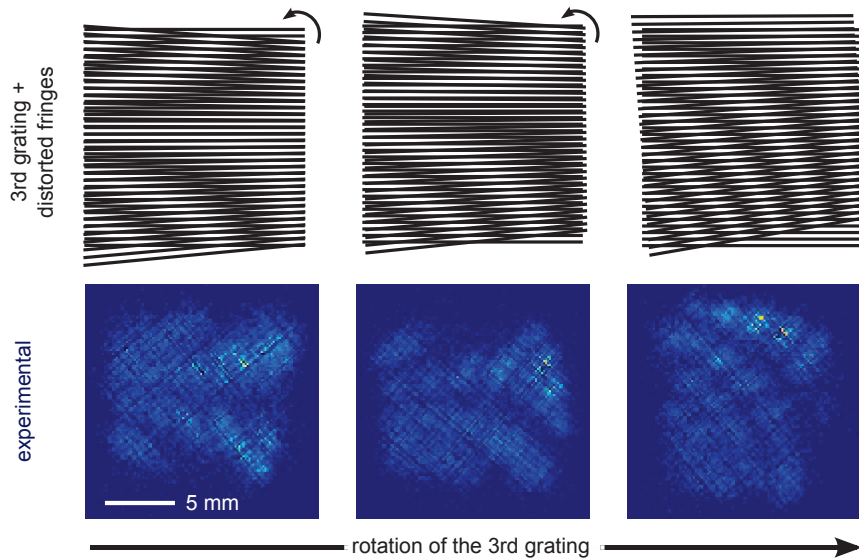


Figure 5.5: From left to right: the second grating is rotated counter clockwise. The upper row shows the pictures obtained by superimposing a grating to distorted fringes while the experimental images, obtained with the insulating wires, are displayed on the bottom panel.

5.4 Summary

The reliability of the moiré fieldmeter was evaluated by the mean of two coils creating an homogeneous magnetic field. The magnetic field measured was in good agreement with the output of a Hall probe, while the electric field did not show any evolution. The fields inside the mu-metal shield were also evaluated: we found $E_y = 0.91 \pm 0.31 \text{ V.m}^{-1}$ for the electric field and $B_x = -15.2 \pm 6.8 \text{ mG}$ for the magnetic field. Taking this field into account, the visibility of the interferometric fringes is expected to decrease at most by 18 %, compared to the situation where no fields would be present. To highlight the charge-up effect, a wire was temporarily placed nearby the fieldmeter and was exposed to the ion beam. The highly inhomogeneous field hence created seems consistent with the deformation of the moiré pattern experimentally observed. Finally, we stress that the shifts measured with the fieldmeter are of the same order of magnitude than the one expected in the AEGIS experiment. Measuring gravitational acceleration with such an apparatus seems therefore promising.

6 | Toward an Antiproton Interferometer

We have seen in chapter 3 that a Talbot-Lau interferometer is a remarkable tool to probe the wave behavior of heavy particles. The PIXIE experiment, introduced in chapter 4, is currently being developed to perform the interferometry with protons. But, in the future, the expertise acquired with protons could be used to interfere equivalently antiprotons. This idea was proposed in 2014 under the name ATLIX for Antimatter Talbot-Lau Interferometry eXperiment [137]. Since the wave behavior of antiproton and protons are expected to be identical, the ATLIX experiment would deal with the exact same device as the one presented in chapter 4. However, several noticeable differences with the PIXIE experiment are foreseen. It deals with the energy of the antiproton beam (5.3 MeV at the exit of the antiproton decelerator, see section 2.2.2), the specificities of antiproton interactions (such as the range of penetration and the antiproton annihilation) and the choice of an adapted detector. For this purpose, we decided to build a dedicated deceleration beamline. Placed at the exit of the antiproton decelerator (AD), this beamline reduces the energy of the antiprotons from 5.3 MeV to few keV. Moreover, a silicon detector was commissioned with low-energy antiprotons. Thanks to its fast readout capabilities, this detector allows one to use time-of-flight method to estimate the energy of the antiprotons leaving the beamline. Besides, the detector is associated to an algorithm used to estimate the coordinates of the antiproton annihilation vertex. After having introduced the deceleration beamline and presenting its performance, we review the detector characteristics and the spatial resolution achieved. Finally, the question of the feasibility of the ATLIX experiment in terms of acquisition time is addressed in the last section.

6.1 The ATLIx experiment specificities

Although there is not much doubt that antimatter obeys the laws of quantum mechanics, no experimental evidence of interferometry with antiparticles has been presented so far. The known attempts of antimatter interferometry, dealing either with positrons [138], [139] or a bound state of particle-antiparticle such as positronium [140] and muonium [141], suffered from the requirements of high spatial coherence for the sources of positrons or from the difficulty to form a stable particle beam. These issues are circumvented in the case of Talbot-Lau interferometry since the first grating creates the spatial coherence.

The interferometry of antiprotons raises the same challenge as for the interferometry of protons since the situation is known to be fully symmetric under CPT transformation. A few differences with the matter counterpart experiment should nevertheless be pointed out:

- **Antiproton interactions.** Because of its antimatter nature, the interaction of antiproton with the gratings present some specificities. Indeed, the annihilation of an antiproton releasing a few GeV makes it possible to form heavy fragments with the material. Moreover, as the radiation length of these particles is larger than the one for protons (see section 6.2), the range of antiprotons in the gratings material has to be reevaluated.
- **Source.** The interferometer is designed to work for particles in the keV range which corresponds to a very low energy range for antiprotons, extracted at a few MeV at the level of the AD. A specific beamline to decelerate them has thus to be built. A significant difference is however expected concerning the intensity delivered. Indeed, if the proton source is easily able to provide 10^7 particles per second, the AD releases the same number of particles in bunches of 200 ns every 120 seconds (see section 2.2.2).
- **Detector.** The detector used in ATLIx has hence to be able to acquire in a trigger mode, to comply with the AD constraints (bunched beam). It has moreover to identify an antiproton with sufficient efficiency and reconstruct the impact coordinate with resolution at least of the order of $100\ \mu\text{m}$ as planned in the ATLIx proposal [137].

We present in the following a beamline and a detector able to handle the ATLIx specificities.

6.2 The antiproton deceleration beamline

As seen on figure 6.1, the antiprotons delivered by the AD experience several operations to reduce their energy. The antiprotons pass firstly through a Gas Electron Multiplier (GEM), a detector used to monitor the position of the AD beam. Once the beam aligned with the center of the GEM, the antiprotons pass through several metallic foils (degrader) to reduce (and spread) their energy from 5.3 MeV to a few hundreds of keV. Most of the antiprotons annihilate within the degrader leading to the formation of pions (pion burst) which travel in a few nanoseconds to the detector. The antiprotons having less than 10 keV energy are then selected from the fast antiprotons by two electrostatic deflector plates located in a separate vacuum chamber and bending the beam at an angle of approximately 40 degrees. After having traveled a distance of 1.35 m from the degrader, slow antiprotons are finally imaged on the Timepix, a silicon detector with fast readout. Each element is described in the following sections.

In order to confine the beam, widely spread after the degrader, two einzel lenses (not displayed on the schematic) are placed downstream and upstream from the deflector plates. The different optical elements are placed in a DN200 vacuum chamber kept at 10^{-7} mbar.

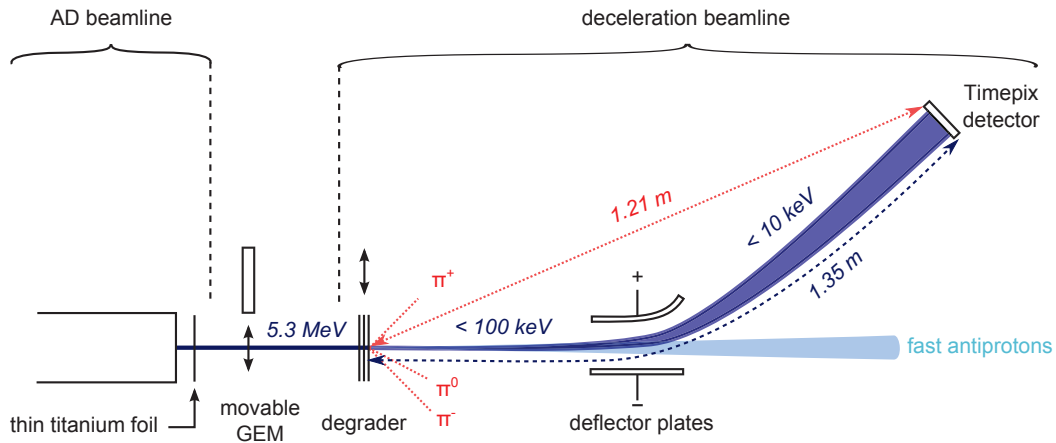


Figure 6.1: Schematic view of the antiproton deceleration beamline. The position of the beam is firstly monitored by a movable Gas Electron Multiplier (GEM) placed at the exit of the AD. Once the beam aligned with the center of the GEM, the antiprotons pass through several metallic foils (degrader) to reduce (and spread) their energy from 5.3 MeV to a few hundreds of keV. Most of the antiprotons annihilate within the degrader leading to the formation of pions (pion burst) which travel within a few nanoseconds to the Timepix detector. The fraction of antiprotons having less than 10 keV energy is then selected by two deflector plates and sent toward the Timepix detector.

6.2.1 Energy range

To act effectively as a grating, the gratings material should remain opaque to antiprotons. This constrain drives the range of energy at which the ATLIX experiment can be performed. The transmission of antiprotons through a membrane of silicon nitride is shown in figure 6.2 for different energies. It is simulated with Geant4 [162], a software dedicated to the interaction of particles through matter, presented in annex B, for a 160 nm thick membrane covered on both side with 10 nm of gold.

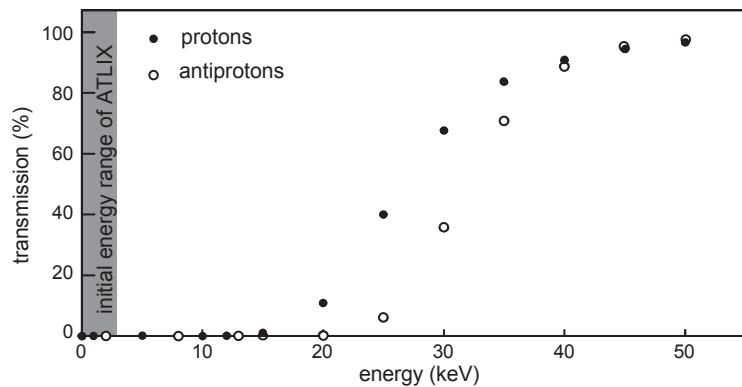


Figure 6.2: The transmission of protons and antiprotons through a membrane of silicon nitride, simulated with Geant4 [162]. The membrane thickness is 160 nm and is moreover covered with 10 nm of gold on both sides. The difference in range, known as the Barkas effect, is due to the opposite charges of the proton and antiproton. The original range of energy planned for ATLIX is indicated in gray. (courtesy of A. Lesauvage)

As a comparison, the transmission of protons is also displayed on figure 6.2. One can notice that for the same energy, protons are less absorbed by the material. This difference of range

between a particle and its anti-partner (due to the opposite charges) is known as the Barkas effect [160]. Reference [161] gives a comparison of the stopping power for proton and antiproton for energies until 540 keV. It is important to notice that most of simulation softwares lack of experimental points for lower energies and the numbers presented here should therefore be taken carefully. To ensure that the gratings remain opaque, it would be therefore safe to limit the antiproton energy to 10 keV. This result extends slightly the range of 0 to 3 keV initially foreseen in the ATLIX proposal [137] (in which the metal coating was not taken into account).

6.2.2 AD beam monitoring

As the position of the AD beam is likely to fluctuate from one day to another, one may wonder how reliable are the data taken over periods that can possibly extend several weeks. In order to operate the beamline in a reproducible way, an independent beam monitor is therefore needed.

Gas Electron Multiplier

For this purpose, the Gas Electron Multiplier (GEM) [157] detector developed at CERN for the AD experiments is well suited. It consists of a plate of insulating material, metalized on each side, on which an array of channels has been drilled. Similarly to MCP (see section 4.5.1), a high voltage is applied between the two sides of the plane to create a high electric field within the channels. It provides an amplification of the primary ionization occurring when a charged particle crosses the detector. The electron signal is then collected by two series of anodes which give us access to the horizontal and vertical distributions of the beam. A photograph of the GEM detector ($10 \times 10 \text{ cm}^2$) is shown on figure 6.3.

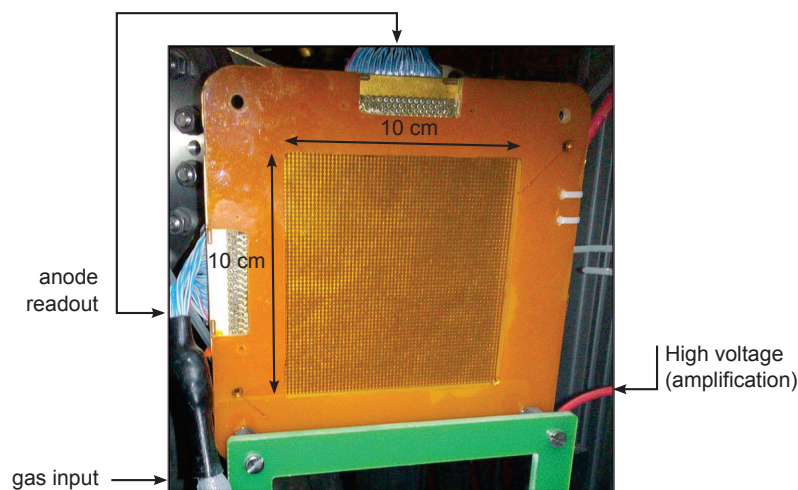


Figure 6.3: Photograph of the GEM detector, used to monitor the position of the antiproton beam. The detector is mounted on an actuator which allows one to place it in front or out of the beam.

The GEM is mounted on an actuator which allows one to place it in front or out of the beam. Note that the beam gets entirely absorbed when the GEM is placed in front of the beam (destructive measurement).

Plastic scintillator

To monitor the beam position in a non destructive way, we envisioned to replace the GEM detector by an in-line diagnostic. It consists in a thin foil of a plastic scintillator¹ converting the antiproton into light with a high efficiency. The light is then collected by a standard CCD camera placed on the side of the scintillator. The specifications of the scintillator foil are given in table 6.1.

Scintillator foil	
type	EJ-212
efficiency	1 photon per 100 eV deposited
density	1.023 g/cm ³
thickness	100 μ m
wavelength of max. emission	423 nm (blue)

Table 6.1: Specifications of the plastic scintillator foil (from the website of the producer [159]).

An image of the beam as seen by the camera is shown in figure 6.4 (right). For each shot, the horizontal and vertical profiles of such images are fitted by a gaussian function. That way, the coordinate of the beam center are known with a sub-millimeter precision. The spread of the beam is evaluated $\sigma_h = 2.01 \pm 0.02$ mm and $\sigma_v = 1.35 \pm 0.03$ mm for the horizontal and vertical spread respectively.

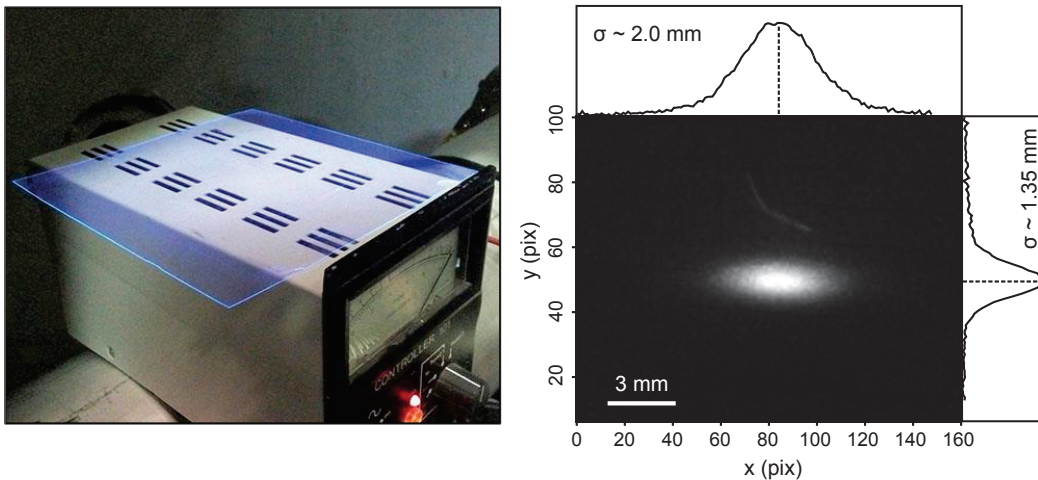


Figure 6.4: Photograph of the scintillator foil (left) and image of the beam taken at the exit of the AD line (5 ms exposure time). The ovoid shape is due to the perspective of the camera, looking at the beam from the top side. The beam position is evaluated with a sub-millimeter precision by fitting the profiles with a gaussian distribution.

¹sufficiently thin not to affect the energy and straggling of the incoming beam.

AD beam drift

The position of the AD beam, measured with the plastic scintillator for 8 hours, is shown in figure 6.5.

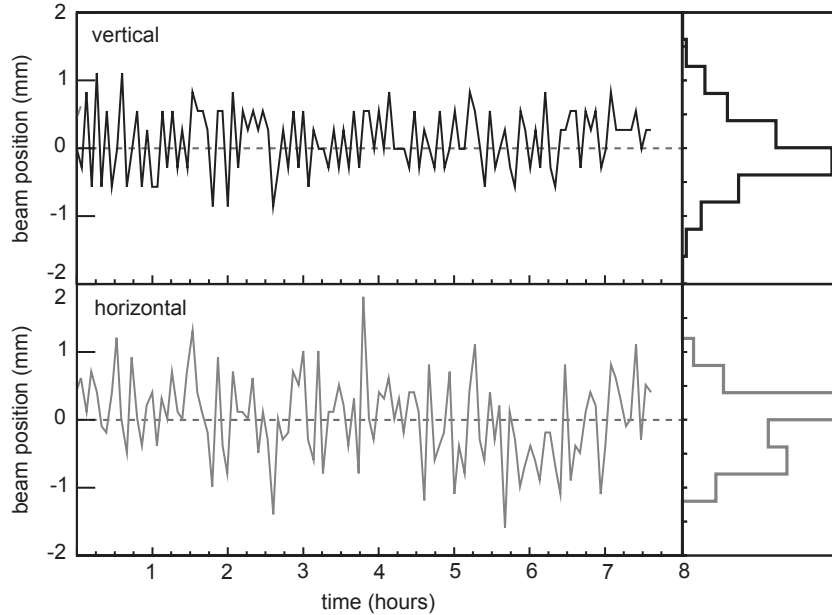


Figure 6.5: Evolution of the beam vertical and horizontal positions, measured with the scintillator, during a 8 hours time window. No significant drift can be seen.

During the 8 hours acquisition, no deviation larger than 2 mm have been observed. As the AD position is nevertheless known to vary from one day to another, the strategy retained is to realize the steering at the beginning of each period of data taking with the GEM planes.

6.2.3 Degradер

To decelerate the antiprotons, the first step consists in placing in front of the beam a thin foil of material, or degrader. Through the degrader, antiprotons experience multiple collisions (scattering) which results in an effective loss of energy. The counterparts of this technique is that:

- the momentum of the beam is widely spread,
- the flux of antiprotons leaving the degrader is significantly reduced.

As shown in figure 6.6, the degrader consists of a thin titanium foil (thickness to measure), used to seal the vacuum of the AD beamline, several thin sheets of aluminum whose thickness can be tuned, and a 25 μm titanium foil. The two titanium foils are spaced by 4 cm of air.

Titanium foil thickness

In order to estimate the thickness of the first titanium foil, we compare Monte Carlo simulations (MC) with experimental data acquired at CERN. The simulation is done with Geant4 [162].

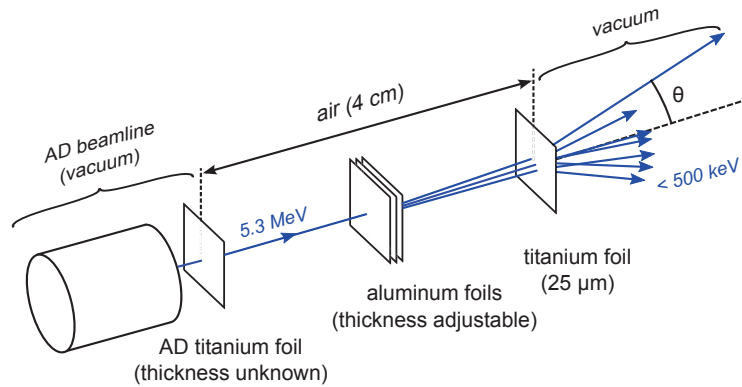


Figure 6.6: Schematic view of the degrader. It is made of a thin titanium foil (thickness to measure), used to seal the vacuum of the AD beamline, several thin sheets of aluminum whose thickness can be tuned, and a $25 \mu\text{m}$ titanium foil. The two titanium foils are spaced by 4 cm of air.

The average number of antiprotons observed on the Timepix detector as a function of the aluminum foil thickness is shown in figure 6.7. The transmission curve corresponding to a thickness of $94 \mu\text{m}$ for the first titanium foil is also displayed (dashed line). The curve is moreover normalized to the same intensity as the data point, to take into accounts the efficiency of the Timepix detector and of the beamline, presented in the next section.

As one can notice from the data points, there is a thickness of aluminum for which the number of antiprotons is maximal. This optimum can be understood as follows. If the aluminum foil is too thin, the antiprotons are not sufficiently decelerated, and none of them have an energy of a few keV. In opposite, a thick aluminum foil will stop all the antiprotons. For a selected energy of 3 keV and an aluminum thickness of $33 \mu\text{m}$, one observe in average 23 antiprotons.

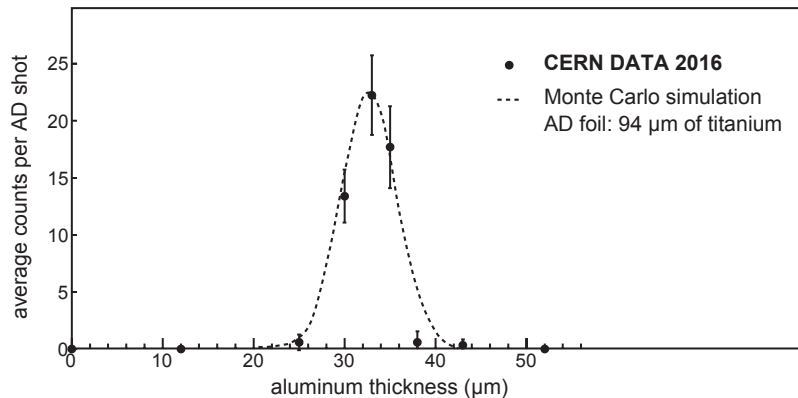


Figure 6.7: Average number of antiprotons reaching the Timepix detector as a function of the thickness of the aluminum foils. Each data point is the flux averaged over 10 to 20 shots and the error bar represents the standard deviation. The antiprotons were selected at an energy $E = 3 \text{ keV}$. The dashed curve is the number of antiprotons simulated for a thickness of $94 \mu\text{m}$ for the first titanium foil. It is simulated for an incoming beam of $3 \cdot 10^7$ antiprotons having an energy $3 \pm \Delta E \text{ keV}$, where $\Delta E = 680 \text{ eV}$ is the (measured) energy spread of the beam reaching the Timepix detector and will be presented in section 6.2.6.

Energy distribution

The energy distribution of the antiprotons leaving the degrader is plotted (in log-log scale) on figure 6.8 for an incoming beam consisting of $3 \cdot 10^7$ antiprotons at 5.3 MeV. It is simulated for 94 μm of titanium for the AD foil and a degrader of 33 μm of aluminum. The distribution is roughly uniform from 0 to 20 keV and decreases then to zero at 600 keV. In terms of flux, it is important to notice that about 82 % of the AD beam is stopped by the degrader. Besides, the number of antiprotons in the energy range investigated by the ATLIX experiment (up to 10 keV, see section 6.2.1) represents only $\sim 10\%$ of the incoming beam.

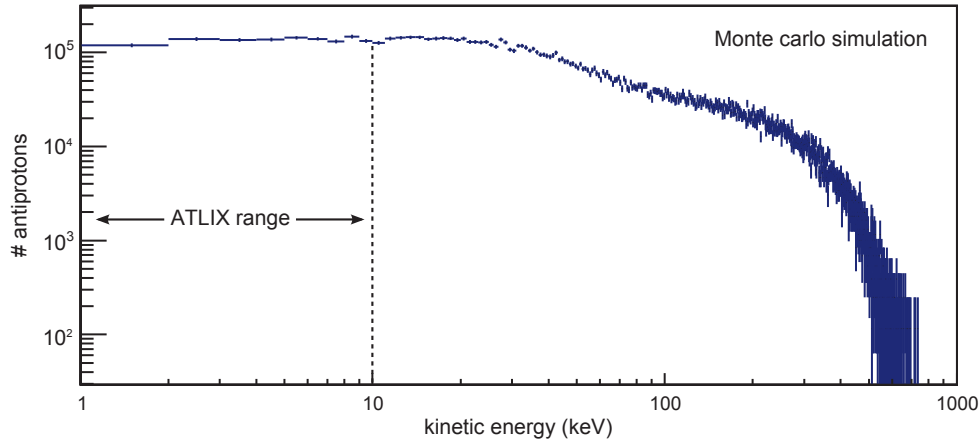


Figure 6.8: Energy distribution of the antiprotons leaving the degrader, for an incoming beam consisting of $3 \cdot 10^7$ antiprotons at 5.3 MeV. It is simulated for a thickness of 94 μm of titanium for the AD foil and a degrader made of 33 μm of aluminum. Only 10% of the $3 \cdot 10^7$ incoming antiprotons delivered by the AD has an energy between 0 and 10 keV, the energy range of the ATLIX experiment.

6.2.4 Position of the interferometer

The number of antiprotons reaching the detector is expected to be low given the efficiency of the degrader. In order to maximize the number of antiprotons toward the interferometer, we compare the three configurations shown in figure 6.9.

In these setups, the interferometer is placed either (a) at the exit of the deceleration beamline, (b) inside the deceleration beamline, downstream of the deflector plates, or (c) in front of the degrader without using any electrostatic selection. In configuration (c), we assume that the energy can be resolved using the time-of-flight information from the detector. To emulate the output of the degrader, the incoming beam consists in 10^4 antiprotons spread over a spot of 20 mm in diameter and has a divergence of 15 degrees (half opening angle). Each configuration have been simulated with SIMION 8.1 [89] for a beam of 1 keV as an input. For the sake of simplicity, the interferometer is modeled by a tube (560 mm long and 3 mm in diameter). The number of antiprotons reaching the detector is listed in table 6.2 for each configurations.

6.2.5 Operating settings

For the configuration presented in figure 6.9.a., one may wonder which voltage applied on each element of the beamline leads to the highest flux of antiprotons. The evolution of the flux as a function of the voltage applied on the lenses is given in figure 6.10. Each point is simulated for an incoming beam of 1 keV, 20 mm in diameter and with a divergence of

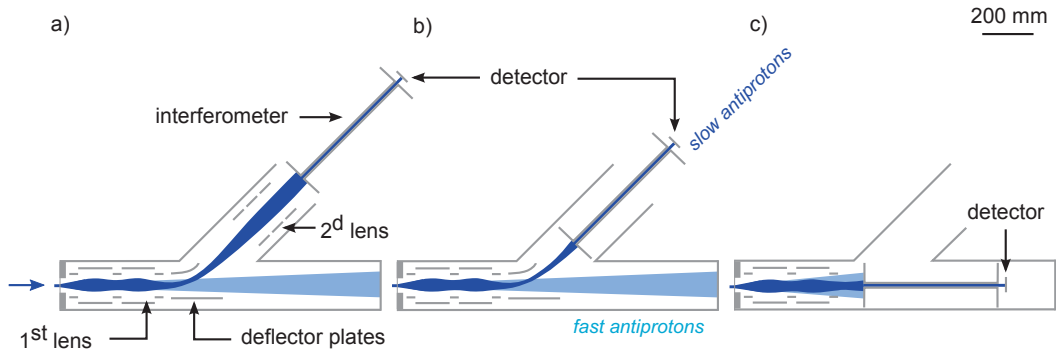


Figure 6.9: Top view of three possible configurations where the interferometer is placed (a) outside the deceleration beamline, (b) partially inside the beamline and (c) in front of the degrader without using any electrostatic deflection.

configuration	1 st lens	def. plates	2 nd lens	time-of-flight	$\langle N_{\text{antiprotons}} \rangle$
a)	1000 V	± 500 V	1000 V	4.25 μs	2.6
b)	1000 V	± 500 V	-	2.89 μs	2.2
c)	1000 V	-	-	2.44 μs	1.1

Table 6.2: The average number of antiprotons reaching the Timepix for the three setups presented in figure 6.9. The voltages applied on each elements and the time-of-flight of the antiprotons (for a 1 keV beam) are also indicated.

15 degrees. As one can see from the plots, each of the lenses presents a optimum voltage, at which it should be operated. Although the first lens presents a clear optimum, peaking at the energy of the incoming beam, the influence of the second lens is weaker.

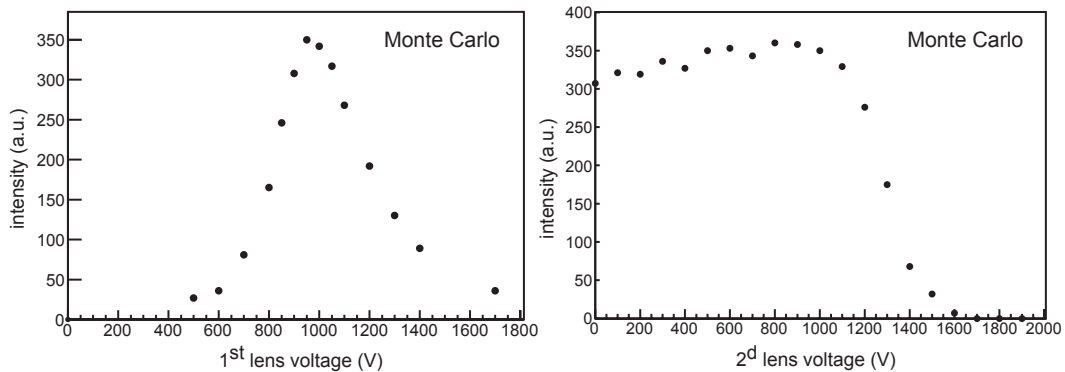


Figure 6.10: The flux of antiprotons reaching the Timepix as a function of the voltage on the lenses, simulated for a 1 keV incoming beam. Although the first lens presents a clear optimum, peaking at the energy of the incoming beam, the influence of the second lens is weaker.

As shown in figure 6.11, the energy of the antiprotons reaching the Timepix scales linearly with the voltage applied on the deflector plates. It is simulated for an incoming beam having a uniform distribution between 0 and 10 keV. Each point is the mean value of the energy distribution measured at the position of the Timepix.

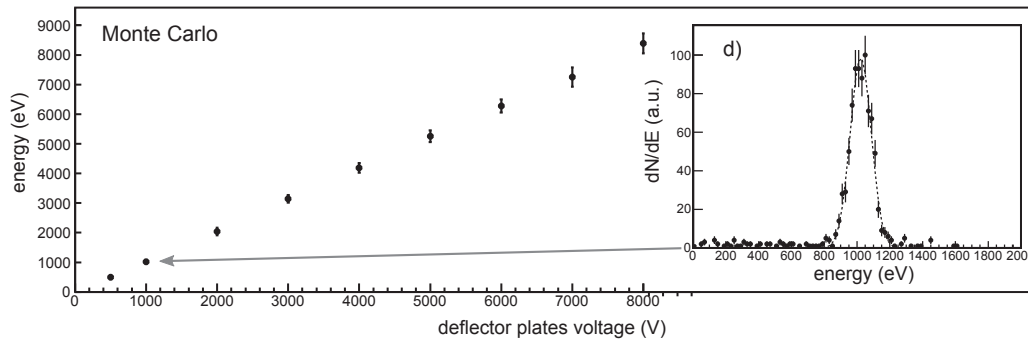


Figure 6.11: The energy of the antiprotons reaching the Timepix scales linearly with the voltage applied on the deflector plates. The energy distribution for a 1 kV difference between the two plates is displayed on the close-up. The distribution is obtained for a beam having a uniform distribution between 0 and 10 keV.

The geometrical acceptance of the deflector plates and lenses lead to a certain tolerance on the energy of the particles selected. The energy distribution obtained for a 1 kV difference between the two plates is displayed on figure 6.11 (close-up). The simulation indicates that the energy spread is approximately $\Delta E/E = 0.2$.

6.2.6 Energy spread

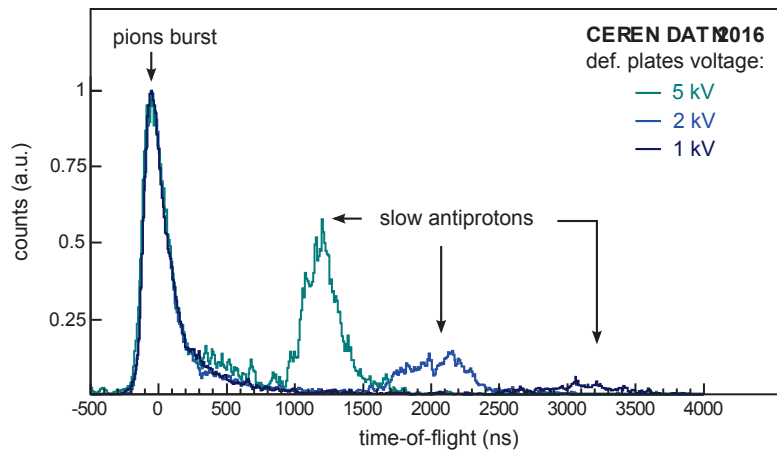


Figure 6.12: The time-of-flight distribution of the antiprotons for different voltages applied between the deflector plates. The time reference ($t = 0$) is given by the pion burst, corresponding to the annihilation of most of the antiprotons into the degrader. Knowing the distance traveled by the antiprotons, the time-of-flight allows one to retrieve their energy distributions.

The energy distribution of the antiprotons can be measured experimentally by time-of-flight with the Timepix detector. Indeed, as most of the beam annihilates within the degrader, a large number of pions is emitted in all directions. Since their velocity is close to the speed-of-light, they travel almost instantaneously (within 3 ns) from the degrader to the Timepix. This “pion burst” is therefore used as the time reference ($t = 0$) for the time-of-flight measurement. Instead, the slow antiprotons selected by the deflector plates travel at a lower velocity (1 keV

corresponds to a velocity of $\sim 4.4 \cdot 10^5 \text{ m}\cdot\text{s}^{-1}$ or a time of flight of $3.1 \mu\text{s}$). The time-of-flight distribution of the antiprotons is given in figure 6.12 for different deflector plates voltages. One can notice the presence of a first peak corresponding to the pion burst. As the distance between the Timepix detector and the degrader is known ($L = 1.35 \text{ m}$), the energy distribution of the antiprotons can be deduced by the expression:

$$E = \frac{1}{2}mv^2, \quad (6.1)$$

$$E = \frac{1}{2}m \left(\frac{L}{\tau} \right)^2,$$

where τ is the time-of-flight of the antiprotons. The mean energy, energy spread and flux of the antiprotons are listed in table 6.3 for several deflector plates voltage.

plates voltage (kV)	mean energy E (keV)	r.m.s ΔE (keV)	$\Delta E/E$	average number of \bar{p} / shot
0	-	-	-	0 to 3
1	0.93	0.20	0.22	8
2	2.16	0.52	0.24	19
3	2.97	0.68	0.23	25
5	6.07	1.48	0.24	32

Table 6.3: Mean energy, energy spread and flux of the antiprotons reaching the Timepix as a function of the voltage applied between the deflector plates.

The energy of the antiprotons is of the order of the voltages applied on the deflector plates, in agreement with the SIMION finite element simulations. For each voltage, the energy spread $\Delta E/E$ is comprised between 0.22 and 0.24. It is worth noticing that the flux increases with the energy of the antiprotons selected. This could be the consequence of the sensitivity of low energy antiprotons to surrounding electric and magnetic fields. Nevertheless, the number of antiprotons reaching the detector when no voltage is applied is not zero. As no straight trajectory can be drawn between the degrader and the detector, this effect is interpreted as the bouncing of fast antiprotons on the walls of the vacuum chamber.

6.3 The Timepix detector

6.3.1 High resolution imaging detectors for particle tracking

The detector used in ATLIX has to identify an antiproton annihilation vertex with a resolution of a few microns. To this end, we compare here the performance of nuclear emulsions, a phosphor screen read by a camera and a silicon detector. A comparative view of a few antiprotons annihilations on the three detectors cited above is shown in figure 6.13.

Nuclear emulsions

Based on a technology developed for the OPERA experiment [147], the nuclear emulsions consist of plates of plastic covered with AgBr(I) crystals distributed homogeneously in a gelatin substrate. When excited by a charged particle, the annihilation products, such as pions, imprint on the emulsion plate a latent image. A chemical developing treatment, followed by a tomographic scan through the sensitive layer, reveals then a three-dimensional view of the vertices. But in spite of their impressive imaging capabilities (able to reconstruct

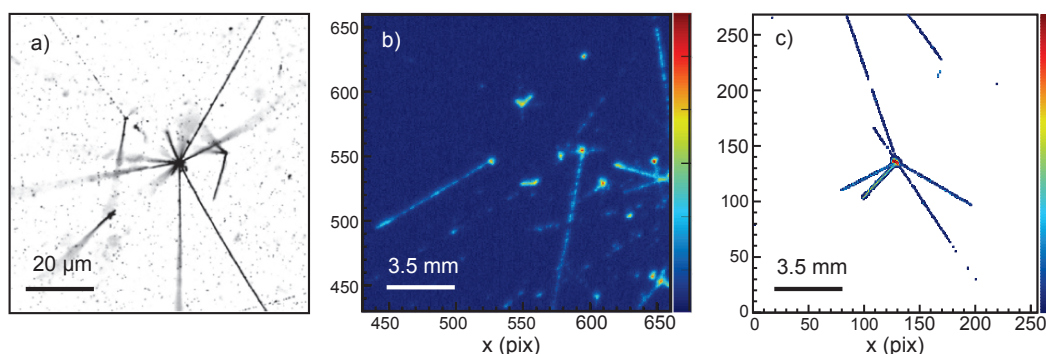


Figure 6.13: Few typical antiproton annihilations events as seen on (a) a nuclear emulsion plate, (b) on the hydrogen detector, a MCP stacked to a phosphor screen read by a CCD camera and (c) on the Timepix silicon detector. To appreciate the impressive capabilities of the nuclear emulsion, it is worth to notice that the size of the image (a) corresponds to an area of 2×2 pixels on the image (c).

the antiproton annihilation vertices with a precision of $2 \mu\text{m}$), the emulsion films require to open regularly the vacuum chamber and need a large amount of time to be processed.

MCP + phosphor + camera

As a comparison, digitized detector offer easier handling. Since the detection efficiency of a standard MCP reaches easily 95 % for GeV pions [72], the same detector used for proton interferometry (a MCP, a phosphor screen and a camera) could be used as well for antiprotons. It is fully vacuum compatible, digitized, and offers a resolution of a few microns. It is furthermore a well-known detector in plasma physics which has been used extensively for antiproton manipulation diagnostics. But its readout time, limited by the camera to a few milliseconds, makes such a detector inappropriate for time-of-flight measurements.

The Timepix silicon detector

The above disadvantages oriented our choice toward silicon detectors, which can easily tackle time capabilities of nanoseconds. We describe in the following the specifications of the Timepix detector [149], initially developed for medical imaging applications [150]. Associated with a track recognition algorithm, the detector is able to determine with $25 \mu\text{m}$ resolution the position of an antiproton with a 56 % tagging efficiency [155].

6.3.2 General characteristics

The Timepix detector consists in a $675 \mu\text{m}$ thick silicon detector, bump-bonded to a fast read-out Application-Specific Integrated Circuit (ASIC). It consists of a matrix of 256×256 pixels with $55 \mu\text{m}$ pitch, covering a $14.1 \times 14.1 \text{ mm}^2$ sensitive area. The ASIC can simultaneously measure for each pixel the energy deposited, and the time-of-flight (referenced to the delivery of the antiproton beam) with a 1.58 ns accuracy [149]. In our setup, a depletion voltage of 200 V is applied and the acquisition is triggered by a TTL pulse for each AD shot. A photograph of the Timepix detector is shown on figure 6.14.

Similarly to time projection chambers, the time-of-arrival for each pixel can be used to obtain a 3D images of the annihilation vertices, as it is directly correlated to the distance between the points where the primary electrons-holes pairs are formed (within the silicon bulk) and

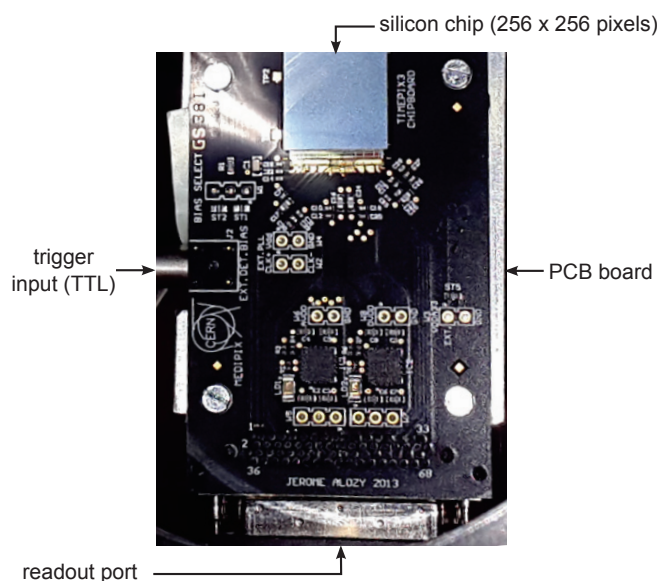


Figure 6.14: Photograph of the Timepix detector. The silicon chip is bump bonded to a fast readout Application-Specific Integrated Circuit (ASIC) which consists of a matrix of 256×256 pixels. In our setup, the acquisition is triggered by a TTL pulse for each AD shot.

the readout pixel. This feature is only possible since the sensor is sufficiently thick. Reference [151] gives an example of such a reconstruction, based on the electron mobility in silicon.

6.3.3 Tagging efficiency

Since the Timepix detection efficiency is practically 100 % for charged particles with energies above 10 keV (such as pions) [152], one could think that the identification of an antiproton annihilation is straightforward in most of the cases. This is unfortunately not verified experimentally: the distinction between an antiproton and a heavy fragment (originating from the annihilation of an antiproton in the silicon sensor) is indeed complicated when the charged pions tracks (or “prongs”) are not visible on the detector image. This is mainly due to the fact that pions emitted perpendicularly to the readout plane are not detected by the Timepix. The fraction of events for which a clear identification is possible, or tagging efficiency, is therefore smaller than one.

To distinguish an antiproton from a heavy fragment, we require the annihilation to present at least two prongs. The tagging algorithm developed in the AEGIS collaboration relies moreover on the presence of a cluster larger than 10 pixels and the presence of a central region with energy deposition above 800 keV. The tagging efficiency reached with these criteria is 56 % [155].

6.3.4 Spatial resolution

Once an antiproton is tagged, its coordinates on the detector can be retrieved by a dedicated pattern recognition algorithm. The algorithm is based on the Hough transform, a tool used in image processing to find a line on an image. As seen in figure 6.13.c, the energetic pions

released during the antiproton annihilation imprint straight tracks on the Timepix detector. The Hough transform, explained in more details in annex A, can then be used to find the pions tracks. For each pixel of the image (with coordinates x and y), the underlying idea is to associate the coordinates (r, θ) defined by:

$$r = x \cos \theta + y \sin \theta. \quad (6.2)$$

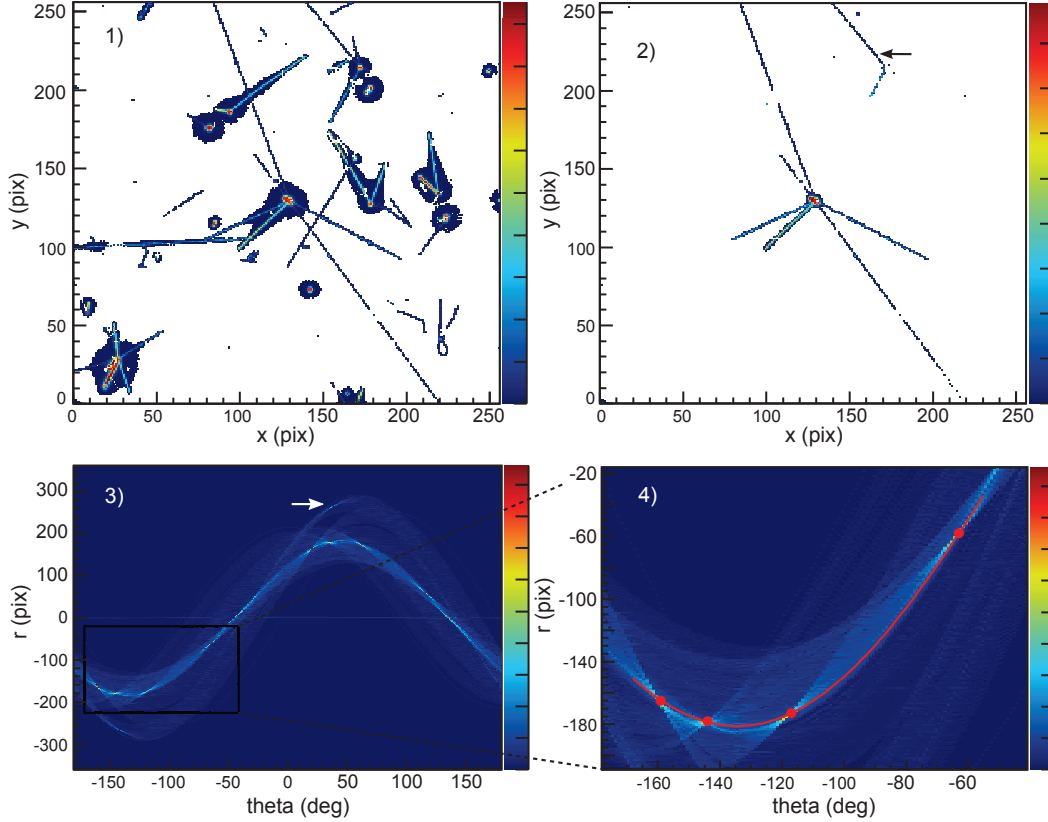


Figure 6.15: The different steps of the algorithm used to retrieve the coordinates of the annihilation vertex. A selection on the antiprotons time-of-flight distribution is first made from the raw image (1) to select the slowest antiprotons (2). The picture obtained serves as an input for the Hough transform (3). For a better visualization of the sinus-like curves, the Hough space is here plotted from -180 to $+180$ degrees. Notice that the same information appears therefore twice. The four pion tracks leaving the annihilation vertex as well as another pion track (arrow) are visible as local maxima in the Hough space. The (r, θ) coordinates of each tracks are then retrieved by a local maximum finding algorithm (4). The vertex coordinates are finally retrieved by fitting the (r, θ) coordinates by expression (6.2).

The algorithm, detailed in reference [155], is illustrated in figure 6.15 with genuine data from the Timepix detector. It proceeds as follows:

- Slow antiprotons are selected by time-of-flight. Examples of time-of-flight distributions, for which the slow antiprotons are unambiguously identified, will be shown in section 6.2.6;
- Following the change of coordinates (6.2), the image is transformed in the Hough space;

- Local maxima are searched in the Hough space. The (r, θ) found (each corresponding to a pion track) are fitted by expression (6.2) to retrieve the (x, y) coordinates of the annihilation vertex;

Similarly to the algorithm used to retrieve the proton impact coordinates (section 4.5.5), this algorithm is able to reconstruct the position of the annihilation vertex with a sub-pixel resolution, of the order of $25 \mu\text{m}$ [155]. More details on the tagging efficiency and spatial resolution achieved with the Timepix detector can be found in reference [155].

6.4 ATLIX feasibility

6.4.1 Expected flux and acquisition time

The number of antiprotons that can be used for the ATLIX experiment can be estimated from the efficiency of the degrader, of the beamline and of the detector tagging efficiency. For each AD shot, the expected number of antiprotons detected and correctly identified on the Timepix detector is:

$$N_{det} = \underbrace{25}_{\text{measured (3 keV)}} \times \underbrace{4.6 \cdot 10^{-2}}_{\text{surface}} \times \underbrace{0.017}_{\text{gratings}} \times \underbrace{0.56}_{\text{Timepix}}, \quad (6.3)$$

$$N_{det} = 0.011 \bar{p}/\text{AD shot.}$$

where the surface term is the surface of the interferometer gratings ($3 \times 3 \text{ mm}^2$) divided by the surface of the Timepix chip ($14.1 \times 14.1 \text{ mm}^2$). The transmission of the interferometer is given by the product of the open fractions of each gratings (listed in section 4.4.2). Since the AD beam is shared between the AEGIS apparatus and the ATLIX experiment, one can count on a reasonable number of 100 AD shots per shift (8 hours). It corresponds to at most 1.1 antiprotons per shift. Since a reliable estimation of the fringes visibility requires approximately 200 antiproton impacts [137], one should therefore plan 200 days of acquisition time for a given energy.

This statistical limit could be overcome in the near future with the implementation of the Extra-Low Energy antiproton Accelerator (ELENA, see section 2.2.2), which will deliver the antiprotons at an energy of 100 keV. As the energy would be reduced by a factor 50, the thickness of the degrader needed to decelerate those antiprotons to a few keV would have to be adapted. A proper study of the degrader thickness, material and mechanical stability should hence be performed.

6.4.2 Critical fields

As the energy spread of the antiprotons is larger than the one of the proton source, the sensitivity of the interferometer to electric and magnetic fields has to be reevaluated. For 1 keV antiprotons having an energy spread of 0.2, the critical fields are²:

$$\begin{aligned} E_c &= 0.24 \text{ V}\cdot\text{m}^{-1}, \\ B_c &= 10 \text{ mG}. \end{aligned} \quad (6.4)$$

The magnetic limit represents no issue since the mu-metal shield ensures a field of the order of 1 mG nearby the interferometer (see section 4.4.1). Instead, the electric field might be problematic due to the charging of the different insulated elements of the interferometer and

²calculated for a distance of 73 mm between the gratings.

of the detector. To reduce the electric field contribution, the design of the Timepix detector should be adapted to the experiment. It should especially be sufficiently compact to be placed inside the magnetic shield. Moreover, the exposure of the insulating component such as the PCB frame and cables should be reduced as much as possible.

6.5 Summary

In order to achieve the Talbot-Lau interferometry experiment of antiprotons, we have designed and built a dedicated deceleration beamline. To monitor the position of the antiproton beam, delivered by the AD, we decided to install a Gas Electron Multiplier (GEM) in front of the AD beamline. This detector is able to monitor the position of the beam with millimeter accuracy, which ensures the reproducibility of the data acquisition scheme. With a similar detector, we measured the drift of the AD beam over a 8 hours time window. No deviation bigger than 2 mm was observed. Based on the comparison of a Monte Carlo simulation with experimental data, we have estimated the thickness of the titanium foil placed at the AD. The results are consistent with a thickness of the order of 86 μm . Based on the data acquired at CERN during the 2016 run, we measured the flux reaching the detector with the design chosen. For a selected energy of 3 keV, we collected around 25 antiprotons per AD shot. We measured an energy spread of 0.2, in good agreement with simulations of the line. Furthermore, a silicon detector adapted to the antiproton specificities has been tested. By the mean algorithm based on Hough transform, this detector offers a 20 μm spatial resolution on the antiproton impact coordinates. The antiprotons impinging on the detector are identified in 56 % of the case. Finally, based on the efficiency of each elements deceleration beamline, the acquisition time needed to evaluate the visibility of the interferometric fringes was estimated to 200 days per energy considered. In order to minimize this time, the study of a degrader adapted to the future ELENA facility should be carried out. To reduce the electric field which might blur the interference pattern, the dimensions of the silicon detector should be reduced and a proper shielding of its insulating parts still have to be accomplished.

7 | Conclusion

Understanding the gravitational interaction of antimatter is a booming topic. In order to measure the gravitational acceleration of antihydrogen atoms, the AEGIS collaboration is currently designing a moiré deflectometer. It consists in a device made of three transmission gratings and an imaging detector. In this thesis, such an apparatus was tested with charged particles at low energy such as protons, H_2^+ and H_3^+ ions. We have shown that the moiré deflectometer is able to measure electric and magnetic fields with high accuracy. The sensitivity reached by such a “field-meter” is moreover enhanced if the gratings pitch is reduced. But, as soon as the grating pitch undergoes a certain scale, the diffraction of the ions nearby the grating slits has to be taken into account. The fieldmeter, turned into an interferometer, can then be used to highlight the wave behavior of protons.

The PIXIE experiment was set-up for this purpose. An effort was made to control the effects which could prevent the formation of the interference pattern. It deals more specifically with the control of the electric and magnetic field surrounding the interferometer. To this extent, we tested different metallic coating at the surface of the gratings. Moreover, a large part of the work was dedicated to characterize the beam delivered by the ion source. To this end, we have implemented a Wien filter, used to know precisely the nature of the ions delivered. The energy and energy spread of the beam were also measured. In addition, two detectors have been compared to improve the visualization of the interference pattern. By the mean of an algorithm calculating the coordinates of single protons impacts, the detector resolution is of the order of 14 μm , a high value compared to standard particle physics detector.

In the near future, the PIXIE experiment could be performed equivalently with antiprotons at CERN. A few challenges are however raised when dealing with antiprotons. It deals with the control of the beam energy and the choice of an imaging detector able to visualize the antiproton annihilations. Based on optics simulation tool, we designed a deceleration beamline, able to lower the antiproton momentum from 5.3 MeV to a few keV. The beamline, tested at CERN, have been able to select around 25 antiprotons at 3 keV with a relative energy spread of 0.2. The reproducibility of the beamline was a point particularly emphasized. To visualize the antiproton annihilations, we tested moreover the Timepix detector which is a silicon detector. With an algorithm based on the Hough transform, this detector is able to retrieve the coordinates of the annihilation vertex with a 25 μm resolution and a 56 % tagging efficiency.

That being said, the achievement of an antiproton interferometer is far from being over. Indeed, in the current setup, the acquisition time needed to observe a fringe signal extends over several weeks. In the years to come, one should benefit from the ELENA facility to increase the flux of antiprotons passing through the interferometer (and reduce the acquisition time). In this context, the study of a degrader able to reduce the beam from 100 keV to the desired energy should be carried out. Finally, the Timepix detector will have to be integrated into the existing setup. More especially, one should reduce the detector dimensions and shield the

insulating parts of the electronic board.

Bibliography

- [1] P. A. Dirac, The quantum theory of the electron, in Proceedings of the Royal Society of London A: Mathematical, Physical and Engineering Sciences (Vol. 117, No. 778, pp. 610-624). The Royal Society, 1928.
- [2] P. A. Dirac, A theory of electrons and protons, In Proceedings of the Royal Society of London A: Mathematical, Physical and Engineering Sciences (Vol. 126, No. 801, pp. 360-365). The Royal Society, 1930.
- [3] P. A. Dirac, Quantised singularities in the electromagnetic field, In Proceedings of the Royal Society of London A: Mathematical, Physical and Engineering Sciences (Vol. 133, No. 821, pp. 60-72). The Royal Society, 1931.
- [4] C. D. Anderson, The apparent existence of easily deflectable positives, *Science*, 76, 238-239, 1932.
- [5] C. M. G. Lattes, G. P. S. Occhialini, & C. F. Powell, Observations on the tracks of slow mesons in photographic emulsions, *Nature*, 160(4066), 453-456, 1947.
- [6] G. D. Rochester & C. C. Butler, Evidence for the existence of new unstable elementary particles, *Nature*, 160(4077), 855, 1947.
- [7] O. Chamberlain, E. Segrè, C. Wiegand & T. Ypsilantis, Observation of antiprotons, *Physical Review*, 100(3), 947, 1955.
- [8] B. Cork, g. R. Lambertson, O. Piccioni, & W. A. Wenzel, Antineutrons produced from antiprotons in charge-exchange collisions, *Physical Review*, 104(4), 1193, 1956.
- [9] D. E. Dorfan, J. Eades, L. M. Lederman, W. Lee & C. C. Ting, Observation of antideuterons, *Physical Review Letters*, 14(24), 1003, 1965.
- [10] T. Massam, T. Muller, B. Righini, M. Schneegans, & A. Zichichi, Experimental observation of antideuteron production, *Il Nuovo Cimento A (1965-1970)*, 63(1), 10-14, 1965.
- [11] P. Picozza et al., PAMELA - A payload for antimatter matter exploration and light-nuclei astrophysics, *Astroparticle physics*, 27(4), 296-315, 2007.
- [12] M. Aguilar et al., Antiproton Flux, Antiproton-to-Proton Flux Ratio, and Properties of Elementary Particle Fluxes in Primary Cosmic Rays Measured with the Alpha Magnetic Spectrometer on the International Space Station, *Physical Review Letters*, 117(9), 091103, 2016.
- [13] S. Perlmutter et al, Measurements of Ω and Λ from 42 high-redshift supernovae, *The Astrophysical Journal*, 517(2), 565, 1999.

- [14] A. Riess et al., Observational evidence from supernovae for an accelerating universe and a cosmological constant, *The Astronomical Journal*, 116(3), 1009, 1998.
- [15] J. H. Christenson, J. W. Cronin, V. L. Fitch, & R. Turlay, Evidence for the 2π Decay of the K_0^2 Meson, *Physical Review Letters*, 13(4), 138, 1964.
- [16] A. D. Sakharov, Violation of CP invariance, C asymmetry, and baryon asymmetry of the universe, *Journal of Experimental and Theoretical Physics*, 5: 24-27, 1967.
- [17] C. S. Wu, E. Ambler, R. W. Hayward, D. D. Hoppes, & R. P. Hudson, Experimental test of parity conservation in beta decay, *Physical review*, 105(4), 1413, 1957.
- [18] A. Schuster, Potential matter. A holiday dream. *Nature*, 58(1503), 367, 1898.
- [19] A. Benoit-Lévy, G. Chardin, Do we live in a "Dirac-Milne" universe?, *Astro-ph*, 2009.
- [20] M. M. Nieto & T. Goldman, The arguments against antigravity and the gravitational acceleration of antimatter, *Phys. Rep.* 205-221, 1991.
- [21] G. Y. Drobychev et al., Proposal for the AEGIS experiment at the CERN antiproton decelerator (Antimatter Experiment: Gravity, Interferometry, Spectroscopy), 2007.
- [22] M. Bregman et al., Measurement of antiproton lifetime using the ICE storage ring, *Physics Letters B*, 78(1), 174-175, 1978.
- [23] A. M. Green & J. A. Niskanen, Low energy antiproton physics in the early LEAR era, *Progress in Particle and Nuclear Physics*, 18, 93-182, 1987.
- [24] S. Maury, The antiproton decelerator: AD. *Hyperfine Interactions*, 109(1), 43-52, 1997.
- [25] D. Möhl, Production of low-energy antiprotons, *Hyperfine Interactions*, 109(1), 33-41, 1997.
- [26] J. Y. Hémerly & S. Maury, The antiproton decelerator: overview, *Nuclear Physics A*, 655(1-2), c345-c352, 1999.
- [27] D. Möhl, G. Petrucci, L. Thorndahl, & S. Van Der Meer, Physics and technique of stochastic cooling, *Physics Reports*, 58(2), 73-102, 1980.
- [28] S. Van Der Meer, Stochastic cooling and the accumulation of antiprotons, *Reviews of Modern Physics*, 57(3), 689, 1985.
- [29] H. Poth, Electron cooling: theory, experiment, application, *Physics reports*, 196(3-4), 135-297, 1990.
- [30] S. Maury et al., ELENA: the extra low energy anti-proton facility at CERN, *Hyperfine Interactions*, 229(1-3), 105-115, 2014.
- [31] A. Hydromako, Detection of Trapped Antihydrogen, University of Calgary PhD thesis, 2011.
- [32] Ch. Hirt, S. Claessens, T. Fecher, M. Kuhn, R. Pail & M. Rexer, New ultrahigh-resolution picture of Earth's gravity field, *Geophysical Research Letters*, 2013.
- [33] <http://www.wolframalpha.com/widgets/view.jsp?id=d34e8683df527e3555153d979bcda9cf> (accessed on September 1st, 2017)

-
- [34] S. Baessler et al., Improved test of the equivalence principle for gravitational self-energy, *Physical Review Letters*, 83(18), 3585, 1999.
- [35] P. Touboul & M. Rodrigues, The MICROSCOPE space mission, *Classical and Quantum Gravity*, 18(13), 2487, 2001.
- [36] J. Overduin, F. Everitt, P. Worden & J. Mester, STEP and fundamental physics, *Classical and Quantum Gravity*, 29(18), 184012, 2012.
- [37] CP LEAR collaboration, Tests of the equivalence principle with neutral kaons, *Phys. Lett. B* 452,425-433, 1999.
- [38] R. J. Hughes & M. H. Holzscheiter, Constraints on the gravitational properties of antiprotons and positrons from cyclotron-frequency measurements, *Physical review letters*, 66(7), 854, 1991.
- [39] G. Gabrielse et al., Precision mass spectroscopy of the antiproton and proton using simultaneously trapped particles, *Phys. Rev. Lett.* 82, 3198-3201, 1999.
- [40] S. Pakvasa, W. Simmons & T. Weiler, Test of equivalence principle for neutrinos and antineutrinos, *Phys. Rev. D* 39, 1761-1763, 1989.
- [41] F. Witteborn and W. Fairbank, *Phys Rev Lett* 19, 1049, 1967.
- [42] N. Beverini et al., PS200 proposal Preprint, Los Alamos National Laboratory report LAUR-86-260, 1986.
- [43] P. Scampoli & J. Storey, The AEGIS experiment at CERN for the measurement of antihydrogen gravity acceleration, *Modern Physics Letters A*, 29(17), 1430017, 2014.
- [44] T. Brando, Observations of low-energy antineutrons in a time-separated neutral beam, *Nucl. Instrum. Methods* 180, 461-467, 1981.
- [45] H. Abele, T. Jenke, D. Stadler & P. Geltenbort, Qubounce: The dynamics of ultra-cold neutrons falling in the gravity potential of the Earth, *Nuclear Physics A*, 827(1-4), 593-595, 2009.
- [46] S. D. Hogan, Rydberg positronium for tests of antimatter gravity, 3rd International Workshop on Antimatter and Gravity, London, U.K., Aug. 2015.
- [47] M. Giammarchi, Quantum Interferometry and Gravity with Positronium, Lorentz- and CPT-violating Standard-Model Extension, Indiana University, Bloomington, 2015.
- [48] G. A. Baur et al., Production of antihydrogen, *Physics Letters B*, 368(3), 251-258, 1996.
- [49] M. E. A. Amoretti et al., Production and detection of cold antihydrogen atoms, *Nature*, 419(6906), 456-459, 2002.
- [50] G. Gabrielse et al., Background-free observation of cold antihydrogen with field-ionization analysis of its states, *Physical Review Letters*, 89(21), 213401, 2002.
- [51] G. B. Andresen et al., Confinement of antihydrogen for 1000 seconds, *Nature Physics* 7: 558. arXiv:1104.4982, 2011.
- [52] M. Ahmadi et al., Observation of the 1S - 2S transition in trapped antihydrogen, *Nature*, 541(7638), 506-510, 2017.

- [53] A. E. Charman & the ALPHA collaboration, Description and first application of a new technique to measure the gravitational mass of antihydrogen, *Nature communications*, 4 1785, 2013
- [54] P. Perez, Y. Sacquin, The GBAR experiment: gravitational behaviour of antihydrogen at rest, *Classical and Quantum Gravity*, Volume 29, Number 18, pp. 184008-184019(12), 2012.
- [55] S. Aghion et al., Laser excitation of the $n = 3$ level of positronium for Antihydrogen production, *Physical Review A* 94, 2016.
- [56] G. Testera et al., The aegis experiment. *Hyperfine Interactions*, 233(1-3), 13-20, 2015.
- [57] D. Krasnicky et al., AEGIS experiment commissioning at CERN. In *AIP Conference Proceedings* (Vol. 1521, No. 1, pp. 144-153, 2013).
- [58] A. Kellerbauer & S. Fritzsche, High-resolution optical spectroscopy of Os^- with a view to laser cooling of atomic anions, *Journal of Physics: Conference Series*, 388(1):012023, 2012.
- [59] E. Jordan, G. Cerchiari, S. Fritzsche, & A. Kellerbauer, High-resolution spectroscopy on the laser-cooling candidate La^- , *Phys. Rev. Lett.*, 115:113001, Sep 2015.
- [60] D. Comparat, Molecular cooling via Sisyphus processes, *Phys. Rev. A*, 89(4):43410, 2014.
- [61] B. I. Deutch, A. S. Jensen, A. Miranda & G. C. Oades, *Proc. 1st Workshop on Antimatter Physics at Low Energies (Fermilab, Batavia II, FNAL)* p 371, 1986.
- [62] G. Gabrielse et al., ATRAP Collaboration, *Phys. Lett. B* 548 140, 2002.
- [63] M. Charlton, Antihydrogen production in collisions of antiprotons with excited-states of positronium, *Phys. Lett. A* 143 143, 1990.
- [64] J. P. Merrison et al., Hydrogen formation by proton impact on positronium, *Physical review letters*, 78(14), 2728, 1997.
- [65] M. K. Oberthaler, Anti-matter wave interferometry with positronium, *Nuclear Instruments and Methods in Physics Research B*, 192:129-134, 2002.
- [66] E. Klempt, C. Batty & J-M. Richard, *Phys. Rep.* 413, 197, 2005.
- [67] G. Bendiscioli and D. Kharzeev, *La Rivista del Nuovo Cimento* 17, 1, 1994.
- [68] C. Ghesquière, An inclusive view on $p\bar{p} \rightarrow n\pi$ at rest, in *Symposium on Antinucleon-Nucleon Interactions*, CERN-1974-018 pp.436-446, 1974.
- [69] S. J. Orfanidis and V. Rittenberg, *Nucl. Phys. B* 59, 570, 1973.
- [70] L. Landau & E. Lifshitz, *Quantum Mechanics (Non-relativistic Theory)*, vol. 3. Pergamon Press, 1977.
- [71] O. Ahlen, Rydberg Hydrogen Detector with n-state dependent Field Ionization, *Chalmers University Master thesis*, pp. 24-34, 2013.
- [72] Hamamatsu MCP assembly technical information , pp. 10, 2006.
- [73] K. Berggren, A high sensitivity imaging detector for the study of the formation of (anti)hydrogen, *Linköping University Master thesis*, 2013.
- [74] www.thorlabs.com (accessed on September 1st, 2017)

- [75] www.sony.co.jp (accessed on September 1st, 2017)
- [76] www.finesensing.com/iiimaging/doc/PhosphorScreen.pdf (accessed on September 1st, 2017)
- [77] M. H. Holzscheiter, N. Bassler, N. Agazaryan, G. Beyer, E. Blackmore, J. J. De Marco & H. V. Knudsen, The biological effectiveness of antiproton irradiation, *Radiotherapy and Oncology*, 81(3), 233-242, 2006.
- [78] S. Aghion et al., A moiré deflectometer for antimatter, *Nature communications*, 5 1-6, 2014.
- [79] A. Peters, K. Y. Chung & S. Chu, High-precision gravity measurements using atom interferometry, *Metrologia*, 38(1), 25, 2001.
- [80] M. K. Oberthaler, S. Bernet, E. M. Rasel, J. Schmiedmayer, & A. Zeilinger, Inertial sensing with classical atomic beams, *Physical Review A*, vol. 54, num 4, 1996.
- [81] P. Bräunig, Atom Optical Tools for Antimatter Experiments, Heidelberg University PhD thesis, 2015.
- [82] P. Bräunig, A. Demetrio, S. Müller and M. K. Oberthaler, Limits on a gravity measurement with a non-collimated antihydrogen source, internal AEGIS note, Jul. 2015.
- [83] F. Bergermann, Characterization of the Moiré Deflectometer for the AEgIS-Experiment, Heidelberg University Diploma thesis, 2012.
- [84] F. C. Hauptert, A Moiré-Deflectometer as Gravimeter for Antihydrogen, Heidelberg University PhD thesis, 2012.
- [85] C. Patrignani & Particle Data Group, Review of particle physics, *Chinese physics C*, 40(10), 100001, 2016.
- [86] P. Lansonneur, P. Bräunig, A. Demetrio, S. R. Müller, P. Nedelec, & M. K. Oberthaler, Probing Electric and Magnetic Fields with a Moiré Deflectometer, *Nuclear Instruments and Methods in Physics Research Section A: Accelerators, Spectrometers, Detectors and Associated Equipment*, 862, 49-53, 2017.
- [87] S. R. Müller, Moiré Deflectometer for Charged Particles, Heidelberg University Master thesis, 2015.
- [88] R. E. Grisenti, W. Schöllkopf, J.P. Toennies, J. R. Manson, T. A. Savas, & H. I. Smith, He-atom diffraction from nanostructure transmission gratings: The role of imperfections, *Physical Review A*, 61(3) (2000) 033608.
- [89] www.simion.com (accessed on September 1st, 2017)
- [90] W. F. Brown, Magnetic Materials, Ch 8, in the *Handbook of Chemistry and Physics*, Condon and Odishaw, eds. McGraw-Hill, 1958.
- [91] L. De Broglie, Recherches sur la théorie des quanta, Doctoral dissertation Thesis, 1924.
- [92] I. Estermann & O. Stern, Beugung von Molekularstrahlen, *Z. Phys.* 61, 95-125, 1930.
- [93] H. Halban & P. Preiswerk, Preuve expérimentale de la diffraction des neutrons, *C.R. Acad. Sci.* 203, 73-75, 1936.

- [94] M. Arndt, O. Nairz, J. Vos-Andreae, C. Keller, G. Van der Zouw & A. Zeilinger, Wave-particle duality of C₆₀ molecules, *Nature*, 401(6754), 680-682, 1999.
- [95] S. Eibenberger, S. Gerlich, M. Arndt, M. Mayor, & J. Tüxen, Matter-wave interference of particles selected from a molecular library with masses exceeding 10000 amu, *Physical Chemistry Chemical Physics*, 15(35), 14696-14700, 2013.
- [96] G. P. Thomson & A. Reid, Diffraction of cathode rays by a thin film, *Nature*, 119(3007), 890, 1927.
- [97] C. J. Davisson & L. H. Germer, Reflection of Electrons by a Crystal of Nickel, *Proceedings of the National Academy of Sciences*, 14(4), 317-322, 1928.
- [98] F. Hasselbach, Progress in electron-and ion-interferometry, *Reports on Progress in Physics*, 73(1), 016101, 2009.
- [99] G. Schütz et al., Biprism electron interferometry with a single atom tip source, *Ultramicroscopy*, 141, 9-15, 2014.
- [100] B. Neyenhuis, D. Christensen & D. S. Durfee, Testing nonclassical theories of electromagnetism with ion interferometry, *Physical review letters*, 99(20), 200401, 2007.
- [101] H.F. Talbot, Facts relating to optical science, *Philosophical Magazine Series 3*, 9(56):401-407, 1836.
- [102] E. Lau, Beugungserscheinungen an Doppelrastern, *Ann. Phys.* 437, 417-423, 1948.
- [103] E. Wigner, On the Quantum Correction For Thermodynamic Equilibrium, *Physical Review*, 40(5):749-759, 1932.
- [104] L. Zehnder, *Z. Instrumentenkunde* 11, 275, 1891.
- [105] L. Mach, *Z. Instrumentenkunde* 12, 89, 1892.
- [106] www.ipnl.in2p3.fr (accessed on September 1st, 2017)
- [107] www.lpsc.in2p3.fr (accessed on September 1st, 2017)
- [108] www.ni.com/labview (accessed on September 1st, 2017)
- [109] T. Thuillier, CERN Accelerator School 2012, Senec, 2012.
- [110] A. Coly, Etudes expérimentales de sources d'ions RCE à 2.45 GHz pour la production de courants intenses, Grenoble University PhD thesis, 2010.
- [111] R. Geller, *Electron Cyclotron Resonance Ion Sources and ECR Plasmas*, IOP Publishing, 1996.
- [112] P. Sortais, T. Lamy, J. Médard, J. Angot, L. Latrasse & T. Thuillier, Ultracompact/ultralow power electron cyclotron resonance ion source for multipurpose applications, *Review of Scientific Instruments*, 81(2), 02B314, 2010.
- [113] F. Paschen, Sur la différence de potentiel nécessaire à la formation d'arc électrique dans l'air, l'hydrogène et le gaz carbonique sous différentes pressions, *Wied. Annales de physique*, Vol.37, 69-96, 1889.
- [114] E. Badarau & I. Popescu, *Gaz ionisés, décharges électriques dans les gaz*, Paris, Dunod, 334 p, 1968.

- [115] C. C. Finlay et al., International geomagnetic reference field: the eleventh generation, *Geophysical Journal International*, 183(3), 1216-1230, 2010.
- [116] A. Müller, Scaling of cross sections for multiple electron transfer to highly charged ions colliding with atoms and molecules, *Physics Letters A*, Vol. 62, Issue 6, p. 391-394, 1977.
- [117] J. A. Ray & C. F. Barnett, Secondary Electron Emission of Metals Bombarded with 120 eV to 5 keV Protons, *Journal of Applied Physics* 42, 3260, 1971.
- [118] T. Taylor & J.F. Mouris, An advanced high-current low-emittance dc microwave proton source, *Nucl. Instr. And Meth. A*, 336(1-2), 1-5, 1993.
- [119] D. Shiner et al., H₂, D₂, and HD ionization potentials by accurate calibration of several iodine lines, *Physical Review A*, 47(5), 4042, 1993.
- [120] E. Herbst, The Astrochemistry of H₃⁺, *Phil. Trans. R. Soc. Lond. A.*, vol. 358, 1774, p.2523-2534, 2000.
- [121] D. Spence & K. R. Lykke, Generation of High purity cw proton beams from microwave driven source, in *Particle Accelerator Conference, Proceedings of the 1995 IEEE*, Vol. 2, pp. 1019-1021, 1995.
- [122] A. D. Gaus, W. T. Htwe, J. A. Brand, T. J. Gay, & M. Schulz, Energy spread and ion current measurements of several ion sources, *Review of scientific instruments*, 65(12), 3739-3745, 1994.
- [123] M. E. Rudd, R. D. DuBois, L. H. Toburen, C. A. Ratcliffe, & T. V. Goffe, Cross sections for ionization of gases by 5-4000-keV protons and for electron capture by 5-150-keV protons, *Physical Review A*, 28(6), 3244, 1983.
- [124] www.attocube.com (accessed on September 1st, 2017)
- [125] W. F. Brown, Magnetic Materials, Ch 8, in the *Handbook of Chemistry and Physics*, Condon and Odishaw, eds. McGraw-Hill, 1958.
- [126] www.magneticshields.co.uk (accessed on September 1st, 2017)
- [127] www.quantumnano.at (accessed on September 1st, 2017)
- [128] www.tibtech.com/conductivity.php (accessed on September 1st, 2017)
- [129] J. F. Ziegler, M. D. Ziegler & J. P. Biersack, SRIM - The stopping and range of ions in matter (2010), *Nuclear Instruments and Methods in Physics Research Section B: Beam Interactions with Materials and Atoms*, 268(11), 1818-1823, 2010.
- [130] www.alliedvision.com (accessed on September 1st, 2017)
- [131] P. Friebel, Grating Alignment using Mach-Zehnder Interferometers, Heidelberg University Bachelor thesis, 2017.
- [132] B. L. Peko & T. M. Stephen, Absolute detection efficiencies of low energy H, H⁻, H⁺, H₂⁺ and H₃⁺ incident on a multichannel plate detector, *Nuclear Instruments and Methods in Physics Research Section B: Beam Interactions with Materials and Atoms*, 171(4), 597-604, 2000.
- [133] www.gids-gmbh.com/en/10.html (accessed on September 1st, 2017)

- [134] www.quantar.com/pages/QTI/ofs.htm (accessed on September 1st, 2017)
- [135] www.finesensing.com/iiimaging/doc/PhosphorScreen.pdf (accessed on September 1st, 2017)
- [136] M. Saito, Y. Saito, K. Asamura & T. Mukai, Spatial charge cloud size of microchannel plates, *Review of scientific instruments*, 78(2), 023302, 2007.
- [137] P. Braunig, J. Storey, and M. K. Oberthaler, AtliX: Antimatter Talbot-Lau Interferometry Experiment, Internal Proposal of the AEgIS collaboration, 2014.
- [138] T. J. Phillips, Antimatter gravity studies with interferometry, *Hyperfine Interactions*, 109(1-4):357-365, 1997.
- [139] P. Hamilton et al., Antimatter interferometry for gravity measurements, *Physical Review Letters*, 112(12), 2014.
- [140] M. K. Oberthaler, Anti-matter wave interferometry with positronium, *Nuclear Instruments and Methods in Physics Research B*, 192:129-134, 2002.
- [141] D. M. Kaplan et al., Measuring antimatter gravity with muonium, arXiv preprint, arXiv:1308.0878, 2013.
- [142] E. Klempt, C. Batty, and J.-M. Richard, *Phys. Rep.* 413, 197, 2005.
- [143] G. Bendiscioli and D. Kharzeev, *La Rivista del Nuovo Cimento* 17, 1, 1994.
- [144] C. Ghesquière, An inclusive view on $p\bar{p} \rightarrow n\pi$ at rest, in *Symposium on Antinucleon-Nucleon Interactions*, CERN-1974-018 pp.436-446, 1974.
- [145] S. J. Orfanidis and V. Rittenberg, *Nucl. Phys. B* 59, 570, 1973.
- [146] A. Hydromako, Detection of Trapped Antihydrogen, University of Calgary PhD thesis, 2011.
- [147] R. Acquafredda et al., *JINST* 4, P04018, 2009.
- [148] G. B. Andresen et al., Antiproton, positron, and electron imaging with a microchannel plate/phosphor detector, *Review of Scientific Instruments*, 80(12), 123701, 2009.
- [149] T. Poikela, J. Plosila, T. Westerlund, M. Campbell, M. De Gaspari,... & V. Zivkovic, Timepix3: a 65K channel hybrid pixel readout chip with simultaneous ToA/ToT and sparse readout, *Journal of instrumentation*, 9(05), C05013, 2014.
- [150] www.cern.ch/medipix (accessed on September 1st, 2017)
- [151] N. Pacifico et al., Direct detection of antiprotons with the Timepix3 in a new electrostatic selection beamline, *Nuclear Instruments and Methods in Physics Research Section A: Accelerators, Spectrometers, Detectors and Associated Equipment*, 2016.
- [152] N. Asbah et al., Measurement of the efficiency of the pattern recognition of tracks generated by ionizing radiation in a TIMEPIX detector, *Journal of Instrumentation*, 9(05), C05021 pp. 4, 2014.
- [153] A. Lesauvage, Simulations avec Geant4 pour l'expérience AEgIS, Lyon University Bachelor thesis, 2016.

-
- [154] P. V. Hough, Method and means for recognizing complex patterns, 1962 (No. US 3069654).
- [155] H. Holmestadt. Analysis of the 2015 data. GRACE/ATLIX internal note, Oct. 2016.
- [156] R. O. Duda & P. E. Hart, Use of the Hough transformation to detect lines and curves in pictures, *Communications of the ACM*, 15(1), 11-15, 1972.
- [157] S. D. Pinto, R. Jones, L. Ropelewski, J. Spanggaard & G. Tranquille, GEM-based beam profile monitors for the antiproton decelerator, *Journal of Instrumentation*, 7(03), C03001, 2012.
- [158] M. H. Holzscheiter, N. Bassler, N. Agazaryan, G. Beyer, E. Blackmore, J. J. De Marco & H. V. Knudsen, The biological effectiveness of antiproton irradiation, *Radiotherapy and Oncology*, 81(3), 233-242, 2006.
- [159] www.eljentechnology.com (accessed on September 1st, 2017)
- [160] W. H. Barkas, J. N. Dyer & H. H. Heckman, Resolution of the Σ^- mass anomaly, *Physical Review Letters*, 11(1), 26, 1963.
- [161] L. H. Andersen et al., Measurement of the Z_1^3 contribution to the stopping power using MeV protons and antiprotons: The Barkas effect, *Physical review letters* 62.15:1731, 1989.
- [162] S. Agostinelli et al., GEANT4 - a simulation toolkit, *Nuclear instruments and methods in physics research section A: Accelerators, Spectrometers, Detectors and Associated Equipment*, 506(3), 250-303, 2003.
- [163] www.root.cern.ch (accessed on September 1st, 2017)
- [164] 3rd General Conference on Weights and Measures, Paris, CR 70, 1901.

Appendices

A | Hough Transform

The Hough transform [154] is a pattern recognition technique, commonly used to detect straight lines on an image. This tool, initially developed to retrieve the tracks of particles in bubble chambers, is also particularly convenient to identify arbitrary shapes such as circle or ellipse in an image (generalized Hough transform [156]).

Let us consider an image where the shape of a line is expected. For each pixel of the image, the underlying idea is to associate the coordinates (r, θ) defined by:

$$r = x \cos \theta + y \sin \theta, \tag{A.1}$$

where x and y are the coordinates of the pixel. With this change of coordinates, a point with coordinates (x, y) in the image becomes a sinusoidal curve in the (r, θ) space (or Hough space). Equation A.1 can be reversed in order to express x and y as a function of r and θ :

$$y = -\frac{\cos \theta}{\sin \theta} x + \frac{r}{\sin \theta}. \tag{A.2}$$

Such that each point with coordinates (r, θ) in the Hough space corresponds to a line in the image space. The Hough transform of a simple image representing a line and a point is shown on figure A.1.

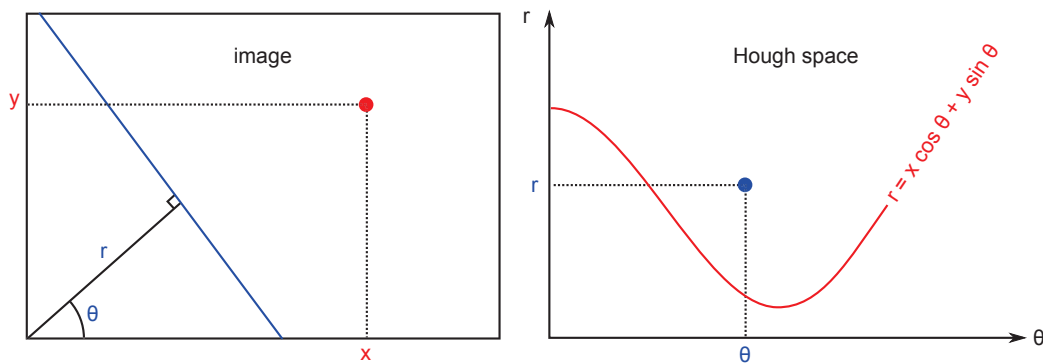


Figure A.1: A straight line in the image space is represented as a point in the (r, θ) space (or Hough space). Inversely, a point in the image space becomes a sinusoidal curve in the Hough space.

For more complex images, one can equivalently transform each pixel into a sinus curve in the Hough space (after having applied a edge detection algorithm for example). The intersection point of the sinus curve represents then the line that pass through the most pixels. The Hough transform is illustrated on figure A.2 to find a straight line (marked by a black arrow) on a complex image.

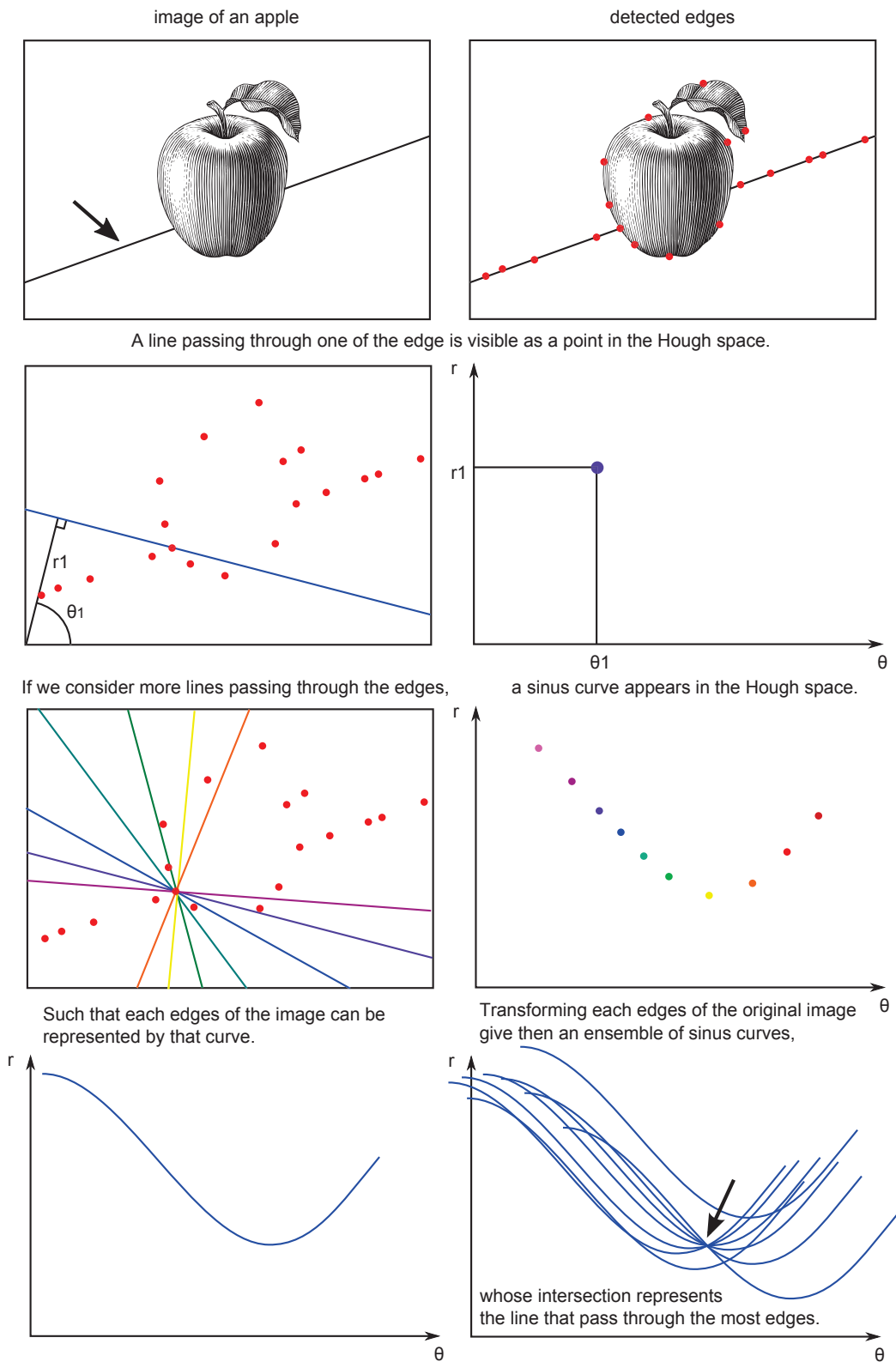


Figure A.2: How the Hough transform enables one to find a straight line (black arrow) on an image.

B | Software

ROOT

ROOT is an object-oriented program developed by CERN. It was originally designed for particle physics data analysis but it provides all the functionalities needed to deal with big data processing, statistical analysis, visualisation and storage. It is mainly written in C++ but integrated with other languages such as Python [163]. The version used in this thesis is ROOT 5.34.

Geant4

Geant4 (for GEometry ANd Tracking) is a program used to simulate the passage of particles through matter, using Monte Carlo methods. It is the successor of the GEANT series of software toolkits developed by CERN, and the first to use object oriented programming (in C++). Its development, maintenance and user support are ensured by the international Geant4 Collaboration. Application areas include high energy physics and nuclear experiments, medical, accelerator and space physics studies. Geant4 software and source code is freely available from the project web site [162].

SRIM

Besides Geant4, the transport of ions in matter can be calculated in simple configurations with the program SRIM (for Stopping and Range of Ions in Matter). Typical applications include the simulation of the stopping power and range in several material, ion implantation, sputtering (when an ion beam extract the atoms of a target) and ion beam therapy. Most aspects of the energy loss of ions in matter are calculated in SRIM (stopping powers, range and straggling distributions). The program offers moreover the possibility to simulate multi-layer targets [129].

SIMION

SIMION is an ion optics simulation program used to calculate electric fields nearby a set of electrodes and the ion trajectories in those fields. The version used in this thesis is SIMION 8.0 [89]. The three dimensional electrostatic fields are first retrieved by solving the Laplace equation (from the electric potential) by a finite elements method. Once the electric fields obtained, the trajectories of charged particles are computed. For this purpose, electrostatic forces are calculated at the position of the ion (at time t). Finally, the acceleration of the ion is deduced from the force and the position of the ion at time $t + \Delta t$ is integrated numerically.

C | Constants

Quantity	Symbol	Value
Planck constant	h	$6.626070040(81) \times 10^{-34} \text{ m}^2 \cdot \text{kg}^{-1} \cdot \text{s}$
speed of light	c	$299792458 \text{ m} \cdot \text{s}^{-1}$
Boltzmann constant	k_B	$1.38064852 \times 10^{-23} \text{ m}^2 \cdot \text{kg} \cdot \text{s}^{-2} \cdot \text{K}^{-1}$
Earth gravitational acceleration	g	$9.80665 \text{ m} \cdot \text{s}^{-2}$
electron mass	m_e	$9.10938356(11) \times 10^{-31} \text{ kg}$
proton mass	m_p	$1.672621898(21) \times 10^{-27} \text{ kg}$
elementary charge	e	$1.60217662 \times 10^{-19} \text{ C}$

Table C.1: List of constants used in this thesis (from [85]). The $1-\sigma$ uncertainties on the last digits are given in parentheses. The value of the Earth gravitational acceleration given here is the normalized one, adopted by the 3rd General Conference on Weights and Measures [164].